

REVIEW ARTICLE | JUNE 24 2025

A review on temperature coefficient of frequency (TCf) in resonant microelectromechanical systems (MEMS)

Wen Sui  ; Stephen J. Pearton  ; Philip X.-L. Feng  



Appl. Phys. Rev. 12, 021330 (2025)
<https://doi.org/10.1063/5.0201566>



Articles You May Be Interested In

Piezoelectric thin films and their applications in MEMS: A review

J. Appl. Phys. (January 2025)

Opportunities and challenges involving repulsive Casimir forces in nanotechnology

Appl. Phys. Rev. (December 2024)

Emerging MEMS sensors for ocean physics: Principles, materials, and applications

Appl. Phys. Rev. (May 2024)

A review on temperature coefficient of frequency (TCf) in resonant microelectromechanical systems (MEMS)

F

Cite as: Appl. Phys. Rev. **12**, 021330 (2025); doi: [10.1063/5.0201566](https://doi.org/10.1063/5.0201566)

Submitted: 31 January 2024 · Accepted: 16 January 2025 ·

Published Online: 24 June 2025



View Online



Export Citation



CrossMark

Wen Sui,¹ Stephen J. Pearton,² and Philip X.-L. Feng^{1,3,a}

AFFILIATIONS

¹Department of Electrical & Computer Engineering, Herbert Wertheim College of Engineering, University of Florida, Gainesville, Florida 32611, USA

²Department of Materials Science & Engineering, Herbert Wertheim College of Engineering, University of Florida, Gainesville, Florida 32611, USA

³Department of Physics, College of Liberal Arts & Sciences, University of Florida, Gainesville, Florida 32611, USA

^aAuthor to whom correspondence should be addressed: philip.feng@ufl.edu

ABSTRACT

Microelectromechanical systems (MEMS) have emerged as highly attractive alternatives to conventional commercial off-the-shelf electronic sensors and systems due to their ability to offer miniature size, reduced weight, and low power consumption (i.e., SWaP advantages). These features make MEMS particularly appealing for a wide range of critical applications, including communication, biomedical, automotive, aerospace, and defense sectors. Resonant MEMS play crucial roles in these applications by providing precise timing references and channel selections for electronic devices, facilitating accurate filtering, mixing, synchronization, and tracking via their high stability and low phase noise. Additionally, they serve as key components in sensing applications, enabling detection and precise measurement of physical quantities for monitoring and control purposes across various fields. Temperature stability stands as a paramount performance specification for MEMS resonators and oscillators. It relates to the responsivity of a resonator's frequency to temperature variations and is typically quantified by the *temperature coefficient of frequency* (TCf). A constant and substantially large absolute TCf is preferred in MEMS temperature sensing applications, while a near-zero TCf is required for timing and other MEMS transducers that necessitate the decoupling of temperature effects on the resonance frequency. This comprehensive review aims to provide an in-depth overview of recent advancements in studying TCf in MEMS resonators. The review explores the compensation and engineering techniques employed across a range of resonator types, utilizing diverse materials. Various aspects are covered, including the design of MEMS resonators, theoretical analysis of TCf, temperature regulation techniques, and the metallization effect at high temperatures. The discussion encompasses TCf analysis of MEMS resonators operating in flexural, torsional, surface, and bulk modes, employing materials such as silicon (Si), lithium niobate (LiNbO_3), silicon carbide (SiC), aluminum nitride (AlN), and gallium nitride (GaN). Furthermore, the review identifies areas that require continued development to fully exploit the TCf of MEMS resonators.

Published under an exclusive license by AIP Publishing. <https://doi.org/10.1063/5.0201566>

29 June 2025 22:04:31

TABLE OF CONTENTS

I. INTRODUCTION.....	2	B. TCf of cantilever	7
II. SCIENTIFIC BACKGROUND AND MOTIVATION....	3	C. TCf of circular drumhead	7
III. MEMS STRUCTURE AND DESIGN THEORY.....	3	D. TCf of surface acoustic wave resonator.....	7
IV. THEORETICAL ANALYSIS OF TCF FOR MEMS WITH DIFFERENT STRUCTURES	6	E. TCf of Lamb wave resonator	7
A. TCf of doubly clamped structure	6	F. Temperature coefficient of Young's modulus	8
1. Flexural rigidity dominated resonance	6	V. TEMPERATURE REGULATION TECHNIQUES.....	8
2. Stress dominated resonance	6	VI. TEMPERATURE COMPENSATION TECHNIQUES ..	11
		VII. METALLIZATION EFFECTS.....	12
		VIII. TCF OF Si MEMS.....	13

A. Si MEMS for temperature sensing	14
B. Temperature compensation of Si MEMS	14
1. Passive methods	14
2. Active methods	18
IX. TCF OF LITHIUM-BASED OXIDES MEMS	19
A. Temperature compensation with SiO_2	19
B. Temperature compensation with AlN	19
X. TCF OF SiC MEMS	20
XI. TCF OF AlN MEMS	20
A. TCf of AlN SAW	21
1. SAW on AlN/sapphire	22
2. SAW on AlN/quartz	24
3. SAW on AlN/diamond	24
4. SAW on AlN/metal	25
5. SAW on AlN/ LiNbO_3	25
6. SAW on AlN/Si	25
7. SAW on AlN/SiC	25
8. Discussion on the TCf of AlN SAW resonators	26
B. TCf of AlN SMR	26
C. TCf of AlN LWR	28
D. TCf of AlN TPoS	29
E. TCf of AlN CMR	30
XII. TCF OF $\text{Al}_{1-x}\text{Sc}_x\text{N}$ MEMS	31
A. TCf of $\text{Al}_{1-x}\text{Sc}_x\text{N}$ FBAR	32
B. TCf of $\text{Al}_{1-x}\text{Sc}_x\text{N}$ SAW	32
C. TCf of $\text{Al}_{1-x}\text{Sc}_x\text{N}$ LWR	32
D. TCf of $\text{Al}_{1-x}\text{Sc}_x\text{N}$ TPoS	33
XIII. TCF OF GaN MEMS	33
A. TCf of GaN MEMS operating in flexural mode	34
B. TCf of GaN SAW	35
C. TCf of GaN BAW	35
XIV. TCF OF ONE- AND TWO-DIMENSIONAL (1D AND 2D) NEMS	35
XV. SUMMARY AND OUTLOOK	37

I. INTRODUCTION

Microelectromechanical systems (MEMS) are highly multidisciplinary and pervasive technologies that encompass design, fabrication or processing, characterization, packaging, and integration, and are used to create miniaturized, chip-scale integrated devices and systems that combine at least mechanical and electrical elements and functions.^{1–6} They are usually fabricated using integrated circuit (IC) batch processing or similar techniques and can range in size from the order of a micrometer ($\sim 1 \mu\text{m}$) to millimeters. Such devices (or systems) have the abilities to sense, actuate, control, and perform signal processing and computation on the microscale and generate impacts on the macroscale.^{7–11} Advances in mechanical structural designs, materials science, and fabrication techniques offer new opportunities for MEMS, such as gyroscopes, accelerometers, radio frequency (RF) resonators, oscillators, switches, biosensors, and micromirrors.^{12–16} The significantly reduced size, weight, and power (SWaP) of MEMS are attractive for a wide spectrum of applications ranging from consumer electronics and medical devices^{17–21} to military and space missions.^{22–28}

MEMS for harsh environment applications are becoming increasingly important because they are recognized as essential for reducing weight and volume in strategic market sectors such as automotive,

aerospace, turbomachinery, oil well logging equipment, industrial process control, nuclear power, and communications.^{29–36} Typical temperatures for automotive and aerospace systems range from 20°C to 600°C . Higher temperatures up to and above 900°C can be found in extremely harsh environments, such as gas turbine engines and nuclear power generators.^{37–39} MEMS are required to be resistant to a wide range of environmental factors, such as high levels of radiation, acceleration/deceleration, and extreme temperatures, while maintaining the performance and excellent reliability comparable to those operated in ambient environment.^{40–46}

Emerging MEMS applications in extreme high- or low-temperature terrestrial environments present many additional challenges.^{47–52} Often, one of the first challenges is to identify suitable materials and then the next challenge may be to engineer robust interfaces.^{53–58} Regarding material selection, high-temperature tolerance (e.g., high melting point) is important but usually not the only requirement. The material properties and performance also should not degrade quickly with rising temperature.^{59–63} The challenges of interfaces stem from three sources: (1) transfer of power and signal to and from the device in the high-temperature environment; (2) choice of proper materials for the interfaces, such as tubing and contacts, compatible with the material selection for the device; and (3) thermomechanical effects. Thermomechanical effects, e.g., mismatches in thermal expansions of different materials and the resulting residual stress, can influence the operation of the device. To achieve robust design and accurate simulation, it is important to understand how the key parameters that determine the performance of MEMS devices vary with temperature, including the device geometry, density, and Young's modulus of the material.⁶⁴

Conventional silicon (Si) MEMS are not suited for harsh environment applications due to failure and degradation of Si electronic properties at temperatures above 350°C .⁶⁵ Therefore, Si MEMS must reside in cooler areas or be actively cooled.^{66–68} The additional longer wires, extra packaging, and/or bulky expensive cooling systems inevitably increase the size and weight of the system; and they require a power supply, which is undesirable for high-temperature applications where suitable power sources are limited. As a result, researchers have looked into materials that are intrinsically more tolerant to these extreme cases. Wide-bandgap (WBG) materials, such as III-nitrides,^{69–75} silicon carbide (SiC),^{76–79} and diamond-like carbon (DLC),^{80–83} have emerged as promising options beyond Si for MEMS operating in harsh environments due to their superior electronic, mechanical, thermal, and chemical properties. Group III-nitrides, such as gallium nitride (GaN) and aluminum nitride (AlN), have attracted considerable attention as promising materials for high-power and ultrahigh-frequency electronics thanks to their appealing electronic properties, including intrinsic direct bandgaps, excellent breakdown field limits, high carrier mobilities, and strong piezoelectricity.^{84–87} In addition, their excellent mechanical properties and chemical inertness make them suitable for applications at high temperatures and in harsh environments.^{88,89}

In recent years, stable feedback oscillators referenced to MEMS resonators (as their frequency determining elements) have been under intensive research and have demonstrated strong potential as viable replacements for quartz crystal oscillators in frequency reference and timing applications. Although quartz crystal resonators have served the electronics industry well for almost 100 years and are still dominating the overall timing market, they are limited by several disadvantages

compared with MEMS resonators.⁹⁰ These include bulky size, manufacturing challenges when scaled down to micrometer-scale devices, reliability, sensitivity to external environmental noises, and incompatibility with semiconductor wafer-scale complementary metal-oxide-semiconductor (CMOS) processes. The application of quartz at high temperatures is limited by the phase transition from trigonal α -quartz to hexagonal β -quartz at 573 °C, which causes discontinuities in its material properties and typically restricts the use of quartz to temperatures below 350 °C. However, MEMS resonators alone (without the use of active temperature compensation) typically suffer from large frequency variations over temperature, which still hinders direct replacement of quartz crystals.

Temperature stability is one of the most important performance specifications for mechanical resonator-based oscillators in frequency reference and timing applications.^{91–93} Temperature stability depends on the responsivity of a resonator's frequency to temperature change, which can be defined by the *temperature coefficient of frequency* (TCf).^{94–101} A larger TCf is preferred in resonant MEMS temperature sensing applications, while a near-zero TCf is essential for timing and frequency reference. Various approaches have been adopted to engineer the TCf of MEMS resonators. Active compensation technologies, such as oven storage and electronic phase-locked loop (PLL), have been widely applied to compensate for the resonator's frequency variations with temperature. However, the drawbacks include inevitable circuit complexity and increased power consumption caused by additional sensors.^{102–104} In passive compensation technologies, composite structure, heavy doping, geometry engineering, and strain engineering have been adopted to engineer the temperature stability of MEMS resonators. Although the passive temperature compensation method does not complicate the circuit or increase power consumption, the drawback is that it increases fabrication complexity.^{105–107}

In this review, we offer a comprehensive and detailed survey of the thermal response of resonant MEMS. We start by introducing the scientific background and motivation (Sec. II), followed by MEMS structure and design theory (Sec. III). We then summarize and discuss the theoretical analysis of TCf for MEMS with different structures (Sec. IV). Temperature regulation techniques (Sec. V), temperature compensation techniques (Sec. VI), and metallization effects (Sec. VII) are also presented. We then survey the TCf of Si MEMS (Sec. VIII), lithium niobate (LiNbO_3) MEMS (Sec. IX), SiC MEMS (Sec. X), aluminum nitride (AlN) MEMS (Sec. XI), aluminum scandium nitride (AlScN) MEMS (Sec. XII), gallium nitride (GaN) MEMS (Sec. XIII), and emerging one- (1D) and two-dimensional (2D) NEMS (Sec. XIV). We conclude by discussing the challenges and opportunities in this highly promising field (Sec. XV).

II. SCIENTIFIC BACKGROUND AND MOTIVATION

Temperature stability is based upon the responsivity of a resonator's frequency to temperature change, which can be defined by the *temperature coefficient of frequency* (TCf). TCf can be evaluated by using

$$\text{TCf} = \frac{1}{f_0} \frac{df}{dT}, \quad (2.1)$$

where T is the temperature and f_0 is the initial or reference frequency, which often refers to the resonance frequency measured at room temperature. The resonance frequency of a resonator is primarily determined by its structure, dimensions, and material properties.^{108–113}

However, external perturbations, such as temperature fluctuations, can alter the frequency of a resonator by modifying its dimensions and material properties.^{114–116} Temperature variations lead to changes in material properties, including stress (σ) and Young's modulus (E_Y), causing a shift in resonance frequency.^{117–119} Furthermore, several temperature-related factors can affect the resonant performance of MEMS resonators, including phase changes of materials,^{120–123} electrode degradation, interface damage and failure,^{124,125} surface oxidation,^{126–129} adsorption, and desorption.^{130–134} Understanding how key parameters, such as device geometry, material density, and Young's modulus, vary with temperature is crucial for achieving the robust design and accurate simulation of MEMS devices.^{135–140} By doing so, it is possible to develop more reliable and effective MEMS devices that perform optimally across a broad range of temperatures. While WBG materials, such as AlN, GaN, and SiC, have the advantage of being more stable than Si at extreme temperatures, changes in dimensional, mechanical, and electronic properties can be significant when devices made with these materials are required to operate over a broad temperature range.^{141–145} As a result, it is essential to assess the material's characteristics not only at a single temperature but also across a wide temperature range.¹⁴⁶ MEMS resonators with linear frequency response to temperature and large absolute TCf have great potential for temperature sensing applications. Resonant MEMS temperature sensors operate by detecting frequency shifts caused by temperature changes.^{147–151} This shift exhibits a direct proportionality to fluctuations in the environmental temperature, delineated by the TCf. Employing oscillator circuits that encompass the MEMS sensor, zero-crossing detectors, and requisite circuits, these sensors effectively capture and convert the detected frequency changes into a precise temperature signal. Nevertheless, in frequency and timing applications, a zero TCf is preferred, indicating that MEMS resonators can maintain frequency stability despite temperature fluctuations. This characteristic makes them suitable for various applications, including wireless communication systems, frequency standards, and timekeeping devices.^{152–156} Therefore, researchers are continually exploring ways to engineer MEMS resonators to exhibit the desired properties and optimize their performance for specific applications. All of these considerations are summarized in Fig. 1.

III. MEMS STRUCTURE AND DESIGN THEORY

Mainstream MEMS resonators can be broadly categorized into two major types based on their transduction mechanisms: capacitive resonators, which utilize the electrostatic method,^{161–165} and piezoelectric resonators, which rely on the piezoelectric effect.^{166–169} Electrostatic resonators usually employ single crystal silicon (SCS) or polycrystalline silicon (poly-Si) as the structural material and can achieve high quality factors (Q_s), up to a few million.^{170,171} However, they suffer from a high motional impedance and relatively low electromechanical transduction efficiency. To reduce the motional impedance, a large DC polarization voltage and narrow capacitive transducer gaps as small as a few hundred nanometers are required. High DC voltage can introduce nonlinearity, while the narrow gaps demand precise process control, adding complexity to the fabrication process.^{172,173} In contrast, modern piezoelectric resonators can have higher electromechanical coupling coefficients (k_t^2), leading to a lower motional impedance.^{174–178} Although they can exhibit lower Q_s than capacitive resonators, the absence of narrow gaps makes batch manufacturing of these devices simple with good process uniformity.¹⁷⁹

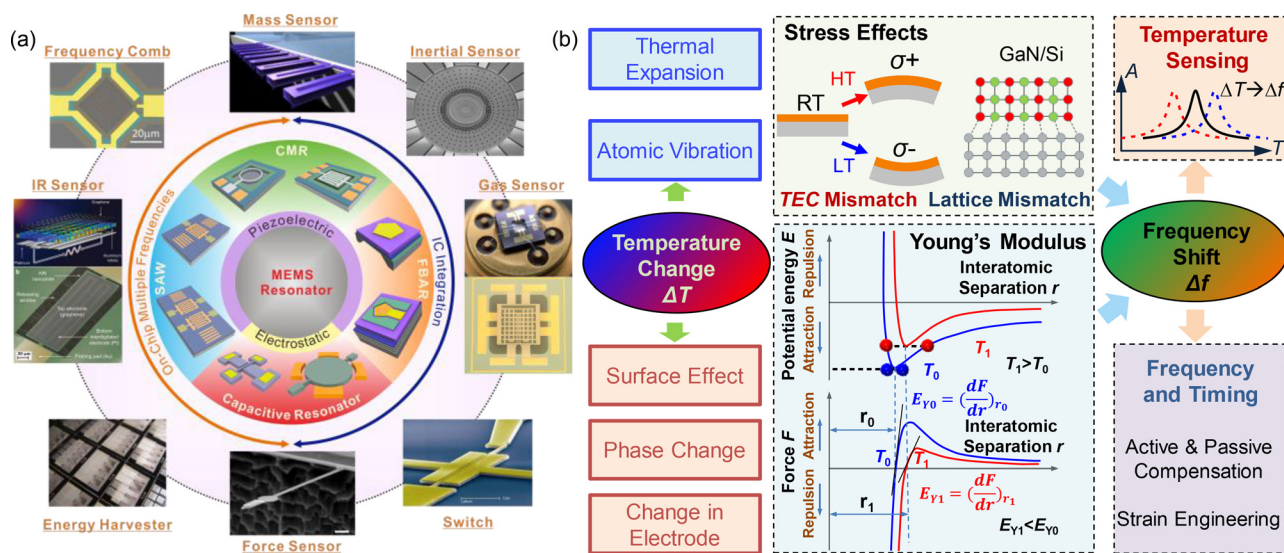


FIG. 1. Scientific background and motivation. (a) Categorization of MEMS transducers and sensors in diverse applications, including mass sensor, inertial sensor (Serrano *et al.*, *Microsyst. Nanoeng.* **2**, 16015 (2016), Open Access),¹⁵⁷ gas sensor (Open Access), switch, force sensor (Chui *et al.*, *Transducers* (2003), Copyright 2003 IEEE, Creative Commons),¹⁵⁸ energy harvester (Lin *et al.*, *IEEE International Ultrasonics Symposium* (2009), Copyright 2009 IEEE, Creative Commons),¹⁵⁹ IR sensor (Qian *et al.*, *Microsyst. Nanoeng.* **2**, 16026 (2016), Open Access),¹⁶⁰ and frequency comb.¹⁵ (b) Impact of temperature on the resonance frequency of MEMS resonators.

In terms of the mode of operation, MEMS resonators can be classified into several categories, including flexural, torsional, surface, and bulk modes, as summarized in Table I. Flexure mode vibration is generated by transverse standing waves, which are typically observed in long or thin geometries, such as cantilevers, beams, or membranes that bend under stress.^{180–184} The resonant mode shapes of flexural vibrations are determined by both the structures and boundary conditions. For flexural mode, the principal stress is almost aligned with the normal stress and is orthogonal to the linear displacement of the flexure. Common beam structures that operate in flexural modes include doubly clamped beams,^{185–188} cantilevers,^{189–193} and double-ended tuning forks (DETF).^{194–199} Microdisks and drumheads are two types of membrane structures with distinct boundary conditions.^{200–203} The maximum deflection of a microdisk (supported by a central pedestal underneath) occurs at the rim of the plate, while for a drumhead, it occurs at the center of the diaphragm or membrane. Flexural mode MEMS resonators typically have lower frequencies in kilohertz (kHz) or megahertz (MHz) range and higher Qs than bulk mode resonators. They are commonly used in applications that require high precision and stability, such as frequency references, oscillators, and filters.^{204–207} It is important to carefully control the stress and temperature conditions during the design, fabrication, and operation of flexural mode resonators to minimize the effects on their resonant frequency.^{208–211} Techniques such as thermal compensation, stress isolation, and strain engineering can be used to reduce the impact of stress and temperature changes on the resonator's performance. On the other hand, due to its pronounced sensitivity of resonance frequency to temperature variations, it is well-suited for temperature sensing.

A torsional mode resonator typically comprises a suspended paddle supported by a pair of tethers, with both the tethers and torsional paddles rotating around the axis defined by the tethers. This unique

structure of the torsional mode resonator effectively lowers anchor loss and thermal elastic damping, making it an attractive option for various sensing applications such as infrared thermal sensing,²¹² angular rate sensing,²¹³ and biosensing.²¹⁴ In addition, torsional mode resonators are less sensitive to stress and temperature changes compared to flexural mode resonators, making them suitable for use in harsh environments and temperature-compensated oscillator circuits.

The principles of surface acoustic wave (SAW) devices were first predicted by Lord Rayleigh in 1895. In 1965, the electronics industry discovered that SAW transducers could be valuable in the design of analog filters with specific frequencies, thus marking their first use in this field.²¹⁵ Since then, SAW devices have become increasingly popular due to their unique ability to manipulate and filter RF signals with high precision, making them an essential component in a variety of electronic devices and communication systems.²¹⁶ SAW resonators typically operate in the frequency range of several hundred megahertz (MHz) to a few gigahertz (GHz) (typically <6 GHz), based on the harmonic vibrations propagating from the surface into the bulk, excited by interdigital transducers (IDTs) on a piezoelectric substrate.²¹⁷ These devices exhibit good sensitivities to environmental perturbations such as temperature, pressure,²¹⁸ and humidity.²¹⁹ Due to their passivity, absence of wiring, and high precision, SAW sensors are particularly suitable for harsh environments with high temperatures or in radiative environments, making them highly sought-after in industries such as aerospace, automotive, and energy.^{220,221} One of the primary obstacles facing this technology is the substantial loss that occurs at high frequencies and the relatively low electromechanical coupling in the resonant mode. These limitations hinder their scalability to much higher frequency ranges and related applications.

Bulk-mode vibrations are generated by longitudinal standing waves or shear waves, resulting in deformations in the forms of planar expansions or contractions.^{222–227} Common bulk-mode resonators

TABLE I. Structure, device image, mode shape, and resonance frequency of MEMS resonators operating in flexural mode, torsional mode, and surface mode.²⁷⁶ (Wang et al., Transducers (2017). Copyright 2017 IEEE, Creative Commons), and bulk mode²⁷⁷ (Liu et al., Micromachines **11**, 12 (2020), Open Access),²⁷⁸ (Liu et al., Sensors **23**, 3808 (2023), Open Access),²⁷⁹ (Wu et al., J. Microelectromech. Syst. **21**, 6 (2012), Copyright 2012 IEEE, Creative Commons),²⁸⁰ (Park et al., IEEE International Ultrasonics Symposium (IUS) (2019). Copyright 2019 IEEE, Creative Commons),²⁸¹ (Gao et al., Micromachines **13**, 102 (2022), Open Access).

Vibration modes	Structure	Device image	Mode shape	Resonance frequency	Parameters
Flexural mode	Doubly-clamped beam			$f_n = \frac{\pi(n+0.5)^2}{2L^2} \sqrt{\frac{E_Y I}{\rho w t}} \times \sqrt{1 + \frac{0.97 \sigma w t L^2}{(n+1)^2 \pi^2 E_Y I}}$	n : Mode number L : Length E_Y : Young's modulus ρ : Mass density
	Cantilever			$f_n = \frac{(k_n L)^2}{2\pi L^2} \sqrt{\frac{E_Y I}{\rho A}}$	w : Width t : Thickness σ : Stress
	Drumhead			$f_n = \left(\frac{k_n r}{2\pi} \right) \sqrt{\frac{D}{\rho t r^4} \left[(k_n r)^2 + \frac{\gamma r^2}{D} \right]}$	I : Moment of inertia
Torsional mode	Paddle and tethers			$f = \frac{1}{2\pi} \sqrt{\frac{2J_T G}{L T I}}$	$k_n r$: numerically calculated modal parameter A : Cross-sectional area
Surface mode	SAW resonator			$f = v/\lambda$	r : Radius D : Flexural rigidity
	Rectangular plate (Length-extensional)			$f_n = \frac{n}{2L} \sqrt{\frac{E_Y}{\rho}}$	γ : built-in tension v : Acoustic wave velocity
Bulk mode	Rectangular plate (Width-extensional)			$f_n = \frac{n}{2w} \sqrt{\frac{E_Y}{\rho}}$	λ : Wavelength G : Shear modulus
	Square plate (Lamé mode)			$f_0 = \frac{1}{\sqrt{2}L} \sqrt{\frac{G}{\rho}}$	d_p : thickness of piezoelectric layer k_n : n^{th} mode coefficient
	FBAR/SMR			$f_a = v/2d_p$	J_T : torsional area moment of inertia
	Circular disk (Radial breathing)			$f_0 = \frac{k_n}{2\pi r} \sqrt{\frac{E_Y}{\rho(1-\sigma^2)}}$	$J_T = w_T t^3 \times \left(\frac{1}{3} - 0.21 \times \frac{t}{w_T} \times \left(1 - \frac{w_T^4}{12 \times t^4} \right) \right)$
	Lamb wave resonator			$f = v/\lambda$	L_T : tether length of a paddle w_T : tether width of a paddle

include beams, rectangular plates, square disks, and circular plates operating in length-extensional (LE) mode,^{228–230} width-extensional (WE) mode,^{231–234} square-extensional (SE) mode,^{235–238} radial breathing mode,²³⁹ Lamé mode,^{240–246} etc., with the resonance frequency determined by physical dimensions, such as width, length, thickness, and radius. Bulk mode has much higher structural stiffness compared to flexural mode, enabling high resonance frequencies in the GHz range without necessarily scaling the dimensions into the nanometer

range. Therefore, bulk-mode resonators usually have a smaller surface-to-volume ratio, which simplifies fabrication and reduces surface loss.²⁴⁷ Film-bulk acoustic resonator (FBAR) represents a prominent example of bulk acoustic wave (BAW) devices, comprising a piezoelectric layer sandwiched between two metal electrodes.^{248–250} To operate the FBAR on a substrate, it is essential to acoustically isolate the active area of the device from the substrate. This is achieved through either a Bragg mirror layer or an air cavity as effective reflectors. The BAW

device with an acoustic Bragg reflector is known as a solidly mounted resonator (SMR). By combining favored piezoelectric properties with the appropriate thickness of the piezoelectric layer, FBARs can resonate in the frequency range of sub-GHz to 20 GHz and are widely used in building filters for RF systems.²⁵¹ Fabricating multi-frequency FBARs on a single chip presents challenges due to the direct correlation between resonance frequency and the thickness of piezoelectric layer. Techniques such as trimming and mass-loading are widely employed to adjust the resonance frequency, thus enabling on-chip frequency diversity.^{252,253} However, these methods necessitate intricate and costly fabrication processes, often involving multiple lithographic steps. Moreover, the precision required for these steps is already in the angstrom range for devices operating below 6 GHz. Consequently, simple scaling of this technology may not be easily feasible for super-high-frequency applications.^{254–256}

Lamb wave resonators (LWRs) harness superpositions of longitudinal and shear waves propagating in a plate, with the resonance frequencies defined by in-plane dimensions.^{257–259} These devices were initially implemented on LiNbO₃ and AlN material platforms. The interdigital transducers (IDTs) consist of two sets of parallel electrodes separated by small gaps, which create an electric field that generates mechanical vibrations in the piezoelectric plate. As the acoustic wave propagates through the plate, it reflects back-and-forth between the IDTs, leading to constructive interference and resonant amplification at specific frequencies.^{260–262} By adjusting the geometrical parameters of the IDTs, such as the IDT finger width and spacing, the thickness of the piezoelectric plate, and the electrode material, the resonance frequency and Q of the LWR can be tuned to meet the requirements of various applications.^{263–265} Compared to BAW resonators, LWR offers a distinct advantage in that it can be implemented on a lateral field-excited configuration without the need for a bottom floating electrode.^{266–268} This simplifies the micromachining process considerably, reducing complexity and cost. The combination of IDTs and piezoelectric materials makes LWR a promising technology for a wide range of applications, including wireless communication, sensing, and signal processing.^{269–271} LWR based on AlN operating in the fundamental mode and overtones at 11 and 23 GHz have been demonstrated with Qs of 600 and 250, respectively.²⁷² However, one of the main challenges of AlN LWRs is their relatively low electromechanical coupling coefficient. To address this issue, researchers have explored various approaches, including alloying AlN with Scandium (Sc), which has been shown to effectively enhance the k_t^2 coefficient in recent years.^{273–275}

IV. THEORETICAL ANALYSIS OF TCf FOR MEMS WITH DIFFERENT STRUCTURES

The TCf of a MEMS resonator can be influenced by multiple factors, including material properties (temperature coefficient of elasticity, density, thermal expansion coefficient of materials, etc.), resonator geometry (dimensions, shape, mode of vibration, etc.), anchor design, electrode placement, environmental conditions (pressure, humidity, etc.), and packaging.^{282–287} It is essential to take all of these factors into account when designing MEMS resonators to ensure that they have desirable TCf characteristics for specific applications.^{288–290} However, theoretical analysis of TCf is limited to MEMS with simple structures due to the complex effects of the various factors and the lack of studies on material properties at different temperatures.^{291–294} This section offers a comprehensive summary of the TCf characteristics of

commonly used MEMS structures, including beams, cantilevers, membranes, circular disks, SAW, and LWR. The presented information may provide a valuable resource that can help guide and assist designers in developing MEMS resonators with desired TCf characteristics.

A. TCf of doubly clamped structure

The multimode resonance frequencies of doubly clamped structures can be expressed as

$$f_n = \frac{\pi(n + 0.5)^2}{2L^2} \sqrt{\frac{E_Y I}{\rho w t}} \sqrt{1 + \frac{0.97 \sigma w t L^2}{(n + 1)^2 \pi^2 E_Y I}}, \quad (4.1)$$

where n denotes the mode number, ρ is the material mass density, $I = wt^3/12$ is the moment of inertia, σ refers to the built-in stress (N/m² or Pa), w is the width, t is the thickness, and L is the length of doubly clamped structure.^{295–299} Equation (4.1) yields a mixed elasticity model, in which both flexural rigidity (dominated by the thickness and elastic modulus) and built-in stress play key roles in determining the resonance frequency.

1. Flexural rigidity dominated resonance

When flexural rigidity is dominant in elasticity, the resonance frequency of the n_{th} out-of-plane flexural mode can be expressed as

$$f_n = \frac{(k_n L)^2}{4\sqrt{3}\pi} \frac{t}{L^2} \sqrt{\frac{E_Y}{\rho}}, \quad (4.2)$$

where $k_n L$ is the eigenvalue for the n_{th} flexural mode. Numerical calculation gives $k_1 L = 4.730$, $k_2 L = 7.853$, and $k_3 L = 10.996$ for the first three modes.

The temperature coefficient of frequency is given by

$$\text{TC}f_n = \frac{1}{f_n} \frac{df}{dT} = \frac{1}{2} (\text{TCE}_Y + \alpha), \quad (4.3)$$

where TCE_Y is the temperature coefficient of Young's modulus, which is defined as $(1/E_Y)(dE_Y/dT)$, and α is the linear coefficient of thermal expansion.

2. Stress dominated resonance

When built-in stress is dominant in elasticity, the resonance frequency of the n_{th} flexural mode can be modeled using the string model,

$$f_n = \frac{n}{2L} \sqrt{\frac{\sigma}{\rho}}, \quad (4.4)$$

As suggested by Eq. (4.4), the multimode resonances should have the ratios of 1:2:3..., and the resonance is dominated by the built-in stress while independent of E_Y . The temperature coefficient of frequency can be written as

$$\text{TC}f_n = \frac{1}{f_n} \frac{df}{dT} = \frac{\alpha E_{Y0}}{2\sigma_0 \left(1 - \frac{\alpha E_{Y0}}{\sigma_0} T\right)}, \quad (4.5)$$

where σ_0 is the initial stress and E_{Y0} is the Young's modulus at reference temperature.

B. TCf of cantilever

Micro-cantilevers are useful test structures for determining how E_Y varies with temperature through resonant frequency measurement. The resonance frequency f_n of each flexural mode of the cantilever with length L and thickness t can be obtained by

$$f_n = \frac{(k_n L)^2}{4\sqrt{3}\pi} \frac{t}{L^2} \sqrt{\frac{E_Y}{\rho}}, \quad (4.6)$$

where $k_n L$ are the non-trivial solutions of $1 + \cos k_n L \cosh k_n L = 0$. Numerical calculation gives $k_1 L = 1.875$, $k_2 L = 4.694$, and $k_3 L = 7.855$ for the first three modes. Equation (4.6) indicates that the resonance frequency of cantilevers is dependent on the geometric dimensions (i.e., the thickness and length of the cantilever), the Young's modulus, and the material density.

The temperature coefficient of frequency can be written as

$$\text{TC}f_n = \frac{1}{f_n} \frac{df}{dT} = \frac{1}{2} (\text{TCE}_Y + \alpha). \quad (4.7)$$

Due to inevitable microfabrication errors, the supporting layer near the base (or anchor) of the cantilevers can be undercut in the etching process used to release the cantilevers, which can affect the resonant frequency of the cantilevers. However, if the undercut is comparatively smaller than the width of the cantilevers, it is reasonable to treat the undercut as an extension of the cantilever by a length ΔL . Although the undercut results in the shift of resonance frequency, the $\text{TC}f$ remains the same as that shown in Eq. (4.7) since the normalized change in frequency is used, and both L and $(L + \Delta L)$ will change by the same rate of thermal expansion. By experimentally measuring the temperature dependence of resonance frequency, $\text{TC}f$, TCE_Y , and the coefficient of thermal expansion (CTE), α can be quantitatively determined.

C. TCf of circular drumhead

The multimode resonance frequencies of a circular diaphragm resonator can be expressed as³⁰⁰

$$f_n = \left(\frac{k_n r}{2\pi} \right) \sqrt{\frac{D}{\rho t^4}} \left[(k_n r)^2 + \frac{\gamma r^2}{D} \right], \quad (4.8)$$

where n denotes the mode number, ρ is the material mass density, t is the device thickness, $k_n r$ is the numerically calculated modal parameter, r is the radius of circular diaphragm, γ refers to the built-in tension [in N/m, or stress (N/m² or Pa) multiplied by thickness], and D is the flexural rigidity, $D = E_Y r^3 / [12(1 - \nu^2)]$ in which E_Y and ν are Young's modulus and Poisson's ratio, respectively. Equation (4.8) yields a mixed elasticity model, in which both flexural rigidity (dominated by the thickness and elastic modulus) and built-in tension (stress) play key roles in determining the resonance frequency. When $\gamma r^2 / D$ is very large and dominates in Eq. (4.8), Eq. (4.8) goes in the membrane regime, in which the frequency is dominated by the built-in tension. The $\text{TC}f$ of tension dominant limit can be derived as

$$\text{TC}f_n \approx \frac{\alpha}{2} - \frac{\alpha E_{Y0}}{2\sigma_0}, \quad (4.9)$$

where α refers to the CTE, σ_0 is the initial stress at reference temperature, and E_{Y0} is the Young's modulus at reference temperature.

As $\gamma r^2 / D$ becomes negligible in Eq. (4.8), flexural rigidity dominates the frequency, i.e., and the model approaches the plate or disk regime. The $\text{TC}f$ in the flexural rigidity dominated limit can be derived as

$$\text{TC}f_n \approx \frac{3\alpha}{2} + \frac{\text{TCE}_Y}{2}. \quad (4.10)$$

When the device resonates in the transition region between these two regimes, the variation of $\text{TC}f$ with temperature can be ascribed to the intricate competing effects of temperature induced changes in CTE, built-in stress, and Young's modulus.

D. TCf of surface acoustic wave resonator

For a surface acoustic wave (SAW) resonator, intrinsic first-order $\text{TC}f$ is given by^{301,302}

$$\text{TC}f = \frac{1}{f_0} \frac{df}{dT} = \text{TC}v_p - \alpha_{11}, \quad (4.11)$$

where $\text{TC}v_p$ is the temperature coefficient of velocity, and α_{11} is the in-plane CTE along a -axis. In the case of a thin film, i.e., a thinner layer compared to the bulk substrate, its thermal expansion is governed by the substrate's in-plane CTE.

SAW $\text{TC}v_p$ can be approximated by

$$\begin{aligned} \text{TC}v_p &= \frac{1}{v_{p,\text{ref}}} \frac{\partial v_p}{\partial T} = \sum \frac{w_{ij}}{c_{ij,\text{ref}}} \frac{\partial c_{ij}}{\partial T} - \frac{1}{2} \frac{1}{\rho_{\text{ref}}} \frac{\partial \rho}{\partial T} \\ &= \sum \frac{w_{ij}}{c_{ij,\text{ref}}} \frac{\partial c_{ij}}{\partial T} + \frac{\alpha_{33}}{2} + \alpha_{11}, \end{aligned} \quad (4.12)$$

where v_p is the SAW phase velocity and $v_{p,\text{ref}}$ is v_p at reference temperature. The sum includes the w_{ij} -weighted contributions of several temperature coefficients of elasticity (TCE_Y) of the elastic constants c_{ij} . ρ is the mass density and ρ_{ref} is the mass density at room temperature. α_{33} is the out-of-plane or c -axis CTE of the material.

In general, contribution of TCE_Y to the $\text{TC}f$ is an order of magnitude larger than that of CTE because of the relatively large value of the TCE_Y , and despite their lower weights as seen in

$$\text{TC}f \approx \frac{0.09}{c_{11,\text{ref}}} \frac{\partial c_{11}}{\partial T} + \frac{0.07}{c_{33,\text{ref}}} \frac{\partial c_{33}}{\partial T} + \frac{0.36}{c_{44,\text{ref}}} \frac{\partial c_{44}}{\partial T} + \frac{\alpha_{33}}{2}, \quad (4.13)$$

where c_{11} and c_{33} are the axial elastic constants and c_{44} is the shear elastic constant, with $c_{11,\text{ref}}$, $c_{33,\text{ref}}$, and $c_{44,\text{ref}}$ being their values at room temperature, respectively.

E. TCf of Lamb wave resonator

The resonance frequency of a Lamb wave resonator can be expressed as

$$f = v_p / \lambda, \quad (4.14)$$

where v_p is the Lamb wave phase velocity, and λ is the wavelength. The phase velocity v_p of A_0 -mode Lamb wave propagating in an isotropic non-piezoelectric thin plate with thickness h ($h/\lambda \ll 1$) is theoretically given by³⁰³

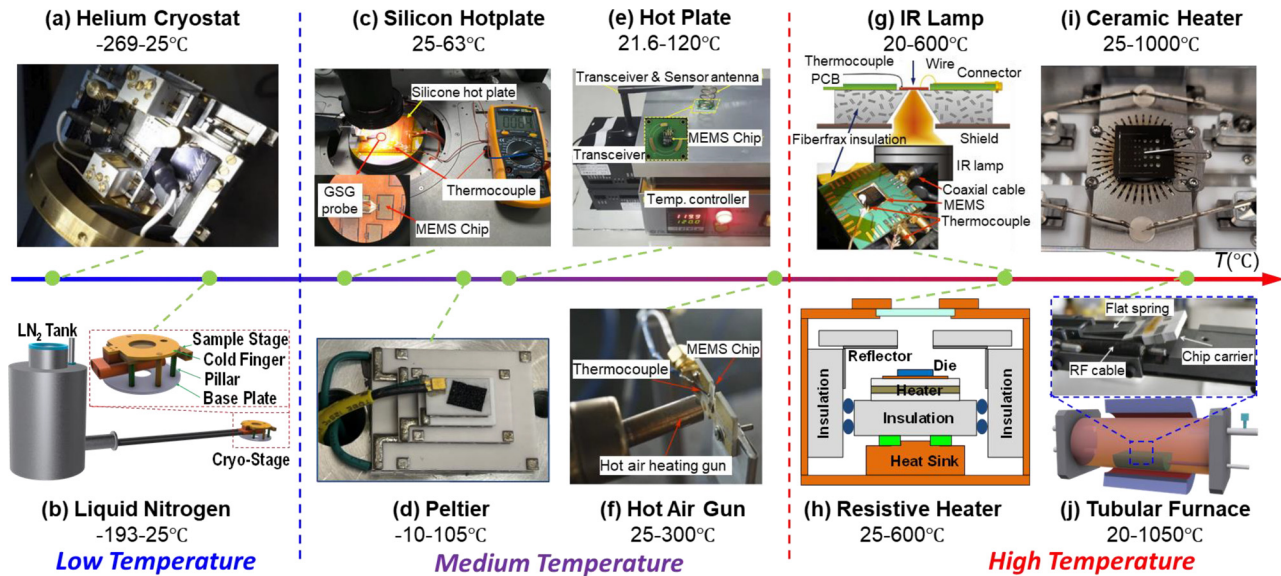


FIG. 2. Temperature regulation techniques. Low temperature environment obtained through (a) cryostat (Bolideu *et al.*, IEEE Access **10** (2022). Open Access)³⁰⁷ and (b) liquid nitrogen. Medium-temperature regulation by (c) silicon hotplate (Hu *et al.*, Solid-State Electron **150** 28 (2018). Copyright 2018 Elsevier, Creative Commons),³⁰⁸ (d) Peltier stage,³⁴ (e) Hot plate (Lv *et al.*, J. Semicond. **43**, 114101 (2022). Copyright 2022 Chinese Institute of Electronics, Creative Commons),³¹³ and (f) hot air gun (Wang *et al.*, Transducers (2017). Copyright 2017 IEEE, Creative Commons).³⁷⁶ High-temperature regulation achieved using (g) IR lamp (Ren *et al.*, IEEE MEMS (2010). Copyright 2010 IEEE, Creative Commons),³¹⁰ (h) resistive heater with insulation (Pozzi *et al.*, J. Phys. D: Appl. Phys. **40**, 3335 (2007). Copyright 2007 IOP Publishing, Creative Commons),³¹¹ (i) ceramic heater,³¹² and (j) tubular furnace (Aubert *et al.*, J. Appl. Phys. **114**, 014505 (2013). Copyright AIP Publishing, Creative Commons).³¹⁴

$$v_p = 2\pi \frac{h}{\lambda} \left(\frac{E_Y}{3\rho(1-\nu^2)} \right)^{1/2}, \quad (4.15)$$

where E_Y , ν , and ρ are Young's modulus, Poisson's ratio, and the mass density of the thin plate, respectively. TCf is given by

$$TCf_{LWR} = \frac{1}{f} \frac{\partial f}{\partial T} = \frac{1}{v_p} \frac{\partial v_p}{\partial T} - \frac{1}{\lambda} \frac{\partial \lambda}{\partial T} = \frac{1}{2E'} \frac{\partial E'}{\partial T} - \frac{1}{2\rho} \frac{\partial \rho}{\partial T} - \alpha, \quad (4.16)$$

where T is temperature, $E' = E_Y(1-\nu^2)$, and α is the CTE in the wave propagation direction.

In linear approximation, the temperature dependent density ρ can be defined as

$$\rho(T) = \rho(T_0)(1 - (\alpha_{11} + \alpha_{22} + \alpha_{33})\Delta T). \quad (4.17)$$

For a stack of i layers ($i = 1, 2, 3, \dots$), the effective E' , ρ , and α are approximated as follows

$$E'_{\text{eff}} = \frac{\sum_i E'_i h_i}{\sum_i h_i}, \quad \rho_{\text{eff}} = \frac{\sum_i \rho_i h_i}{\sum_i h_i}, \quad \text{and} \quad \alpha_{\text{eff}} = \frac{\sum_i E_i h_i \alpha_i}{\sum_i E_i h_i}, \quad (4.18)$$

where h_i represents the thickness of each layer.

F. Temperature coefficient of Young's modulus

Generalized Hooke's law defines the relationship between the stress and strain in a material with proportionality constants

$$[\epsilon] = [s] \cdot [\sigma], \quad (4.19)$$

where $[\sigma]$ and $[\epsilon]$ are the stress and strain vectors, respectively, while $[s]$ represents the compliance matrix. For isotropic materials, the Young's

modulus is simply defined as the inverse of s_{11} . In the case of anisotropic materials, such as Si, which possess a cubic crystal structure, the compliance matrix $[s]$ contains three independent elastic constants, namely, s_{11} , s_{12} , and s_{44} . The Young's modulus in different crystal orientations can be calculated by^{304,305,319}

$$E_Y(hkl) = \frac{1}{s'_{11}}, \quad (4.20)$$

where $s'_{11} = s_{11} - 2[(s_{11} - s_{12}) - \frac{1}{2}s_{44}] \times (m^2 n^2 + n^2 p^2 + m^2 p^2)$. m , n , p are the cosines of the angle formed between the particular direction of interest [h, k, l] and the x, y, and z axes. Although the Young's modulus of Si is dependent on the crystal orientation, it has been reported that the temperature coefficient of Young's modulus (TCE_Y) can be orientation independent.³⁰⁵ The temperature coefficient of elastic constants of single crystal Si has been extensively studied over the years. However, there are large variations in the reported results. The temperature coefficient of s_{11} (TCs_{11}) has been reported ranging from 52 to 100 ppm/ $^{\circ}\text{C}$.³⁰⁵

In 1961, a semi-empirical formula was proposed to describe the thermal response of Young's modulus³⁰⁶

$$E_Y = E_{Y0} - BT \exp\left(-\frac{T_0}{T}\right), \quad (4.21)$$

where E_{Y0} is the value of Young's modulus at absolute zero temperature, B is a temperature independent constant related to the bulk modulus, and T_0 is an empirical parameter related to the Debye temperature.

V. TEMPERATURE REGULATION TECHNIQUES

There are several commonly used temperature regulation techniques for MEMS TCf studies, as summarized in Fig. 2. The selection of

a temperature regulation technique primarily depends on the specific requirements, including the size and geometry of the sample, the temperature range to be covered, and the desired level of temperature control. Proper selection and implementation of a heating method can greatly enhance the accuracy and reliability of TCf measurements and provide valuable insight into the thermal behavior of MEMS devices.

To study the performance of MEMS devices at low temperatures, it is essential to maintain the sample or device under test (DUT) in a vacuum to prevent frost during cooling, as the additional mass from the frost can shift the resonance frequency. There are several methods available to cool samples. One common approach is mounting the sample on a copper cold finger cooled by a bath of liquid nitrogen [Fig. 2(b)]. The temperature of the stage is monitored by a thermocouple, which is positioned beneath the sample and encased within the cold finger. This cooling method was employed in studying the TCE_Y of single crystal Si and 3C-SiC micro-cantilevers below room temperature.³⁰⁵ As shown in Fig. 2(a), cryostats that use recirculating helium (He) have become increasingly popular for low temperature measurement down to ~ 5 K. In this type of cryostat, helium gas is continuously circulated through a closed-loop system, which cools the sample without depleting the helium. The gas is first compressed and then cooled using a refrigeration system, before being pumped through a series of heat exchangers to cool the sample to the desired temperature.³⁰⁷ Compared to the traditional liquid nitrogen method, the recirculating helium approach offers several advantages. First, recirculating helium cryostats can achieve much lower temperatures than the liquid nitrogen method (~ 80 K). Second, the recirculating helium method is more sustainable and efficient as the helium gas is continuously recirculated, not consumed. In contrast, the liquid nitrogen method requires frequent replenishment of the liquid, which can be both costly and time-consuming. Finally, the recirculating helium method provides a more stable and uniform cooling environment, which is crucial for many scientific experiments. However, it should be noted that the initial cost of a helium cryostat is usually higher than that of a liquid nitrogen system, and the complexity of the cryostat system requires a higher level of maintenance and technical expertise to operate. Additionally, there is a risk of helium leaks, which can be hazardous and require careful handling.

Most of the published literature studying the thermal response of MEMS resonators is still limited to a low-temperature range, i.e., below 150 °C. A widely used heating scheme is shown in Figs. 2(c)–2(e), where the temperature is adjusted by a hot plate made of silicone,³⁰⁸ a Peltier stage,⁶⁴ or a ceramic heater.³⁰⁹ The temperature is monitored by a thermocouple fixed on the hot plane next to the measured MEMS die. Ceramic heaters are often used in laboratory settings and offer precise temperature control, with temperature ranges up to 300 °C. Peltier devices, on the other hand, can both heat and cool MEMS chips, providing greater flexibility in temperature control. Peltier devices can typically achieve temperature ranges from a few tens degrees below 0 °C to around 200 °C. The main advantage of this kind of measurement system is that no complex components are needed so that it is a quick and easy way to heat up the MEMS chip. Despite the advantages of hot plate heating, achieving uniform heating across the surface of larger MEMS devices remains a challenge. The highest temperature is typically limited below 300 °C.

Hot air gun heating technique involves directing a focused stream of heated air onto the device to heat it. The hot air gun can be used to

heat a specific area of the device and can achieve temperatures up to a few hundred degrees Celsius. This method is particularly useful for heating small areas and allows for precise temperature control. It is a low-cost and easily accessible method for heating MEMS devices. Additionally, it can be used to achieve fast and localized heating, which is convenient for thermal analysis of small devices. This method has been demonstrated in testing the high-temperature responses of SAW resonators based on AlN/6H-SiC from 25 °C to 300 °C [Fig. 2(f)].²⁷⁶ However, one of the challenges of hot air gun heating is achieving uniform heating across the MEMS device's surface, particularly for larger devices.

Infrared (IR) heating is commonly used in industrial settings. Infrared lamps emit heat in the form of electromagnetic radiation, which can be directed at a large area of the device to achieve uniform heating. This technique can attain temperature ranges of up to several hundred degrees Celsius, making it suitable for TCf studies that require moderate to high temperatures. One of the advantages of infrared heating is that it is relatively easy to set up and can achieve uniform heating over a large area of the device. One of the challenges of this method is achieving precise temperature control, particularly for small MEMS devices. Additionally, the heating and cooling rate of the MEMS device can impact the accuracy of TCf measurement requiring careful calibration of the heating process. This heating scheme has been utilized to achieve localized heating of the AlN LWRs in ambient conditions from 20 °C to 600 °C. As illustrated in Fig. 2(g), the MEMS die is mounted with ceramic adhesive to a thermally insulating Fiberfrax substrate. A small hole is drilled on the Fiberfrax substrate, which enables access to the MEMS die from the backside. An IR lamp at the focal point is utilized to heat the device for maximum heat intensity.³¹⁰ Similarly, laser heating is another precise and localized method for heating MEMS devices. A laser beam is directed at a specific area of the device, heating it to a precise temperature. This technique is efficient and precise for heating small and specifically focused areas of the device and can achieve very high temperatures, typically up to several thousand degrees Celsius. One of the advantages of laser heating is its precise temperature control, which allows for accurate TCf measurements. However, it is challenging to achieve uniform heating across the MEMS device's surface, especially for larger devices. Additionally, laser heating can be expensive and requires specialized equipment, making it sometimes less accessible compared to other heating methods.

Joule heating is a method of heating MEMS devices by passing electric currents through them. This technique is useful for heating specific areas of the device and can achieve precise temperature control. The temperature range typically achieved with Joule heating can be up to several hundred degrees Celsius. One of the advantages of Joule heating is that it is relatively easy to set up and can achieve localized heating. However, one of the challenges is achieving uniform heating across the MEMS device's surface, especially for larger devices.

Precise temperature can be achieved by a specially designed ceramic resistive heater with proportional-integral-derivative (PID) temperature controller, which has been demonstrated with good temperature accuracy up to 600 °C [Fig. 2(h)]. To suppress the heat loss through radiation at higher temperature, one effective way is to surround the heater/sample system by insulating/reflecting material. A mineral insulated thermocouple is placed in contact with the top surface of the die to monitor the surface temperature (T_1), while a second

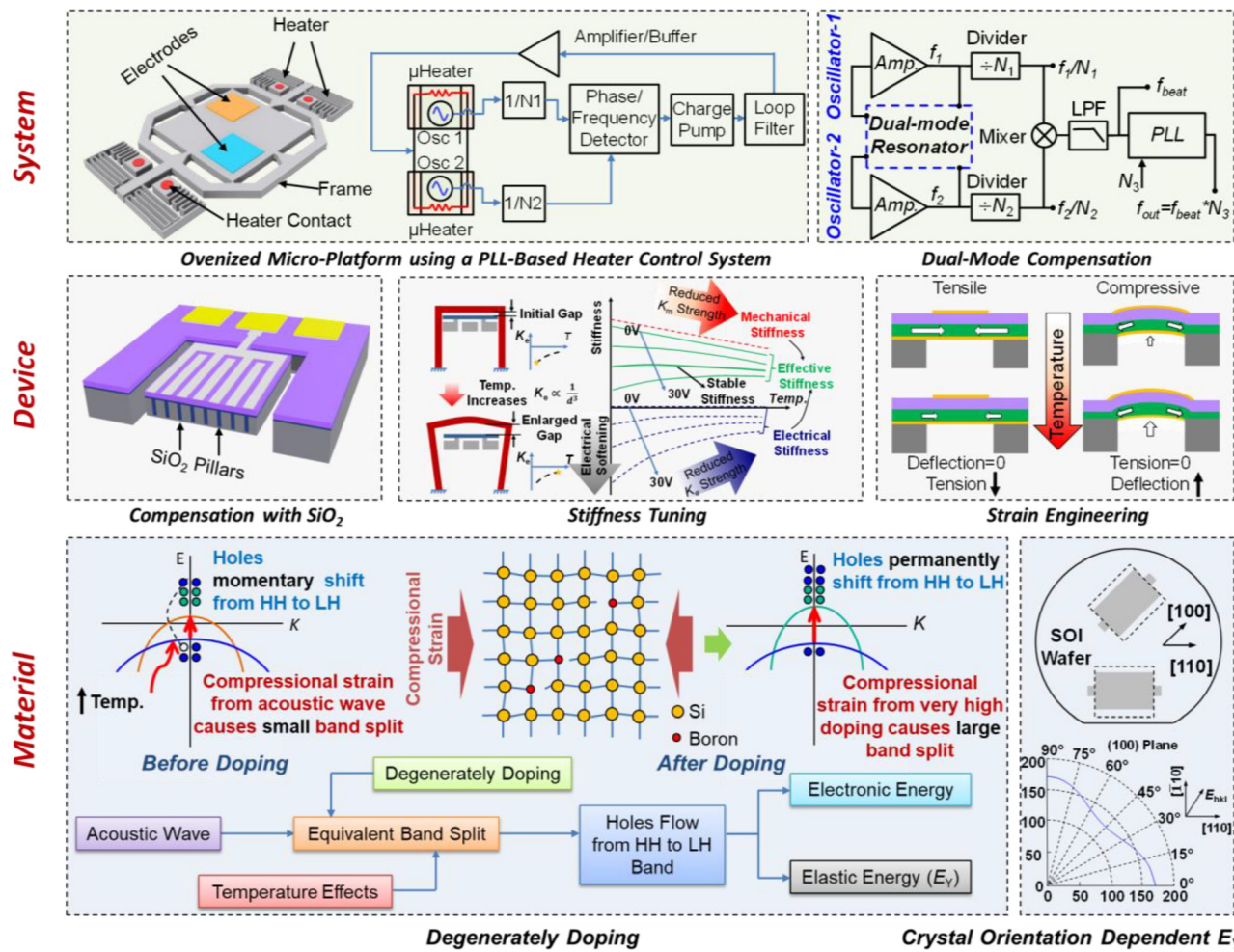


FIG. 3. Temperature compensation techniques at the material level³¹⁹ (Hopcroft *et al.*, J. Microelectromech. Syst. **19**, 2 (2010). Copyright 2010 IEEE, Creative Commons), within the device level³²¹ (Liu *et al.*, J. Micromech. Microeng. **30**, 014002 (2020). Copyright 2020 IEEE, Creative Commons), and during the post-device stage³²⁵ (Kwon *et al.*, J. Microelectromech. Syst. **24**, 2 (2015). Copyright 2015 IEEE, Creative Commons);³²⁸ (Li *et al.*, Transducers (2019). Copyright 2019 IEEE, Creative Commons).

thermocouple is placed a few millimeters away in close contact with the ceramic plate to measure the surface temperature of the heater (T_2). The real temperature of the devices (T_R) lies near the two temperatures read from the two thermocouples (T_1 and T_2). T_2 is always expected to be higher than T_1 due to heat transfer. This temperature difference is related to the contact situation between the chip and heater, the thickness of the chip, and the thermal conductivity of the material. A temperature gap larger than 50 °C has been observed when a copper sheet is present between the SiC-on-Si chip and the heater. This gap becomes much smaller when the sample is directly contacting the heater, with $T_1 \approx T_2$ up to 500 °C.³¹¹ With further optimization, the highest temperature of the state-of-the-art ceramic heater can reach ~1000 °C [Fig. 2(i)].³¹²

Oven or furnace heating is a widely used method for conducting TCf studies on MEMS devices. The technique involves subjecting the device to a specific temperature and maintaining it at that temperature for a predetermined duration using an oven or furnace, as shown in

Fig. 2(j). One of the significant advantages of using the oven or furnace heating method is its ability to achieve a wide temperature range, from room temperature up to several hundred degrees Celsius or even higher than 1000 °C. This feature makes it suitable for studying the TCf of MEMS devices that operate under extreme temperature conditions. Additionally, the method provides excellent temperature uniformity throughout the device. Despite its advantages, a key challenge is achieving precise temperature control in compact systems. Further, the heating and cooling rate of the MEMS device can affect the accuracy of the TCf measurement, necessitating careful calibration of the heating process. A higher temperature up to 1050 °C has been achieved by using a tubular furnace in the study of *in situ* high-temperature characterization of AlN-based SAW.³¹⁴ First, the MEMS chip is bonded with platinum (Pt) wires to platinum foil strips attached to a RescorTM ceramic carrier platelet. Then the carrier is clamped to an RF signal cables pair that can survive at high temperatures. Clamping is ensured by springs and a lid that allows electrical feedthrough between the RF

cables and the chip carrier platinum strips. Finally, the setup is inserted inside a tubular furnace.

VI. TEMPERATURE COMPENSATION TECHNIQUES

Temperature variations can noticeably affect the resonance frequencies of MEMS resonators, which compromises the accuracy and reliability of the functions of such micromechanical systems. To address this issue, several compensation techniques have been developed, primarily categorized as active and passive methods for temperature compensation. Active methods involve the use of external feedback systems to adjust the driving signal and compensate for temperature variations in real time. Passive methods, on the other hand, use structural or material modifications to counteract the thermal effects on the resonance frequencies. Alternatively, these compensation techniques can be categorized into three distinct stages: at the material level, device level, and during the post-device stage. A summary of temperature compensation techniques is shown in Fig. 3. Experimental demonstrations have shown that these compensation methods can significantly enhance the stability and precision of MEMS resonators, making them more suitable for a wide range of applications in areas such as sensing, communication, and timing.³¹⁵

At the material level, the use of degenerately doped Si has been presented as an effective approach to compensate for temperature variations. When an acoustic wave propagates through a solid material, it generates a set of compressional and dilatational forces that can disturb the periodicity of the atomic lattice. In semiconductors such as Si, this perturbation can induce an impact on its electronic band structure. At steady-state, the valence band of Si consists of three energy surfaces in k -space, with two of them being degenerate and energetically favorable to be occupied with holes. The strain induced by the acoustic wave can split the equivalent bands, leading to a flow of holes from the heavy-hole (HH) to the light-hole (LH) band. The net flow of holes increases with increasing temperature, which changes the electronic energy of the system. However, the principle of conservation of energy requires a corresponding temperature-dependent change in the elastic energy of the system, causing a reduction in stiffness (i.e., E_Y) and, therefore, the resonance frequency with increasing temperature. To minimize the effect of momentary strain on the energy band, a relatively larger permanent strain is created by doping. This leads to a significant permanent separation of the degenerate valence bands, with most of the holes occupying the higher energy band. As a result, the effect of the acoustic wave propagation on band splitting becomes minimal, since few holes are available for transition between energy bands, requiring much higher energy to make such a transition. As a result, the electrical and elastic energies of the resonating system become insensitive to temperature variation.^{316–318} An alternative approach involves the careful selection of an appropriate crystal orientation during fabrication. Si, being the prevailing material in MEMS applications, exhibits anisotropic crystalline behavior wherein its material properties vary with respect to the orientation relative to the crystal lattice. Consequently, it is crucial to acknowledge that the accurate determination of E_Y , when analyzing distinct Si-based designs, may exhibit deviations of up to 45%.³¹⁹

Within device level, the most adopted method involves introducing an additional layer with a positive TCE_Y, such as silicon dioxide (SiO_2), under the piezoelectric material. Selecting an appropriate thickness ratio of the composite structures can compensate for the negative TCf. However, this method has a drawback of increasing the

fabrication complexity, and the introduced SiO_2 layer or embedded pillars can potentially degrade the performance of the MEMS resonator, resulting in a lower quality factor and a deteriorated electromechanical coupling coefficient. Despite these limitations, passive temperature compensation technology remains a promising approach for compensating temperature variations in MEMS resonators due to its simplicity and low power consumption.³²⁰

Stiffness compensation represents another passive technique employed to counteract the inherent negative TCf in structural materials by introducing an electrical stiffness exhibiting a positive temperature coefficient. This technique utilizes temperature-dependent gap spacing to induce the necessary electrical stiffness, compensating for the mechanical stiffness variation as temperature changes.³²¹ Notably, a distinctive advantage of stiffness compensation is its ability to preserve the original resonator material and structure. However, a primary drawback is the increased system design complexity. The incorporation of temperature-dependent gap spacing and the associated electrical stiffness mechanism requires meticulous engineering, potentially escalating manufacturing complexity and costs. Furthermore, the integration of electrical components within the overall system may pose additional challenges such as increased power consumption, reliability issues, and susceptibility to electrical failures.

Strain engineering has been demonstrated as another method to counteract temperature-induced frequency shifts in resonant MEMS devices, since the resonance frequency and TCf of a resonator are both related to the stress level.³¹⁵ A study on AlN-based flexural plate wave sensors showed that in-plane tension of the composite plate has a strong influence on the temperature stability. Devices with built-in compressive stress exhibited a TCf of -62 to $-28 \text{ ppm}^{\circ}\text{C}$ between room temperature and 80°C , while the devices with initially tensile film stress showed an increased TCf of -391 to $-72 \text{ ppm}^{\circ}\text{C}$. These results suggest that initially tensile film stress leads to a decrease in in-plane tension and constant zero deflection as temperature increases, while initially compressive film stress results in zero tension due to plate undulation and unchanged stress conditions as temperature increases.³²² One common method to induce stress is by utilizing the mismatch of the CTE of different materials, which has been demonstrated in double-clamped resonators.³²³

The varactor-based tuning method provides a highly effective solution for temperature compensation in MEMS resonators through voltage-controlled resonance frequency adjustment. Demonstrated for the first time on AlN capacitive-piezoelectric resonators with electrodes detached from the piezoelectric material, this technique achieves frequency shifts exceeding 1500 ppm.³²⁴ It leverages voltage-controlled gap reduction to precisely modulate the resonance frequencies of AlN micromechanical resonators. By incorporating variable capacitances

TABLE II. Comparison of material properties of commonly used electrodes.

Metal	ρ (kg/m ³)	E_Y (GPa)	κ (W/[m·°C])	α (°C ⁻¹)	Melting point (°C)
Al	2700	70	205	22.2×10^{-6}	660
Mo	10 280	312	138	5.35×10^{-6}	2623
Au	19 300	77	301	14.4×10^{-6}	1064
Pt	21 450	168	69.1	9.1×10^{-6}	1768

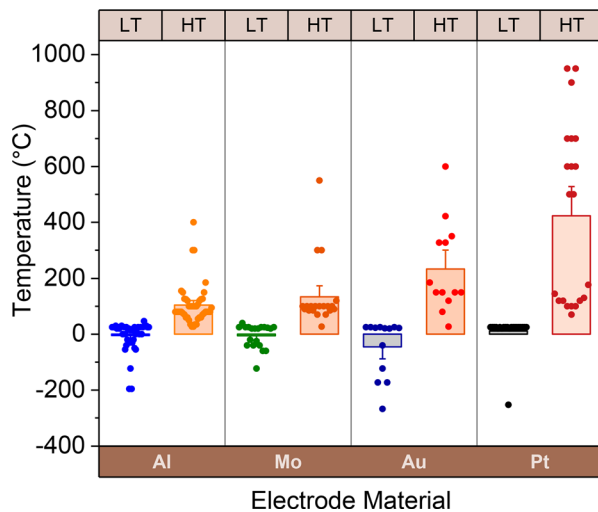


FIG. 4. Commonly used electrode at varying temperatures.

into the resonator structure, the method enables fine frequency tuning, enhances quality factors, and preserves strong electromechanical coupling. A key innovation is the compliant top electrode suspension, which responds to applied voltage by varying the capacitance in series with the device, thereby altering its series resonance frequency. This advanced approach offers significant promise for dynamic TCf compensation and precise frequency control in high-performance resonator applications.

At the system level, active compensation technologies, such as oven-controlled package and electronic phase-locked loop (PLL), have been shown to achieve high thermal stability at parts-per-billion (ppb) levels over a certain temperature range. Real-time temperature compensation is commonly achieved using an external reference device to track temperature changes with readout circuitry. However, this approach can lead to circuit complexity, a large footprint, and increased power consumption due to the additional electric components.³¹⁵ An alternative approach is self-temperature sensing, which involves monitoring two different modes of the same resonator or two tones produced by two resonators. By comparing the different temperature coefficients of the two modes or tones, a temperature-dependent beat frequency is generated, which is inherent to the devices and eliminates any spatial effect and thermal lag between the two devices, making it an effective method for active TCf manipulation.^{325,326} This approach offers the advantage of reduced circuit complexity and power consumption, making it an attractive option for MEMS device applications.³²⁷

VII. METALLIZATION EFFECTS

The metal electrode of a MEMS resonator can have a significant impact on its resonance frequency at varying temperatures. The CTE of the metal electrode material is a critical factor in determining the resonance frequency shift due to temperature changes. When the temperature increases, the metal electrode expands, causing a change in the stress level and strain distribution of the MEMS resonator. This changes the effective stiffness of the resonator, which in turn alters its resonance frequency. The frequency shift depends on the CTE of the

metal electrode material and its thickness. At high temperatures, the effect of the metal electrode on the resonance frequency becomes more significant. This is because the CTE of the metal electrode material typically increases with temperature, leading to a larger change in its dimensions. In addition, at high temperatures, the mechanical properties of the metal electrode can also change due to thermal annealing, such as changes in its hardness, yield strength, and creep behavior. These changes can further affect the MEMS resonator's stress, strain distribution, and resonance frequency. To mitigate the metal electrode's effect on resonance frequency at high temperatures, various techniques have been developed, such as using low CTE metals, designing low-stiffness electrode, and applying thermal compensation techniques. These methods aim to reduce the stress and strain induced by the metal electrode and maintain the effective stiffness of the resonator constant, thus minimizing the resonance frequency shift due to temperature changes.

Table II illustrates the comparison of material properties of aluminum (Al), molybdenum (Mo), gold (Au), and platinum (Pt). **Figure 4** summarizes the commonly used electrodes at varying temperatures. Al is a frequently used electrode material due to its small mass density ($\rho = 2700 \text{ kg/m}^3$) and low Young's modulus ($E_Y = 70 \text{ GPa}$). The deposition thickness of Al can be up to $1 \mu\text{m}$, which reduces the resistance of the Al interconnect. However, Al has a low melting point of 660°C , which is not preferred in harsh conditions, such as high temperatures up to 1000°C . Mo and Au have also been widely used as the electrodes for MEMS operating at higher temperatures. Nonetheless, most of the reported applications were tested at temperatures below 600°C .

Pt has garnered significant attention as an electrode for high temperature applications due to its relatively high melting temperature (1768°C), resistance to oxidation, nearly constant bulk resistance temperature coefficient, and the greatest chemical inertness among the noble metal family. However, Pt has a weak chemical affinity for other elements, leading to poor adhesion to oxide substrates. Typically, a very thin (10–20 nm) intermediate layer is needed to enhance the adhesion between the substrate and the platinum film. Titanium (Ti) has been utilized as an adhesion layer for Pt IDTs in GaN and AlScN-SiC LWRs operating at 800°C in a vacuum.^{329,330} However, its effectiveness is limited in air due to the diffusion of titanium into the Pt, which results in the formation of oxide precipitates (TiO_2) in the Pt grain boundaries. This modifies the electrical properties of the Pt IDTs and progressively degrades the adhesion layer, leading to delamination. The Pt/zirconium (Zr) combination has demonstrated better performance up to 700°C . However, this combination is inadequate for continuous operation at temperatures above 700°C due to the degradation originated from de-wetting phenomena. When replacing Pt with a Pt/10% rhodium (Rh) alloy, the combination of Pt/10% Rh alloy and Zr exhibited a very good stability up to 950°C .³³¹

Tantalum (Ta) has been used as an adhesion layer for platinum-based IDTs. Sputtered neutral mass spectrometry (SNMS) depth profile curves indicate that neither Ta nor oxygen plays a key role in the deterioration of the Pt. It is suggested that the deterioration of the Pt film is intrinsic and occurs at high temperatures, independent of the adhesion layer and the ambient gas mixture. X-ray diffraction (XRD) measurements show that the Pt layer strongly recrystallized during annealing. The deterioration of the Pt/Ta electrode originated from agglomeration phenomena in the Pt layer, resulting in the breakage of

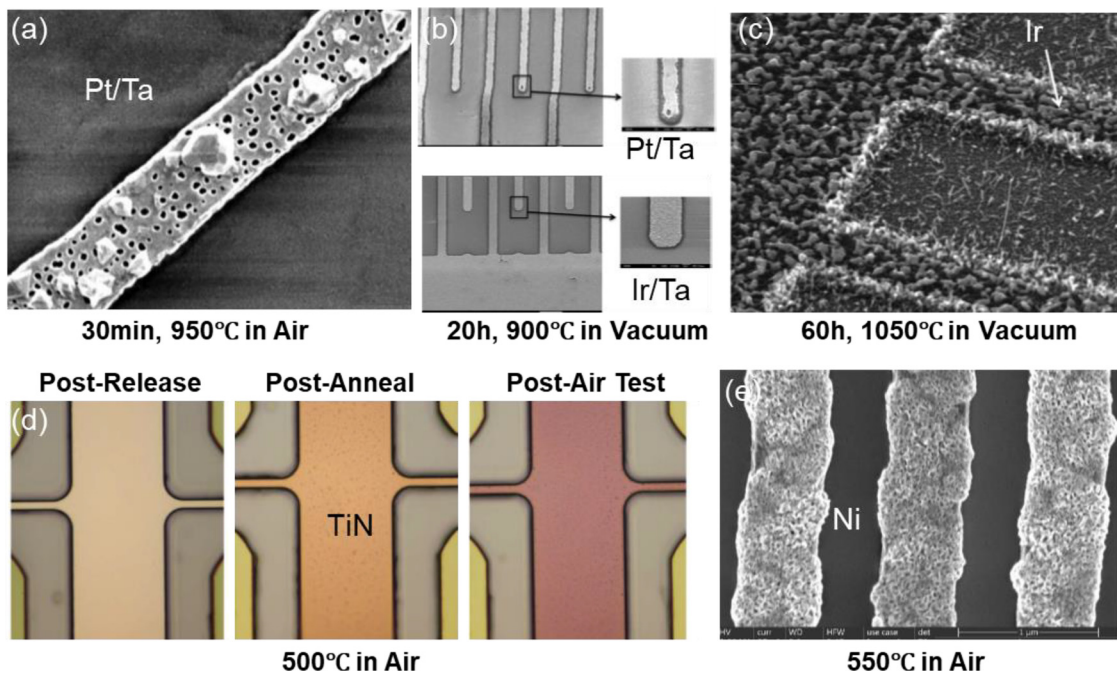


FIG. 5. Electrode degradation at high temperature. (a) SEM images of Pt/Ta electrodes after annealing at 950 °C for 30 min. (Aubert *et al.*, *Appl. Phys. Lett.* **96**, 203503 (2010). Copyright AIP Publishing, Creative Commons).³³¹ (b) SEM images of Pt/Ta and Ir/Ti IDT after 20 h at 900 °C (Aubert *et al.*, *IEEE Trans. Ultrason. Ferroelectr. Freq. Control* **58**, 603 (2011). Copyright 2011 IEEE, Creative Commons).³³² (c) SEM images of Ir electrode after annealing at 1050 °C for 60 h in vacuum (Aubert *et al.*, *J. Appl. Phys.* **114**, 014505 (2013). Copyright AIP Publishing, Creative Commons).³¹⁴ (d) Image of TiN electrode after release, after annealing and before testing, and after *in situ* testing up to 500 °C in air (Esteves *et al.*, *J. Microelectromech. Syst.* **28**, 859 (2019). Copyright 2019 IEEE, Creative Commons).³³⁴ (e) SEM image of Ni electrodes after testing at 550 °C in air (Qamar *et al.*, *J. Microelectromech. Syst.* **29**, 900 (2020). Copyright 2020 IEEE, Creative Commons).³³⁵

29 June 2025 22:04:31

the Pt IDTs fingers and the loss of the SAW signal when operating at 950 °C in air [Fig. 5(a)].³³¹ A protective over-layer could slow down or even prevent agglomeration, protecting the Pt from oxygen and mechanically fixing the Pt nanocrystallites in place. Replacing Pt with iridium (Ir), which has a higher melting temperature of 2440 °C, has been verified as an effective way to avoid such problems. There is no trace of agglomeration on Ir/Ti IDTs after annealing for 20 h at 900 °C in a vacuum [Fig. 5(b)].³³² However, agglomeration occurs in Ir IDTs when exposed to a higher temperature of 1050 °C [Fig. 5(c)],³¹⁴ which is close to the Tammann temperature of Ir (1080 °C), defined as the onset temperature of volume diffusion in metals.³³³

Various electrode materials have been investigated for their performance at elevated temperatures. TiN has been employed as both the top and bottom electrodes in AlN piezoelectric micromachined ultrasonic transducers (PMUTs) fabricated on SiC substrate. However, the TiN electrode exhibits discoloration following annealing and testing up to 500 °C in an air environment, as shown in Fig. 5(d). This discoloration is attributed to the oxidation of TiN, resulting in the formation of TiO₂, or the creation of sub-stoichiometric TiNx.³³⁴ Another example involves the utilization of nickel (Ni) as the interdigital transducers (IDTs) in GaN SAW devices due to its ability to maintain Schottky barrier properties at high temperatures and its favorable acoustic matching with GaN. Ni-based IDTs have been tested over a wide temperature range (−196 °C to 500 °C),³³⁵ revealing an increase in insertion loss with temperature and the absence of a distinct resonance peak at 500 °C [Fig. 5(e)]. The Schottky barrier height

diminishes at higher temperatures, and the Ni metal exhibits the presence of porous holes. The degradation of the Ni/GaN contact can be attributed to the diffusion of nitrogen (N₂) from GaN, Ni diffusion into GaN, and the formation of nickel nitrides and gallides at elevated temperatures.

VIII. TCF OF Si MEMS

Si is a key material in the field of MEMS, enabling the integration of miniaturized mechanical and electrical components on a single chip.³³⁶ The unique combination of Si's mechanical properties, including high strength, low density, and excellent elasticity, along with its well-established fabrication processes, has made it the material of choice for a wide range of MEMS devices.³³⁷ Si MEMS devices exhibit remarkable sensitivity, precision, and reliability, offering a multitude of applications in areas such as sensing, actuation, and biomedical systems.³³⁸ The ability to fabricate intricate structures and integrate them with electronic circuits has opened up new possibilities for developing compact, lightweight, and low-power devices with enhanced performance.³³⁹ Si MEMS technology has significantly impacted various fields, including automotive, aerospace, healthcare, and consumer electronics, driving advancements in sensing, imaging, communication, and automation.³⁴⁰ The continuous development and innovation in Si MEMS hold great promise for the realization of next-generation devices with improved functionality and increased integration. This section will specifically focus on the temperature coefficient of resonance frequency of Si-based MEMS resonators.

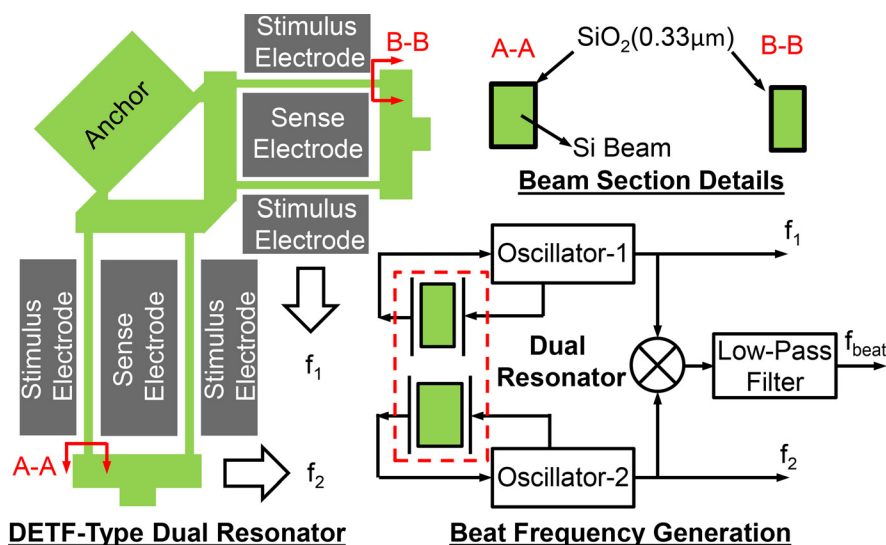


FIG. 6. Schematic of a thermally coupled double-ended tuning fork (DETF) dual-resonator and beat frequency generation technique (Jha et al., Transducers (2007). Copyright 2007 IEEE, Creative Commons).³⁴³

29 June 2025 22:04:31

A. Si MEMS for temperature sensing

A resonant MEMS device with a high TCf is a promising solution for on-chip temperature sensing due to its small sensing element, which enables a direct and rapid response of the resonance frequency to temperature variations. Si MEMS resonators typically exhibit an intrinsic TCf of approximately $-31 \text{ ppm}/^\circ\text{C}$ without compensation.³⁴¹ However, by incorporating a strain-amplifying beam on one end, the TCf of a double-ended-tuning-fork (DETF) resonator, fabricated on a glass substrate, can be increased by a factor of 33 compared to a one-end free DETF resonator. This enhancement is achieved by the differential thermal expansion between the structural layer and substrate, resulting in compression or stretching of the resonator tines and leading to significant frequency shifts with temperature changes. This approach enables a substantial TCf of $604 \text{ ppm}/^\circ\text{C}$, making it suitable for various high-sensitivity temperature sensing applications.³⁴² Additionally, a dual-resonator based on a Si/SiO₂ structure can generate a beat frequency by combining the two resonance frequencies, as shown in Fig. 6. The beat frequency exhibits a linear decrease with temperature ranging from -40°C to 120°C , with a large TCf of $-570 \text{ ppm}/^\circ\text{C}$. This beat frequency thermometer offers an estimated

resolution of approximately 0.008°C .³⁴³ Notably, the beat frequency technique effectively suppresses thermal lag between the external temperature sensor and the resonator, as there is no physical separation between the thermometer and the resonator. Consequently, the observed hysteresis in the frequency–temperature characteristic during rapid temperature cycling using an external temperature sensor can be mitigated by employing the beat frequency as a temperature sensor. Until recently, frequency comb sensing strategy has been demonstrated as a promising approach for ultrasensitive sensing applications. The internal resonating beam resonator demonstrates an exceptional TCf up to $-11\,481 \text{ ppm}/^\circ\text{C}$ based on the comb spacing modulation, which is a $59.2\times$ enhancement compared to a typical sensing scheme in a reference beam resonator.³⁴⁴ This is the largest TCf value reported in Si MEMS resonator to date.

B. Temperature compensation of Si MEMS

1. Passive methods

a. *Temperature compensation with SiO₂.* One common method of compensating for the TCf of Si MEMS resonators is by adding a SiO₂

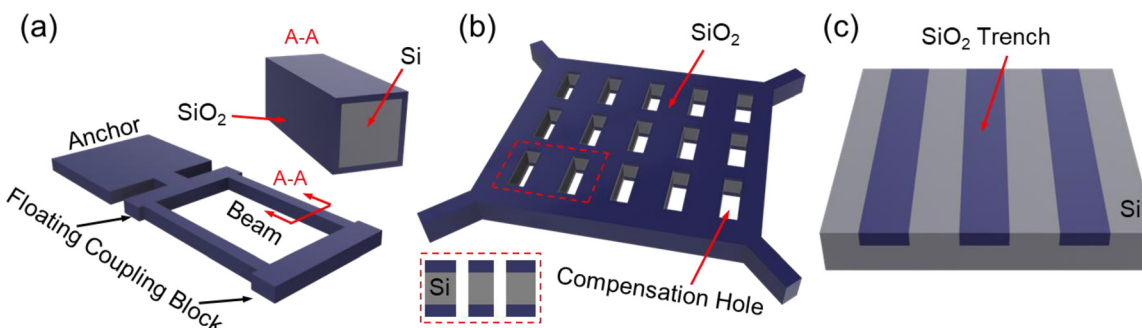


FIG. 7. Temperature compensation with SiO₂. (a) Schematic of Si-SiO₂ composite resonator. (b) The introduction of compensation holes in Si-SiO₂ MEMS resonator. (c) Schematic of oxide-filled trenches or islands for temperature compensation.

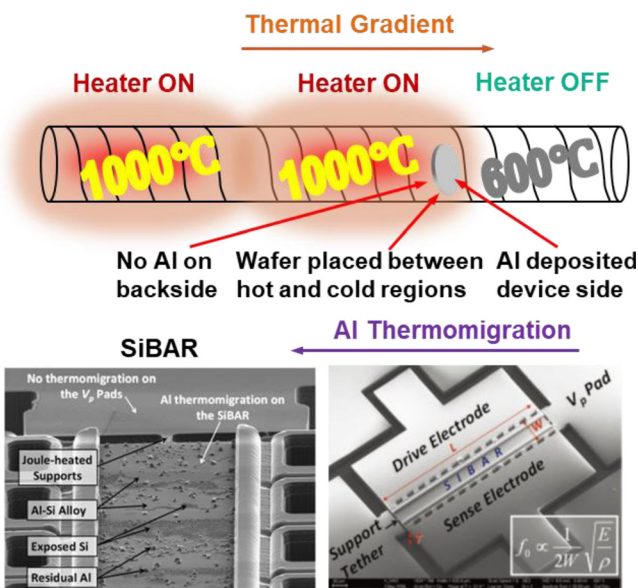


FIG. 8. Schematic of the wafer-level aluminum thermomigration process in a SiBAR. SEM images show a close-up of a SiBAR (bottom right) and an aluminum thermomigrated SiBAR (bottom left). (Hajjam *et al.*, *J. Microelectromech. Syst.* **59**, 87 (2012). Copyright 2012 IEEE, Creative Commons).

layer with a positive TCE_Y . A SiO_2 compensated fundamental mode free-free beam resonator achieves a reduction of TCf from -16.8 to $-0.4 \text{ ppm}^\circ\text{C}$ and the 15th overtone designs reduces TCf to less than $-0.1 \text{ ppm}^\circ\text{C}$.^{345,346} Research shows that the TCf of Si- SiO_2 composite resonators with two parallel beams coupled by two blocks on both ends [Fig. 7(a)] becomes more positive as the beam width becomes thinner. This correlation indicates that a larger relative thickness of

SiO_2 leads to a more positive TCf .³⁴⁷ Fluorine-doped SiO_2 , with a larger positive TCE_Y than pure SiO_2 , allows for tuning of the TCE_Y by controlling the concentration of fluorine. Fluorine doping is also an effective approach for avoiding an excessively thick oxide layer.³⁴⁸ The finite element method (FEM) analysis has demonstrated that the introduction of compensation holes in Si- SiO_2 MEMS resonators allows for reduced SiO_2 thickness while maintaining adequate compensation [Fig. 7(b)]. By utilizing compensation holes, a small TCf of $3.3 \text{ ppm}^\circ\text{C}$ has been achieved.³⁴⁹ The utilization of oxide-refilled trenches or islands [Fig. 7(c)], leveraging the advantageous low thermal conductivity of SiO_2 ($1.3 \text{ W m}^{-1} \text{ K}^{-1}$), presents a compelling opportunity for the fabrication of thermal isolation structures. These structures hold great promise in mitigating power consumption associated with ovenization compensation.³⁵⁰

b. Temperature compensation by doping. Temperature compensation effect is impacted by the vibration mode, crystal orientation, doping type (n- or p-type), and doping level. The elastic constants of semiconductors are impacted by doping through two primary mechanisms: the first mechanism is due to the dissimilarity between the doping atom and the host lattice, while the second mechanism is the introduction of free charge carriers through doping.³⁵¹ Degenerate boron-doping, a p-type doping, has been demonstrated to effectively reduce the TCf of Si MEMS resonators. For instance, the TCf of SiBAR devices, as shown in Fig. 8, has been reduced from -29 to $-18.9 \text{ ppm}^\circ\text{C}$ on $10\text{-}\mu\text{m}$ thick devices using degenerate boron doping. Additionally, boron-assisted aluminum thermos migration proves even more effective in reducing TCf , achieving a small TCf of $-2.72 \text{ ppm}^\circ\text{C}$ with 500 \AA of aluminum at 120 mA for 10 min .^{316,352}

A combination of n-type degenerate doping and adjustment of the operating bias current has been reported as an effective method for fine-tuning the TCf . In thermally actuated single-crystalline Si resonators, a low TCf of $0.005 \text{ ppm}^\circ\text{C}$ has been demonstrated. Higher

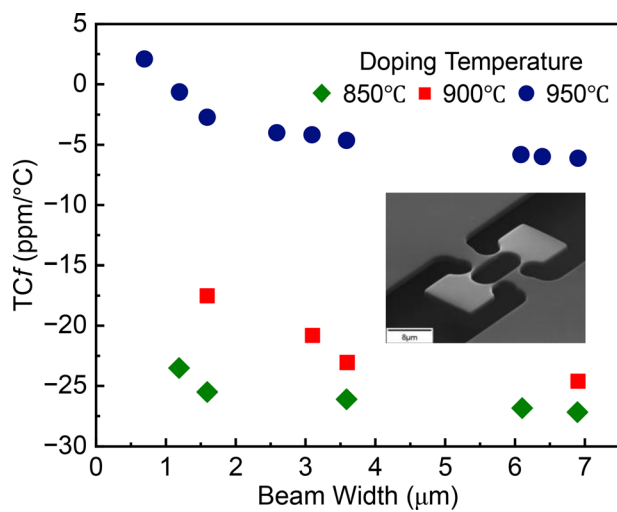


FIG. 9. Measured TCf values for different highly phosphorous doped I-shaped bulk acoustic resonators (IBARs) doped at different temperatures and with different actuator beam widths (Hajjam *et al.*, *J. Microelectromech. Syst.* **21**, 3 (2012). Copyright 2012 IEEE, Creative Commons).

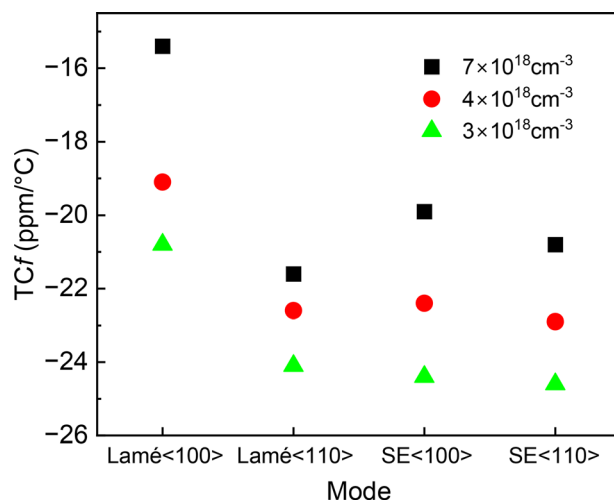


FIG. 10. Measured TCf of single crystal Si square-plate micromechanical resonators, aligned to different crystal orientations, vibrating in square extensional (SE) mode and Lamé mode, as temperature changes. The phosphorous doped concentration for the resonators is 3×10^{18} , 4×10^{18} , and $7 \times 10^{18}/\text{cm}^3$, respectively.

doping temperatures result in higher dopant concentrations, leading to less negative (or more positive) TC_f values. Narrower actuator beams show less negative TC_f compared to wider ones, as shown in Fig. 9. Additionally, higher bias currents are associated with less negative TC_f .^{317,318} Another study showcases a self-sustained Si MEMS oscillator operating at 2.4 MHz, which achieves a low TC_f of 0.4 ppm/ $^{\circ}\text{C}$ through high-concentration phosphorus doping. Optimizing the doping level and bias current enables superior temperature stability, potentially resulting in zero TC_f single-device MEMS frequency references.³⁵³

A theoretical study utilizing finite element method (FEM) parametric modeling and free carrier theory suggests that temperature compensation with n-doping applies to various resonance modes, including bulk modes like width/length extensional modes of a beam, Lamé/square extensional modes of a plate resonator, as well as flexural and torsional resonance modes.³⁵⁴ For square plate Si MEMS resonators, a standard doping level below $5 \times 10^{18} \text{ cm}^{-3}$ results in TC_f ranging from -32 to -29 ppm/ $^{\circ}\text{C}$ for both the Lamé mode and the square extensional mode, indicating insufficient compensation. Heavy n-type doping ($5 \times 10^{19} \text{ cm}^{-3}$) reduces the TC_f of the square extensional mode from -32 to -1 ppm/ $^{\circ}\text{C}$, while the Lamé mode exhibits an over-compensated TC_f of +18 ppm/ $^{\circ}\text{C}$. Heavy p-type doping effectively reduces the Lamé mode's TC_f to -2 ppm/ $^{\circ}\text{C}$. These observations align with the fact that n-type doping mainly affects the shear elastic constant $1/2(c_{11}-c_{12})$, whereas p-type doping significantly alters the elastic constant c_{44} .³⁵¹ Keyes' theory demonstrates that n-type doping has the largest effect on the slow shear mode of the elastic constants as a function of temperature. Temperature-stable wave propagation directions are only achieved with doping levels above 10^{19} cm^{-3} , which is consistent with experimental findings.³⁵⁵

A study investigating crystal orientation and vibration mode on the TC_f in n-type doped Si contour mode resonators (CMRs) found that the square extensional (SE) mode has a similar TC_f in both $\langle 100 \rangle$ and $\langle 110 \rangle$ orientations, despite different doping levels (up to $7 \times 10^{18}/\text{cm}^3$). This is because the SE mode is primarily influenced by the biaxial Young's modulus, which remains constant in both orientations. However, the TC_f of the Lamé mode is more sensitive to n-type doping when aligned to $\langle 100 \rangle$, whereas it remains nearly unchanged when aligned to the $\langle 110 \rangle$ axis. In the $\langle 100 \rangle$ orientation, the resonance frequency of the Lamé mode is affected by both c_{11} and c_{12} , which are significantly impacted by doping. These effects are summarized in Fig. 10. Moderate n-doping ($\sim 10^{18}/\text{cm}^3$) can effectively compensate for TC_f (-24.9 to -15.4 ppm/ $^{\circ}\text{C}$), and even small variations in doping concentration can have a notable impact on the TC_f for the Lamé $\langle 100 \rangle$ device. In contrast, the resonance frequency of the Lamé mode in $\langle 110 \rangle$ orientation is solely determined by c_{44} , and doping has no theoretical contribution to it.^{356,357}

Furthermore, it has been observed that the TC_f in the Lamé mode remains unaffected by variations in doping concentration within the range of $10^{18}/\text{cm}^3$, exhibiting quasi-linear temperature–frequency profiles. However, in a separate square-plate resonator, heavy doping ($5 \times 10^{19}/\text{cm}^3$) has been found to alter the polynomial order of the linear relationship between temperature and frequency, shifting the local turnover point.³¹⁶ In the case of double-ended tuning fork (DETF) resonators, a near-zero TC_f can be achieved by diffusing dopants through exposed sidewalls in a specific crystal orientation alignment, i.e., in the $\langle 100 \rangle$ orientation and 30° with respect to $\langle 110 \rangle$ orientation, as shown

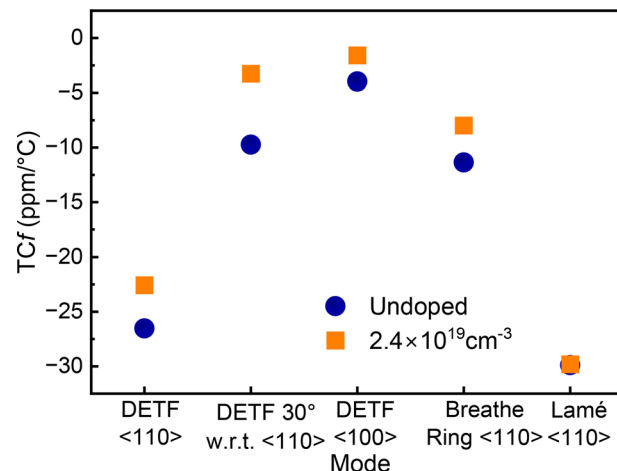


FIG. 11. Phosphorous doping effects on the TC_f of Si DETF aligned to different directions, dual breathe-mode ring resonator aligned with $\langle 110 \rangle$ direction, and Lamé-mode resonator aligned with $\langle 110 \rangle$ direction.

in Fig. 11. Interestingly, it has been discovered that the TC_f of Lamé-mode bulk resonators remains unaffected by lateral diffusion. Consequently, it becomes feasible to independently control the TC_f of neighboring resonant systems on the same wafer through geometry modification.³⁵⁸

TC_f compensation can also be accomplished through charge carrier depletion, following a similar principle of mitigating the impact of charge carrier flow during acoustic transduction, as achieved by generating a charge surplus through degenerate doping. The TC_f of the SiBAR can be reduced from -32 to -3 ppm/ $^{\circ}\text{C}$ by utilizing multiple p–n junctions to deplete the charge carriers. Multiple p–n junctions are formed by successively doping with alternating doping polarities, thereby increasing the number of depletion regions to attain enhanced levels of charge depletion. It has been observed that the concave SiBAR

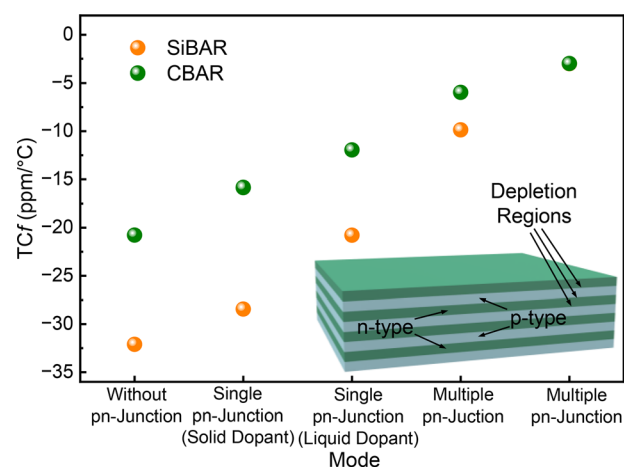


FIG. 12. Comparison of the TC_f between a SiBAR and concave SiBAR (or CBAR) on a highly resistive Si substrate, achieved through charge carrier depletion.

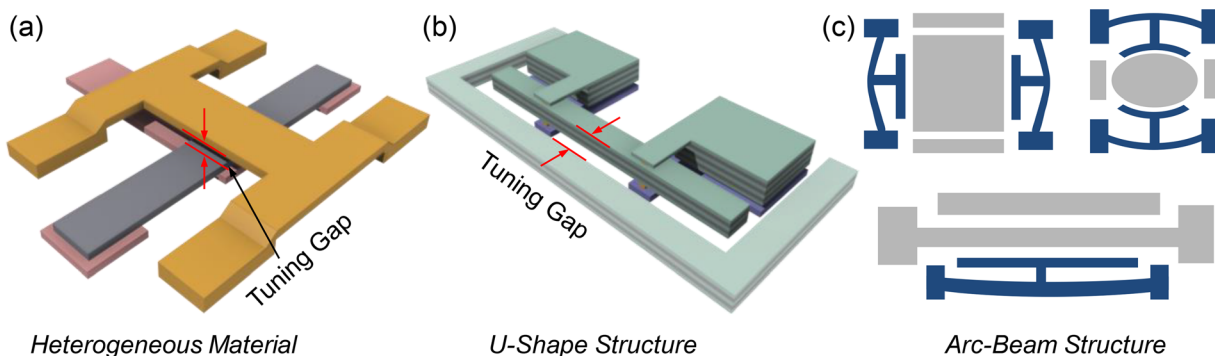


FIG. 13. Comparison of stiffness compensation techniques using (a) heterogeneous material, (b) U-shaped structure, and (c) arc-beam structure.

(featuring curved long edges) experiences additional shear strain in the xy -plane during acoustic transduction, which minimizes charge flow and compensates for the TC_f . However, these effects become less pronounced at extremely high depletion levels.^{359,360} At very high depletion levels with multiple p-n junctions, both the SiBAR and the concave SiBAR exhibit nearly identical TC_f values, suggesting that the TC_f is independent of the geometry of Si MEMS resonators in this case, as shown in Fig. 12. Liquid phosphorous dopants exhibit a greater efficacy in generating a depletion region within an equivalent annealing period in comparison to their solid dopant counterparts.

c. *Temperature compensation by stiffness tuning.* Stiffness compensation is an effective passive technique used to counteract the inherent negative TC_f in structural materials by introducing an electrical stiffness with a positive temperature coefficient. One unique advantage of stiffness frequency pulling is that it can retain the original resonator material and structure. Figure 13 illustrates three previously demonstrated electrical stiffness compensation methods.

The first method involves the introduction of a metal electrode positioned at a specific distance above the polysilicon doubly clamped beam resonator to achieve temperature compensation, as shown in Fig. 13(a). The material used for the support blocks of the top electrode is carefully selected to possess a larger CTE compared to the structural material of the mechanical resonator and its anchors. As the temperature rises, the resulting expansions cause the lower side of the top electrode to move vertically upwards at a faster rate than the top of the resonator beam. Consequently, there is a noticeable increase in the gap spacing between the top electrode and the resonator. This increase in the gap spacing brings about a reduction in the electrical spring constant between the top electrode and the resonator, thereby leading to a corresponding rise in the resonance frequency. This adjustment effectively counteracts the frequency decrease primarily induced by the temperature dependence of Young's modulus. By employing the temperature-dependent electrical stiffness technique, a polysilicon MEMS resonator has demonstrated a small TC_f of approximately $-0.24 \text{ ppm}/^\circ\text{C}$, effectively compensating for frequency shifts caused by temperature variations. This technique significantly reduces the total frequency drift from 1280 ppm in an uncompensated device to just 18 ppm over the temperature range of 300–380 K.³⁶¹

In the second method, the stiffness compensation is achieved by using a U-shaped suspended structure [Fig. 13(b)]. Leveraging this

structure, a free-free beam CMOS-MEMS resonator operating at 2.92 MHz achieves a near-zero TC_f of $0.43 \text{ ppm}/^\circ\text{C}$ in the temperature range of 0°C – 85°C , in stark contrast to the TC_f of $-69.78 \text{ ppm}/^\circ\text{C}$ measured in an uncompensated device.³⁶² A vertical stepped doubly clamped Al beam resonator yields linear compensation that reduces the TC_f from an uncompensated -374.5 to $-1.45 \text{ ppm}/^\circ\text{C}$.³⁶³ Compared to the first overhanging electrode method, the U-shaped suspended structure appears more favorable as it eliminates the need for additional processes. However, it is most likely suitable only for the specific case of free-free beam resonators. Employing this technique on other resonator topologies, such as doubly clamped beams, would necessitate inevitable modifications to the U-shaped geometry. Furthermore, it would be impractical to implement this compensation scheme for bulk resonators, such as disk and Lamé-mode resonators.

As presented in Fig. 13(c), the third approach involves the utilization of arc-beam structures as tuning electrodes. By leveraging the thermal stress-induced temperature-dependent gap spacing of the arc-beam structure, a proportional electrical stiffness is attained, thereby achieving a resonance frequency that is insensitive to changes in temperature. Notably, the arc-beam structure demonstrates versatility and applicability across diverse resonator topologies. This method has been demonstrated in a clamped-clamped beam resonator, which effectively reduces the TC_f from -394.16 to $+14.18 \text{ ppm}/^\circ\text{C}$ in the range of 0°C – 90°C .³⁶⁴ A similar geometrically engineered strategy using a

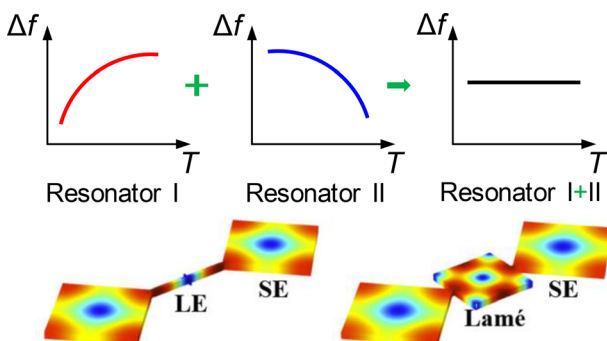


FIG. 14. TC_f manipulations by mechanical coupling of two resonators with different frequency temperature characteristics (Han *et al.*, *J. Microelectromech. Syst.* **32**, 271 (2023). Copyright 2023 IEEE, Creative Commons).

single-layer plate resonator with folded anchors significantly reduces the TC_f by two orders of magnitude compared to traditional straight beam designs.³⁶⁵

d. Geometric temperature compensation. Geometric temperature compensation of MEMS resonators employs tailored stress-compensation strategies to address the temperature-induced frequency variations arising from the thermal sensitivity of the material's Young's modulus. This technique was initially demonstrated on low-frequency (LF) nickel-plated folded-beam micromechanical resonators ($\sim 80 \text{ kHz}$), where a geometrically engineered stress-vs-temperature profile effectively counteracted the thermal dependence of Young's modulus. The approach achieved a substantial reduction in frequency excursion over a 27°C – 117°C temperature range, decreasing the TC_f from 2519 to 342 ppm/ $^\circ\text{C}$ and enabling the introduction of zero- TC_f points within the 27°C – 57°C range, which could be precisely tuned by design.³⁶⁶ Building on this foundation, a stress-tailoring mechanical support structure was later developed to extend the applicability of geometric stress-compensation techniques to higher-frequency (HF) flexural-mode beam resonators, suitable for practical reference oscillator applications. Using this advanced design, a 10-MHz micromechanical resonator demonstrated a remarkable frequency stability, with only a 200-ppm variation over a 27°C – 107°C temperature range. These advancements highlight the efficacy of geometric compensation in achieving enhanced thermal stability across diverse frequency regimes, paving the way for its integration into high-performance MEMS resonators.³⁶⁷

Gap-based temperature sensors provide an alternative approach for achieving precise temperature compensation in MEMS resonators. This method was demonstrated on an 80-MHz polysilicon micromechanical ring resonator, where the resonance frequency excursion over a 100°C temperature range was reduced from an uncompensated 1882 ppm to a compensated 11.3 ppm, representing an exceptional 166 times improvement.^{368,369} Unlike traditional methods that rely on material properties, this technique decouples temperature dependence from the Young's modulus-dominated behavior of the resonator by utilizing electrical stiffness changes arising from thermally induced

variations in the electrode-to-resonator gap spacing. By effectively harnessing thermal strain effects to adjust the electromechanical coupling, gap-based temperature sensors provide a powerful and scalable solution for minimizing frequency drift in high-frequency MEMS resonators.

e. Temperature compensation by other passive methods. Mechanical coupling of two resonators with different frequency–temperature characteristics can reduce the TC_f of the coupled resonator. It has been demonstrated that the TC_f of a Si square extensional mode resonator can be precisely controlled by employing mechanical coupling with either a narrow beam or a Lamé mode square plate, as shown in Fig. 14. By carefully adjusting the dimensions of the coupling element, it is possible to finely tune the TC_f and achieve a desired turnover point for the coupled resonator. Remarkably, a ± 10 ppm frequency change has been attained within the industrial temperature range of -40°C to 85°C .³⁷⁰ Another passive compensation has been achieved by nonlinear operation. Due to the correlation between amplitude and frequency fluctuations, a specific nonlinearity amplitude-frequency ($A\text{-}f$) dependence can reduce the effect of temperature variations on the frequency. It has been demonstrated in a Si MEMS resonator that the variation of frequency is reduced by a factor of 25 over a 75°C range by setting the oscillation amplitude at the optimum operating point.³⁷¹

2. Active methods

Active temperature compensation enables real-time adjustment of the resonant frequency to counter temperature variations across a wide range of temperatures. A dual resonator compensation technique utilizing thermal feedback achieves a simulated temperature stability of ± 0.74 ppm over a temperature range of -45°C to 85°C .³⁷² In the case of a micro-ovenized Si MEMS oscillator operating in shear Lamé mode at 77.7 MHz, temperature stability is improved by 180 times compared to uncompensated devices. The frequency drift is reduced from approximately 3000 to ± 0.25 ppm across temperature ranges from -25°C to 85°C . The micro-oven's measured heating efficiency is $0.48^\circ\text{C}/\text{mW}$, while the sustaining amplifier consumes 16 mA from a 3.2 V supply.³⁷³ Moreover, an oven-controlled Si MEMS oscillator operating at 20.2 MHz with a Q of 1.1×10^6 achieves a remarkable ± 1.5 ppb frequency offset over a 100°C temperature range with ovenization power below 10 mW, presenting an unprecedented combination of temperature stability and low power consumption in the timing industry.³²⁸ Figure 15 summarizes the comparison of performance metrics among ovenized Si MEMS resonators reported in the literature. The findings reveal the remarkable achievement of a near-zero TC_f alongside a low power consumption within the ovenized operation, consistently below 10 mW.

A combination of passive compensation, active compensation, and structure design strategies enables high-frequency stability across a wide temperature range. For a 20-MHz free-free beam MEMS resonator, a small TC_f of $+0.638$ ppm/ $^\circ\text{C}$ has been achieved over a temperature range of -50°C to 125°C . This result is accomplished through three compensation approaches: passive compensation using a structural gold layer, active compensation via a heater element, and a well-designed free-free beam structure that minimizes thermal mismatch between the vibrating structure and the substrate.³⁷⁴ In the case of a

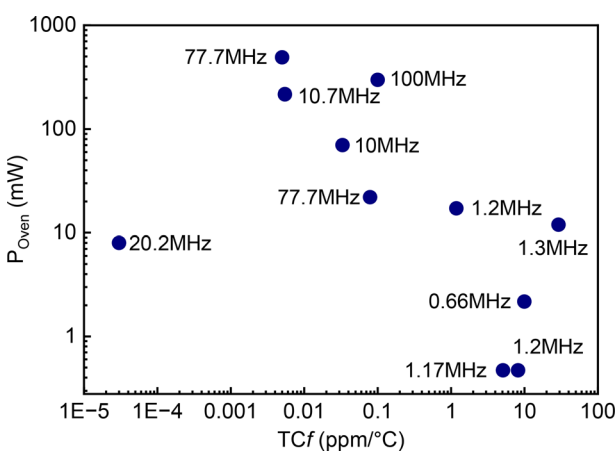


FIG. 15. Comparison of performance metrics among ovenized Si MEMS resonators reported in the literature: resonance frequency, TC_f , and power consumption.

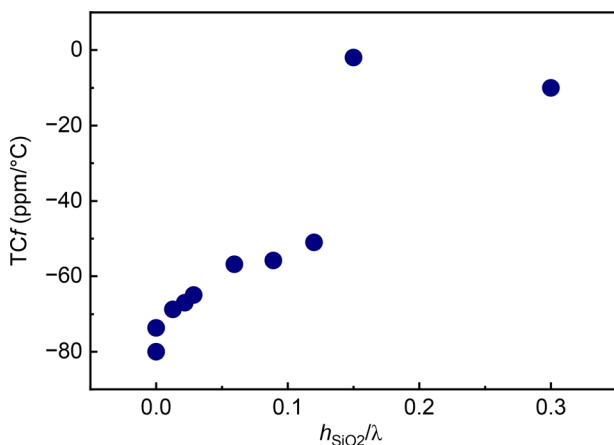


FIG. 16. TC_f variation of SiO₂/LiNbO₃ SAW devices with respect to h_{SiO_2}/λ ratio.

double-ended tuning fork (DETF) resonator, passive compensation is achieved by employing a precisely designed metal-oxide composite ratio, resulting in a TC_f of 8.2 ppm/°C. Utilizing the constant-resistance method, an ovenized resonator exhibits a TC_f of less than 1 ppm/°C while operating on low power consumption of 0.47 mW.^{375,376}

IX. TC_f OF LITHIUM-BASED OXIDES MEMS

Lithium-based oxides, such as lithium niobate (LiNbO₃) and lithium tantalate (LiTaO₃), are key materials in advanced electronic and optical devices. These ferroelectric crystals exhibit strong piezoelectric, pyroelectric, and electro-optic properties, making them ideal for use in MEMS, SAW devices, optical modulators, and frequency converters. Their stability and high performance enhance their application in sensors and communication systems. Ongoing research efforts are dedicated to exploring and optimizing the use of LiNbO₃ and LiTaO₃ in MEMS devices, with a focus on improving fabrication techniques and exploring innovative temperature compensation methods.^{377–380}

LiNbO₃ is a lead-free ferroelectric single crystal known for its robust and less temperature-dependent piezoelectric constant. Despite its advantageous properties as a ceramic material, patterning high-aspect-ratio structures in brittle thin-film LiNbO₃ have proven challenging, limiting its application in MEMS. Currently, most LiNbO₃ MEMS research has been focused on SAW resonators, with relatively fewer (but hopefully increasing) suspended LiNbO₃ MEMS (such as LWRs) being explored. LiNbO₃ demonstrates excellent SAW resonator frequency characteristics with low propagation loss and high electromechanical coupling factors. However, it suffers from poor temperature characteristics and exhibits significant TC_f values. For instance, the frequency shift of a LiNbO₃ SAW resonator shows a nearly linear relationship in the temperature range from 25 °C to 63 °C, with a TC_f of -87.5 ppm/°C.³⁰⁸ The TC_f of the longitudinal leaky X31°Y-LiTaO₃/X32°Y-quartz SAW is -26.2 ppm/°C.³⁸¹ A shear-horizontal leaky SAW resonator fabricated on X-cut LiNbO₃ demonstrates a TC_f of -65 ppm/°C across a temperature range from room temperature to 200 °C. The resonator remains operational when exposed to direct flame at 900 °C and exhibits robust power handling capabilities of up to 20 dBm.³⁸²

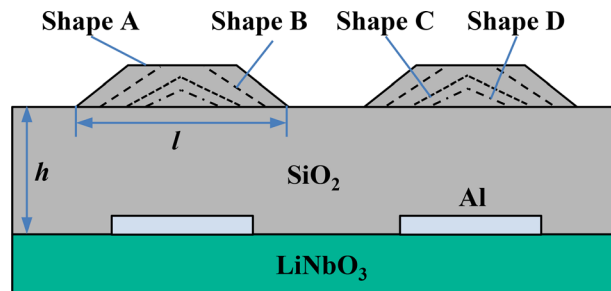


FIG. 17. Cross-sectional view of a shape-controlled SiO₂/Al/LiNbO₃ structure.

Lithium tantalate (LiTaO₃) is prized for its superior thermal stability and lower dielectric losses, making it more reliable in environments with varying temperatures. A low TC_f of -16.7 ppm/°C is achieved in an uncompensated thin-film LiTaO₃ LWR within the temperature range of 27 °C–97 °C, representing a 4.5-fold improvement over LiNbO₃ LWR.³⁸³ The thermal behavior of LiTaO₃ resonators is closely linked to crystallographic orientation. A zero TC_f (i.e., turnover temperature) is obtained in the temperature range of 50 °C–100 °C for X-cut LiTaO₃ LWRs with varying in-plane orientations relative to the Y-axis.³⁸⁴

A. Temperature compensation with SiO₂

The temperature stability of LiNbO₃ MEMS can be enhanced by utilizing SiO₂ thin films as a compensation layer. Figure 16 shows the TC_f variation of SiO₂/LiNbO₃ SAW devices with respect to h_{SiO_2}/λ ratio, where h_{SiO_2} represents the thickness of SiO₂ layer. In a 400-MHz Y-cut LiNbO₃ SAW with $h_{\text{SiO}_2}/\lambda = 0.15$, a TC_f of -2 ppm/°C has been achieved.³⁸⁵ However, a distinct result was observed in z-cut LiNbO₃ SAW, where a TC_f of -51 ppm/°C was measured in a SAW device on SiO₂/z-cut LiNbO₃ at $h_{\text{SiO}_2}/\lambda = 0.12$. This finding indicates that the deposited SiO₂ thin film may be more effective in enhancing the temperature stability of the SAW device on a z-cut LiNbO₃ substrate.³⁸⁶ Moreover, an improved TC_f of -10 ppm/°C was achieved in a SAW device based on a flattened SiO₂/Cu/YX-LiNbO₃ substrate, outperforming the TC_f of -80 ppm/°C measured in an Al/64°YX-LiNbO₃ SAW

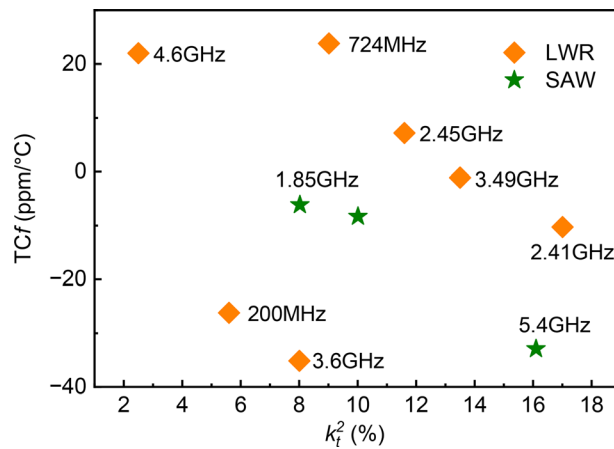


FIG. 18. Comparison of performance metrics among LiNbO₃ MEMS resonators.

device. The introduced SiO_2 film improves thermal stability without compromising frequency characteristics, while the high-density Cu contributes to obtaining a large reflection coefficient.^{387,388} These findings highlight the potential of SiO_2 thin films and Cu layers for enhancing the temperature stability of LiNbO_3 SAW devices.

The shape of the covered SiO_2 layer affects the performance of SAW devices. In the case of a SAW resonator implemented on a flat $\text{SiO}_2/\text{Al}/\text{LiNbO}_3$ structure, achieving a high k_t^2 value while suppressing bulk wave radiation is challenging due to the absence of a waveguide structure, such as a grating, that can reduce the wave velocity. Nevertheless, recent findings have shown that a non-flat $\text{SiO}_2/\text{Al}/\text{LiNbO}_3$ structure can effectively enhance k_t^2 while minimizing unwanted spurious responses and bulk wave radiation.³⁸⁹ Through the application of SiO_2 shape control techniques, an experimental demonstration of a high-performance $\text{SiO}_2/\text{Al}/\text{LiNbO}_3$ SAW resonator has been achieved, exhibiting a moderate k_t^2 value (8%) and nearly zero TC_f , with complete suppression of Rayleigh-mode spurious responses.³⁹⁰ Figure 17 illustrates the cross-sectional profile of the SiO_2 top surface, highlighting the trapezoidal region's step height of 160 nm for both shape A and shape B. While spurious responses persist, their intensity diminishes noticeably. When the step height is reduced to 120 nm in shape C and further to 60 nm in shape D, the spurious response is largely suppressed. It is important to note that the absolute TC_f values are subject to the SiO_2 thickness and the trapezoidal region's step height. Specifically, a near-zero TC_f is achieved when the SiO_2 thickness measures 0.3λ for shape A and B, and 0.35λ for shape C and D.

Recently, progress in fabrication technology has enabled the realization of plate acoustic wave resonators^{391,392} and LWRs based on LiNbO_3 . To enhance performance characteristics, a LWR based on a bimorph structure comprising LiNbO_3 and SiO_2 is attractive, aiming to simultaneously maximize coupling efficiency and minimize the TC_f . By configuring the LiNbO_3 thickness to be half that of SiO_2 , the nodal point aligns with the bimorph interface, resulting in a half sinusoidal pattern in the displacement (or stress) distribution within LiNbO_3 . This configuration enables maximum overlap between the electric field and stress mode shape. Experimental evaluation of the proposed device, operating in the third-order antisymmetric mode (A_3), exhibits exceptional performance with an ultra-low TC_f of $-1.1 \text{ ppm}^\circ\text{C}$ within the temperature range of 25°C – 75°C , a high electromechanical coupling coefficient of 13.5%, and a favorable Q of 500 at 3.5 GHz.³⁹³ However, an acoustic resonator based on S_4 mode Lamb waves, implemented on a bimorph structure comprising LiNbO_3 and SiO_2 , presents significantly larger TC_f values. Specifically, the series resonance displays a negative TC_f of $-32.9 \text{ ppm}^\circ\text{C}$, while the parallel resonance exhibits a positive TC_f of $30.4 \text{ ppm}^\circ\text{C}$. These substantial TC_f values can be attributed to the occurrence of severe buckling and cracks in suspended devices due to the compressive stress within the SiO_2 layer.³⁹⁴ Figure 18 provides a comparison of performance metrics among LiNbO_3 MEMS resonators. Notably, a LiNbO_3 LWR operating at 3.49 GHz has achieved a remarkable near-zero TC_f , while concurrently exhibiting a commendable k_t^2 of 14%.

B. Temperature compensation with AlN

Temperature compensation using an AlN film on a LiNbO_3 substrate has proven effective in enhancing the temperature stability and SAW velocity. In the case of $\text{Y}-128^\circ \text{ LiNbO}_3$, a highly c -axis-oriented

AlN layer with a thickness of $3.1 \mu\text{m}$, deposited via RF magnetron sputtering, has successfully improved the TC_f of the SAW delay line oscillator from -76.32 to $-39.04 \text{ ppm}^\circ\text{C}$ over the temperature range of 15°C – 35°C .³⁹⁵ However, the introduction of AlN tends to decrease the electromechanical coupling coefficient. Studies have demonstrated that increasing the thickness of the AlN film leads to improvements in both SAW velocity and temperature stability, albeit at the expense of a reduced electromechanical coupling coefficient.^{396,397} For instance, in the case of the $\text{Al IDT/AlN/LiNbO}_3$ SAW structure, the absolute TC_f shows a significant decrease as the thickness of the AlN film increases. Specifically, the pure z -cut LiNbO_3 single crystal exhibits a TC_f of $-73 \text{ ppm}^\circ\text{C}$, while at $h_{\text{AlN}}/\lambda = 0.1$, the TC_f is reduced to $-51 \text{ ppm}^\circ\text{C}$.³⁹⁸ Furthermore, measurements indicate a TC_f value of $-55.9 \text{ ppm}^\circ\text{C}$ for a SAW device based on c -axis AlN films on z -cut LiNbO_3 substrates at $h_{\text{AlN}}/\lambda = 0.11$. It is worth noting that both the phase velocity and insertion loss increase with the increment of h_{AlN}/λ from 0 to 0.11.³⁹⁹ TC_f of $\text{Y}-128^\circ \text{ LiNbO}_3$ LWRs is finely tuned using a temperature compensation layer (SiO_2) in combination with a thermally conductive layer (AlN). The AlN layer, with its higher sound speed, enhances both electromechanical coupling and thermal conductivity. By optimizing the thickness ratio of the $\text{AlN/LiNbO}_3/\text{SiO}_2$ structure, a small TC_f of $-5.2 \text{ ppm}^\circ\text{C}$ is achieved for the fourth-order symmetrical Lamb mode (S_4) operating at 8 GHz.⁴⁰⁰

X. TC_f OF SiC MEMS

Silicon carbide (SiC) is a crucial material for high-temperature applications in aerospace and energy, thanks to its exceptional thermal, mechanical, and chemical properties. It maintains stability in the presence of oxygen up to 1600°C by forming a protective SiO_2 passivation layer at around 1200°C . SiC possesses excellent thermal shock resistance, high thermal conductivity, chemical stability, low thermal expansion, and high-temperature strength retention, making it ideal for harsh environment applications. SiC MEMS devices are highly attractive for harsh environments, including gas turbines, high-temperature sensors, and harsh environment electronics. Compared to Si, SiC offers a larger bandgap (2.3–3.4 eV), higher breakdown field (3 MV/cm), and high saturation velocity ($2 \times 10^7 \text{ cm/s}$), making it suitable for high-power and high-frequency electronic devices. Thin-film 3C-SiC is commonly used due to its cost-effectiveness, compatibility with batch manufacturing processes, and wafer-scale hetero-epitaxial growth or deposition on various substrates.^{401–404}

The majority of SiC MEMS research focuses on versatile cantilever structures used to study elastic properties and temperature-induced changes in resonance behavior, such as TCE_Y and CTE. In 1995, one of the initial determinations of the TCE_Y of 3C-SiC was conducted. SiC cantilevers consist of a 10- μm -thick 3C-SiC film grown hetero-epitaxially on Si by CVD.⁴⁰⁵ These cantilevers are driven to resonance by an alternating electrostatic force, and vibration is detected using a frequency modulation technique. The measured TCE_Y is $-46 \text{ ppm}^\circ\text{C}$ in the range between room temperature and 450°C . Additionally, the TCE_Y of 3C-SiC has been experimentally determined by measuring the fundamental mode resonance frequency of micro-cantilever beams in the low-temperature range of -53 to 17°C . The TC_f of SiC cantilevers is $-18 \text{ ppm}^\circ\text{C}$, resulting in a TCE_Y value of $-39.8 \text{ ppm}^\circ\text{C}$.³⁰⁵ Moreover, a temperature-dependent resonance frequency measurement for polycrystalline 3C-SiC cantilevers yields a TC_f of $-25 \text{ ppm}^\circ\text{C}$, and the TCE_Y is found to be $-53 \pm 2 \text{ ppm}^\circ\text{C}$ in the range from room temperature to approximately 300°C .³¹¹

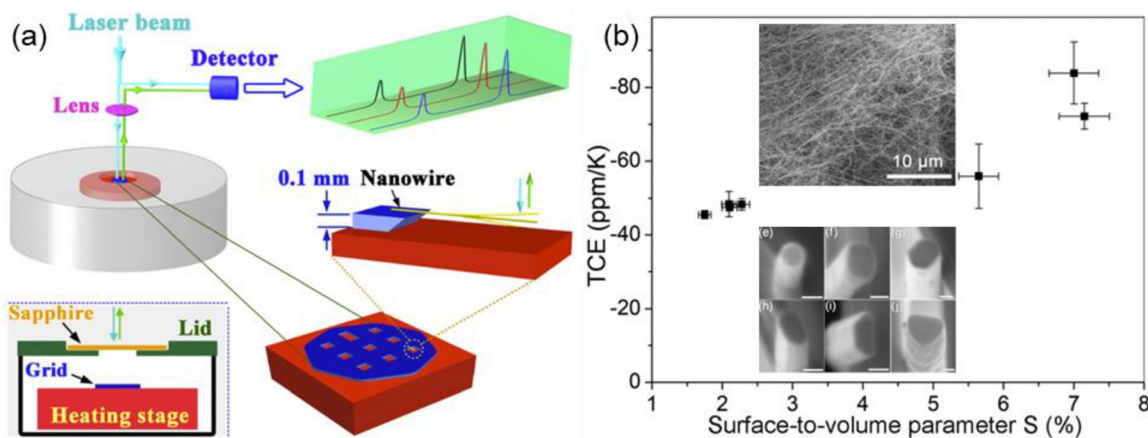


FIG. 19. (a) Schematic illustration of the laser Doppler vibrometer (LDV) setup for modulus testing of nanowires at elevated temperatures. (b) The dependences of TCE_Y on surface-to-volume parameter S. The inset shows an SEM image of the Fe-catalyzed SiC nanowires and cross-sectional profiles of the nanowire (Han *et al.*, Appl. Phys. Lett. 118, 043113 (2021). Copyright AIP Publishing, Creative Commons).

The size- and temperature-dependent E_Y of SiC nanowires in the temperature range of 27°C–302°C has been measured by laser Doppler vibrometer. A TCf of -34.5 ppm/°C is obtained from a 21-μm-long nanowire that has a corner-rounded triangular cross section with a width of 88 nm, which yields a TCE_Y of -72.2 ppm/°C. TCE_Y increases from -47.4 ppm/°C (the bulk value) to -78.1 ppm/°C, when the surface-to-volume parameter S (defined by $S = C \cdot t / A$, where C is the average perimeter of nanowire's cross section, t is the surface thickness, and A is the cross-sectional area) increased from 0.02 to 0.07. These results are summarized in Fig. 19. Such size and temperature dependency of E_Y would greatly benefit the design and fabrication of SiC-nanowire-based high-performance M/NEMS.⁴⁰⁶ Table III summarizes TCE_Y of 3C-SiC materials.

The latest development in coupling AlN and SiC presents exciting opportunities for creating MEMS capable of operating in high-temperature environments. This innovation combines the high-temperature-durable piezoelectricity of AlN with the commercial availability of SiC wafers and advanced micromachining techniques. A lateral overtone bulk acoustic resonator (LOBAR) consisting of an AlN transducer coupled to a suspended 1 μm SiC film, operating at 2.93 GHz with a Q value exceeding¹⁰⁶ exhibits a TCf of -15 ppm/°C in the temperature range of 0°C–90°C.⁴¹⁰ Furthermore, a capacitive in-plane

Lamé mode resonator, based on a 65-μm-thick monocrystalline 4H-SiC, demonstrates a TCf of -12 ppm/°C across the temperature range of -45°C to 85°C.⁴¹¹ Table IV summarizes the TCf reported in SiC MEMS resonators.

XI. TCf OF AlN MEMS

Aluminum nitride (AlN) stands out as a highly promising piezoelectric material, boasting exceptional thermal conductivity and a high acoustic wave velocity.^{413–416} Consequently, it emerges as an ideal candidate for next-generation microsensors, resonators, and filters.⁴¹⁷ The ease of synthesizing AlN through crystal growth methods like molecular beam epitaxy, pulsed laser deposition, metal-organic chemical vapor deposition, and magnetron sputtering further enhances its appeal, as these techniques align with established CMOS processes.^{418,419} This compatibility underscores the potential for seamlessly integrating AlN MEMS into CMOS circuits at the chip level.^{420,421} Another noteworthy aspect is that AlN, being a non-ferroelectric material, is intrinsically poled and lacks a Curie point, enabling it to maintain its piezoelectric properties even at high temperatures, reaching up to 1150°C.^{422–424} Moreover, AlN thin films demonstrate exceptional stability, exhibiting no phase transitions when heated in a nitrogen atmosphere from room temperature up to its

TABLE III. TCE_Y of various 3C-SiC materials. LDV: laser Doppler vibrometer; t: thickness; d: diameter.

References	Material	Device	Dimension	Methods	Temperature (°C)	E_Y (GPa)	TCE _Y (ppm/°C)
405	[100] Films	Cantilever	$t = 10 \mu\text{m}$	LDV (resonance)	RT-260	694	-46
305	[111] Films	Cantilever	$t = 2.6 \mu\text{m}$	LDV (resonance)	-63-RT	453	-39.8 ± 5.99
311	Poly-films	Cantilever	$t = 2.7 \mu\text{m}$	LDV (resonance)	RT-300	330 ± 45	-53 ± 2
406	[111] Nanowire	Nanowire	$d = 55\text{--}200 \text{ nm}$	LDV (resonance)	RT-302	460–560	$-(47.4\text{--}78.1)$
407	[111] Nanowire	Nanowire	$d = 35\text{--}286 \text{ nm}$	In situ SEM vibration	327–1077	230–750	0
408	Poly-films	Freestanding thin-film dogbone	$t = 2.3\text{--}3.4 \mu\text{m}$	Strain measurement	RT-1000	366 ± 18	-84
409	Poly-films	Film	$t = 40 \mu\text{m}$	Raman scattering	RT-900	463 ± 2	-58.3

TABLE IV. Comparison of TCf data reported for SiC MEMS resonators.

References	Material	Resonator type	Electrode	Measurement scheme	Device dimension (μm)	Temperature ($^{\circ}\text{C}$)	f (MHz)	TCf (ppm/ $^{\circ}\text{C}$)
305	3C-SiC	Cantilever	NA	LDV	$L: 125 \mu\text{m}$ $W: 18 \mu\text{m}$ $t: 2.6 \mu\text{m}$	-73 to 17	Normalized	-18
311	3C-SiC on poly-Si bridges	Cantilever	NiCr Contact	LDV	$t: 2.7 \mu\text{m}$	RT-600	Normalized	-24.3 to -26.6
406	3C-SiC	Nanowire	NA	LDV	$L: 21 \mu\text{m}$	27-302	$f_1: 0.23$ $f_2: 1.43$	-34.7
403	4H-SiC	In-plane Lamé mode resonator	Al	Electrically driven & read out	$L: 900 \mu\text{m}$ $W: 900 \mu\text{m}$ $t: 65 \mu\text{m}$	-45 to 85	6.27	-12
412	6H-SiC	Microdisk	NA	Optical	$d: 10 \mu\text{m}$ $t: 1.2 \mu\text{m}$	-27 to 125	15.14	-52

melting point of 2200°C . These attributes position AlN as an attractive material for deployment in harsh environments.^{425,426} Extensive research has explored the growth of AlN on various substrates, including sapphire, SiC, Si, and LiNbO₃.^{427,428} This section will primarily focus on examining the impact of temperature on the resonance behavior of different AlN MEMS resonators.^{429,430}

A. TCf of AlN SAW

1. SAW on AlN/sapphire

AlN thin films grown on sapphire substrates have emerged as highly promising piezoelectric structures for high-temperature SAW applications, primarily due to their exceptional thermal and chemical stability even at temperatures surpassing 1000°C . Additionally, both the longitudinal wave velocity and the shear wave velocity of sapphire closely match those of AlN, at approximately 11 000 and 6000 m/s, respectively. This minimizes acoustic velocity dispersion.⁴³¹

Studies have indicated that the TCf of AlN SAW on sapphire is influenced by the ratio of AlN thickness (h_{AlN}) to wavelength (λ). The TCf of AlN/sapphire SAW devices with different h_{AlN}/λ ratios has been estimated across a temperature range of -30°C to 60°C . It exhibits an almost linear change from -30 ppm/ $^{\circ}\text{C}$ to -45 ppm/ $^{\circ}\text{C}$ as h_{AlN}/λ increases from 0.067 to 1.86. Notably, a compensation point, where the TCf is approximately 0.5 ppm/ $^{\circ}\text{C}$, is observed at $h_{\text{AlN}}/\lambda = 1.116$.⁴³² The reduced softening of elastic constants and smaller thermal expansion of AlN, compared to sapphire, explain such variation in TCf with AlN film thickness. The temperature-dependent elasticity is determined by an anharmonicity in the inter-atomic potentials, and AlN's elasticity exhibits weaker temperature dependence due to a smaller Gruneisen anharmonicity parameter.⁴³³ The thickness of MOCVD grown AlN films for SAW resonators is typically around $1 \mu\text{m}$. Therefore, the low-quality AlN seed layer exists between the AlN film and substrate may be one of the potential causes of the low Q of the AlN SAW. Q of the SAW on AlN/Sapphire has been improved from 1500 to 3500 by increasing the thickness of AlN from ~ 1 to $4 \mu\text{m}$ and by employing a larger aspect ratio of length to width (L/W) value of 12, which can reduce the negative impact of low-quality seed layer and reduce the IDT resistance, respectively.⁴³⁴

Crystal orientation plays a crucial role in determining the acoustic wave velocity, thereby exerting a considerable influence on the TCf. The TCf of AlN/sapphire SAW devices grown in two different orientations, namely, [11-20]AlN/[1-100]Al₂O₃ and [1-100]AlN/[11-20]Al₂O₃, was analyzed across a temperature range of 25°C - 185°C . It was observed that the TCf of the SAW device in the [1-100]AlN/[11-20]Al₂O₃ orientation was lower compared to the [11-20]AlN/[1-100]Al₂O₃ orientation, given a specific h_{AlN}/λ value. This indicates that the TCf is primarily influenced by the CTE in each direction, and the variation in SAW phase velocities between orientations leads to differences in TCf values.²¹⁷ These results are summarized in Fig. 20. Subsequent research has revealed that the TCf of AlN SAW devices on sapphire remains unaffected by the choice of mirror structures. Both devices exhibit comparable TCf values, approximately -45.7 ppm/ $^{\circ}\text{C}$ for the device featuring strip electrodes in the mirrors (SAW resonator) and -47.3 ppm/ $^{\circ}\text{C}$ for the device incorporating circular electrodes in the mirrors (SPC resonator).⁴³⁵ Compared to the one-port SAW

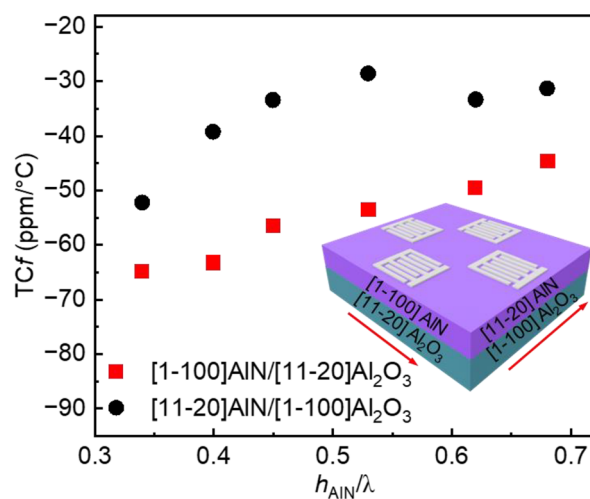


FIG. 20. Schematic of SAW in [11-20]AlN/[1-100]Al₂O₃ and [1-100]AlN/[11-20]Al₂O₃ orientations and TCf distributions with different h_{AlN}/λ .

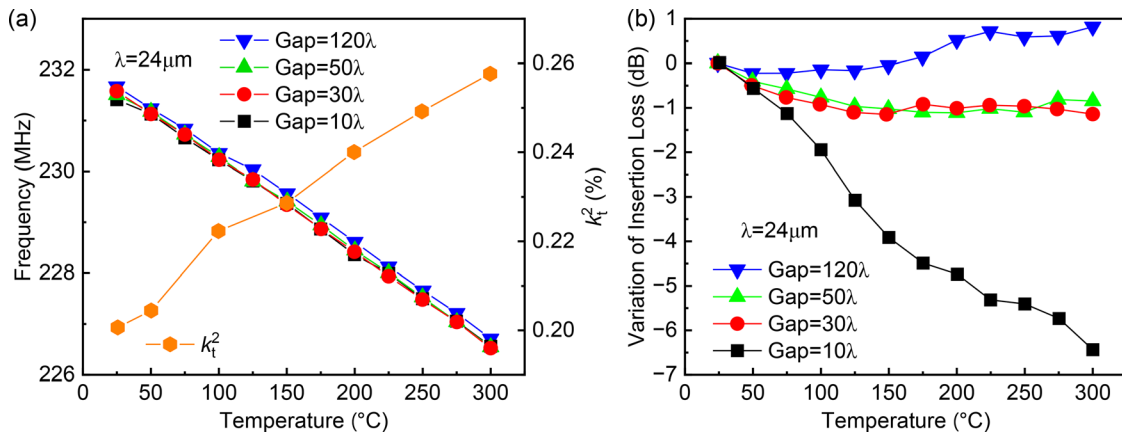


FIG. 21. (a) Frequency variation vs temperature for AlN SAW on sapphire with various free-space delays and evaluation of k_t^2 with temperature. (b) Insertion loss variation of AlN SAW on sapphire with various free-space delays.

resonator, the one-port SPC resonator features an additional resonance mode. The use of the frequency difference between the two resonance modes of the one-port SPC resonator enhances the temperature sensitivity, resulting in a large TCf of $-99.3 \text{ ppm}^\circ\text{C}$.

In addition to resonance frequency, temperature plays a significant role in influencing the characteristics of AlN SAW on sapphire, particularly k_t^2 and Q. For instance, a 2.45-GHz AlN/sapphire SAW resonator demonstrates a TCf of $-34 \text{ ppm}^\circ\text{C}$ within the temperature range spanning from room temperature to 500°C . Within this range, k_t^2 increases from 1.85% at room temperature to 2.25% at 500°C , while the Q value experiences a decrease in approximately 22%.⁴³⁶ The decrease in Q with increasing temperature can be attributed to the rise in internal losses within the resonator, primarily driven by temperature-dependent material properties and internal damping mechanisms. At elevated temperatures, the resonator material experiences greater internal damping due to viscoelastic loss and thermoelastic loss, leading to a reduction in Q. Additionally, temperature escalation can contribute to increased surface roughness and degradation of the resonator's surface. This, in turn, results in heightened energy loss due to scattering and surface-related dissipation, further contributing to a decrease in Q. Subsequent studies demonstrate that the AlN/sapphire structure is enhanced with temperature up to at least 300°C , with a 30% increase in the k_t^2 coefficient when the temperature increases from 25°C to 300°C . It is feasible to create SAW sensors with a constant insertion loss, high sensitivity, or even improve the signal quality by modulating the free-space delay gaps between input and output IDTs as the temperature changes, as shown in Fig. 21. This approach can counteract the expansion of k_t^2 due to the temperature-dependent increase in propagation losses if the delay line is sufficiently long. Notably, the TCf remains unaffected by the specific free-space delay under consideration.^{437,438} However, the absolute TCf value decreases from 81 to 66 ppm/ $^\circ\text{C}$ with an increasing normalized thickness of the AlN film (kh_{AlN}) from 0.17 to 2.24.^{437,438}

Studies have reported that a one-port quasi-synchronous AlN/sapphire-based SAW resonator maintains a high Q and remains stable through multiple heating cycles within the temperature range of 25°C – 400°C , preserving 50% of its initial room temperature value of 8000. However, when exposed to a temperature of 450°C , the Q

experiences a sharp decline to 2900 and cannot be restored due to ongoing oxidation of the aluminum electrode, which can negatively impact the morphology of the AlN layer and its electroacoustic properties. This continuous oxidation ultimately leads to the detuning of the

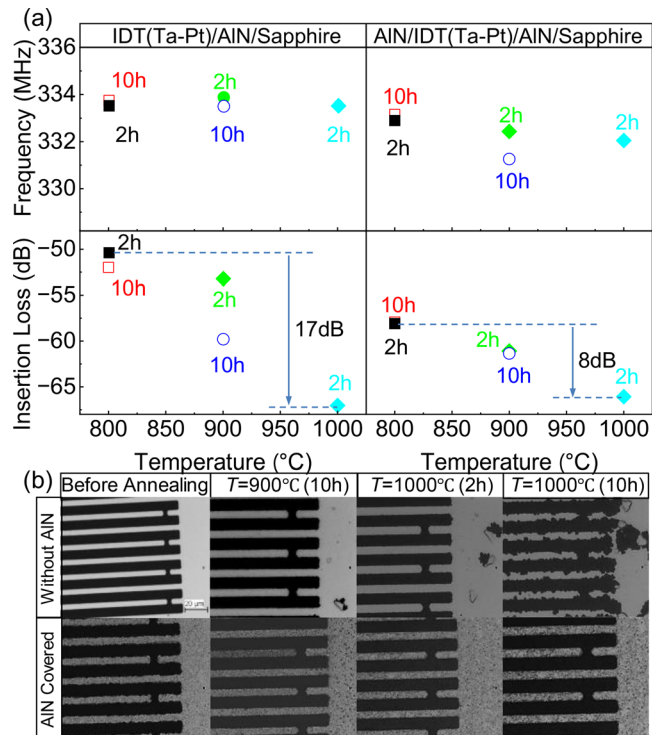


FIG. 22. (a) Evolution of frequency and insertion losses as a function of the temperature and time of annealing of IDT/AlN/sapphire and AlN/IDT/AlN/Sapphire heterostructures. (b) Optical microscopy image of the devices before annealing and after annealing at 900°C for 10 h, 1000°C for 2 h and 1000°C for 10 h. High temperature treatment leads to the discontinuities of the IDTs (Legrani et al., *IEEE International Ultrasonics Symposium* (2012). Copyright 2012 IEEE, Creative Commons).

resonators.⁴³⁹ Therefore, the sensitivity of AlN to oxidation is a major obstacle for high-temperature sensing applications.

To tackle this challenge, an additional 0.5- μm -thick protective AlN layer has been added on top of the IDT/AlN/sapphire SAW structure, aiming to enhance the lifetime of the active piezoelectric AlN film and shield the electrodes from agglomeration or chemical aggression at high temperatures. As expected, the Ta-Pt IDTs in the unprotected heterostructure are damaged after annealing at 900 °C for 10 h and completely destroyed after treatment at 1000 °C for 2 h. Conversely, no deterioration of IDTs is observed at high temperatures for the protected AlN/IDT/AlN/sapphire heterostructure. However, after prolonged exposure to high temperatures (1000 °C), the protective AlN films are fully oxidized, with only a small portion of AlN remaining as a columnar structure near the sapphire substrate, as shown in Fig. 22.²²¹ Nevertheless, for applications at temperatures exceeding 1000 °C, more resilient materials need to be explored as protective layers. The addition of the protective AlN layer results in increased insertion loss and a frequency decrease of 0.5 MHz, likely due to the lower quality of the protective layer. However, both structures exhibit a linear TC_f of approximately -80 ppm/°C within the temperature range of 25 °C–600 °C. While the unprotected IDT/AlN/sapphire structure demonstrates deteriorating insertion losses after annealing, the protected heterostructure shows less degradation.

It has been demonstrated that IDT(Pt/Ta)/AlN/sapphire SAW devices exhibit resilience to short-term exposure to annealing temperatures as high as 900 °C, as shown in Fig. 22.²²¹ The increase in insertion losses observed during annealing can be attributed to two main factors. First, the Pt IDT electrode undergoes degradation at high temperatures, leading to decreased conductivity as observed through scanning electron microscopy (SEM), which reveals recrystallization and agglomeration phenomena resulting in the formation of large crystallites and voids. Second, ellipsometry and secondary ion mass spectroscopy investigations confirm progressive surface oxidation of AlN at temperatures exceeding 700 °C. While the oxide layer thickness continues to slightly increase at 800 °C, the presence of initial minor oxidation hampers the diffusion of oxygen molecules through the oxide overlayer, thus passivating the AlN films from further aggression.⁴⁴⁰ It should be noted that the formation of an extremely thin Al₂O₃ film on the surface of AlN may degrade the performance of AlN/sapphire SAW devices at high temperatures around 900 °C. However, XRD and atomic force microscopy (AFM) results affirm the remarkable stability of AlN crystals under high temperatures up to 900 °C, as evidenced by the unmodified full width at half maximum (FWHM) of the (002) AlN rocking curve (RC) and minimal alteration of the AlN surface after annealing.³³¹

2. SAW on AlN/quartz

AlN/quartz SAW devices have gained popularity as a versatile platform. They offer several advantages over other SAW devices, including high frequency stability, low insertion loss, and high sensitivity. Moreover, these devices boast a wide working temperature range and excellent corrosion resistance. However, they also have some limitations, such as lower coupling coefficients and higher fabrication costs compared to other SAW devices. Despite these challenges, AlN/Quartz SAW devices remain highly promising for various applications, such as wireless communication, sensing, and timing devices. The SAW device that incorporated the AlN film on ST-X quartz substrates

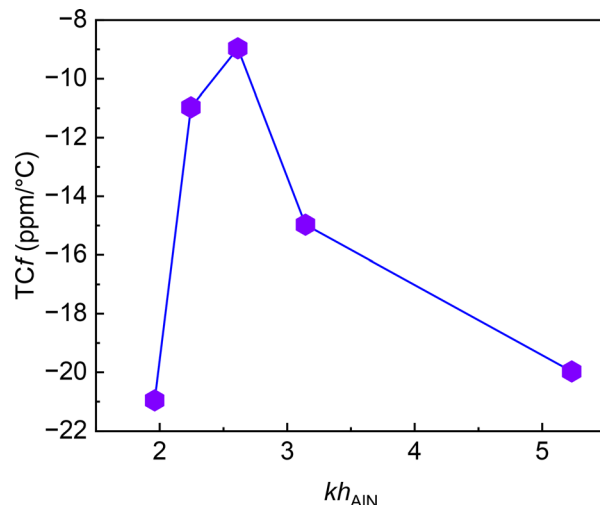


FIG. 23. Variation of the TC_f of the AlN/diamond structure vs the normalized thickness of AlN film.

demonstrated a slightly higher frequency (93.4 MHz) compared to the pure quartz substrate (90.4 MHz). This increase can be attributed to the naturally higher acoustic velocity or stiffness constants of the AlN film. Notably, the TC_f for the SAW device on the quartz substrate was measured to be 0, whereas it reached 16 ppm/°C for the AlN/ST-X quartz-based SAW device with $h_{\text{AlN}}/\lambda = 0.05$ in the temperature range of 0 °C–80 °C.⁴⁴¹ Compared to AlN/Si devices, AlN/quartz SAW device exhibited a higher phase velocity, a larger k_t^2 , and a smaller TC_f.⁴⁴²

3. SAW on AlN/diamond

Polycrystalline diamond has garnered significant interest in SAW device fabrication due to its remarkably high SAW velocity of approximately 12 000 m/s, making it the material with the highest elastic constant available. Despite lacking piezoelectric properties, diamond proves to be an ideal substrate for SAW devices when combined with piezoelectric thin films like ZnO or AlN. Researchers conducted a study on the TC_f and k_t^2 of SAW devices based on AlN/diamond layered structures with the goal of increasing the operating frequency to the X-band range (~8 GHz). Utilizing e-beam lithography, high lateral resolution IDTs were developed with varying spatial periodicities ranging from 1 to 3.2 μm . The TC_f measurements in the temperature range of 20 °C–100 °C revealed a nonlinear relationship with the normalized thickness kh_{AlN} (ranging from 2 to 5.4) where k represents the wave number ($k = 2\pi/\lambda$). Initially, the TC_f increased within the kh_{AlN} range of 2–3, displaying values between -21 and -9 ppm/°C. Subsequently, it gradually decreased from -9 to -20 ppm/°C as kh_{AlN} increased from 3 to 5.4.⁴⁴³ These results are shown in Fig. 23. It is worth noting that the TC_f is expected to increase with the kh_{AlN} value until it reaches zero since AlN and diamond exhibit opposite signs of TC_f. At the moment, the behavior of TC_f in AlN/diamond SAW devices remains unclear. To achieve a low TC_f, a 0.8- μm amorphous SiO₂ layer has been sputtered on top of the Al IDT/AlN/diamond structure. A low TC_f of 6.8 ppm/°C has been reported in the temperature range from -50 °C to 100 °C.⁴⁴⁴

4. SAW on AlN/metal

There is a growing demand for AlN SAW strain sensing in metal structural health monitoring, primarily due to its potential applications in wireless and passive measurements. Currently, these sensors are typically attached to metal with adhesives, which can cause measurement errors and detachment in high-temperature environments. To overcome these challenges, researchers directly sputtered AlN films onto TC4 alloy (also known as Ti-6Al-4V) substrates. The evaluation showed that as temperature increased from room temperature to 350 °C, the resonance frequency consistently decreased due to thermal expansion effects and degraded SAW velocity. Increasing the AlN layer thickness from 1.5 to 3 μm decreased the TC_f values from -89.4 to -66.2 ppm/°C. One possible explanation for this trend is that the effective CTE of the layered AlN/TC4 structure decreases as the thickness of AlN increases. Conversely, a greater number of acoustic waves propagate in the AlN films, causing the TC_f to approach that of standalone AlN films, which is approximately -30 ppm/°C. Additionally, the thickness of the AlN layer also impacts the k_t². Specifically, the device with a 2-μm AlN layer exhibits a larger k_t² across the entire temperature range, with an enhancement of approximately 30% from room temperature to 350 °C.⁴⁴⁵

5. SAW on AlN/LiNbO₃

AlN SAW resonators based on LiNbO₃ substrates are a promising platform for various applications due to their superior performance, low cost, and ease of integration with other electronic components. The SAW properties of c-axis-oriented AlN films deposited on z-cut LiNbO₃ substrates were investigated. A SAW device with a center frequency of 116.5 MHz, phase velocity of 4200 m/s, and k_t² of 1.5% was measured at room temperature. Although the k_t² was smaller than that of z-cut LiNbO₃ single crystal (4.5%),⁴⁴⁶ it was improved compared to SAWs with AlN films deposited on sapphire substrates (less than 0.8%). The resonance frequency decreased linearly with temperature in the range from 0 to 100 °C, and the TC_f was measured to be about -66 ppm/°C, which was smaller than that of the z-cut LiNbO₃ single crystal (-70.2 ppm/°C). In a separate study,³⁹⁸ it was discovered that the absolute TC_f of the AlN SAWs on LiNbO₃ substrate significantly decreased with an increase in the thickness of the AlN film, namely, a TC_f of -73 ppm/°C for the pure z-cut LiNbO₃ single crystal and a TC_f of -51 ppm/°C at h_{AlN}/λ = 0.1. Similar observations were made when studying the effects of the thickness of sputtered AlN on the TC_f of SAW based on AlN-on-LiNbO₃ substrate.⁴⁴⁷ In the temperature range of 15 °C–35 °C, as the AlN film thickness increased from 0 to 4.51 μm, the TC_f changed from -76.32 to -28.81 ppm/°C, resulting in a 62.25% improvement in the TC_f.

6. SAW on AlN/Si

Growing AlN on Si offers several advantages over other substrates such as sapphire, quartz, and diamond. A key benefit is the widespread availability and relatively low cost of Si wafers, making it an economically viable option for large-scale manufacturing. Moreover, the integration of AlN-based devices with existing Si-based electronics becomes possible, facilitating the development of highly integrated systems.^{448,449} The frequency-temperature performance of SAW resonator with a Pt/AlN/Pt/Si structure has been examined. Note that the

devices feature a floating bottom electrode composed of a 50-nm Pt layer, representing a short-circuit boundary condition at the AlN/Si interface. The floating bottom electrode design helps mitigate additional parasitic capacitances, leading to an increase in the parallel resonance frequency and enhanced k_t². A 16-MHz downshift in resonance frequency has been observed when increasing the temperature from 25 °C to 500 °C. This decrease was attributed to thermal expansion, resulting in enlarged finger size and spacing. Additionally, as the test temperature increased, the amplitude of the SAW signal decreased due to enhanced acoustic scattering and increased propagation loss.^{450,451} Reducing the digit and interdigit spacing width of the IDTs leads to an increase in the resonance frequency for SAW. TC_f values increase if the SAW has a higher frequency, which has been observed in SAW structures fabricated on different substrates: AlN/Si, AlN/glass, and GaN/Si.⁴⁵²

A new method for designing temperature-compensated AlN SAW devices was proposed,⁴⁵³ which involves incorporating trenches filled with oxide beneath the SAW wave and controlling their shape. FEM simulations demonstrate the potential to achieve a nearly zero TC_f. Subsequently, the effectiveness of an oxide trench array (OTA) as a passive temperature compensation structure for AlN-on-Si SAW MEMS resonators was experimentally validated across a temperature range of -60 °C to 300 °C.⁴¹⁷ The introduction of OTA resulted in a significant change in the first-order TC_f, reducing it from -24 to 6.66 ppm/°C at room temperature. Notably, a turnover point for the first-order TC_f was observed at 197 °C, highlighting the efficacy of OTA as an effective structure for passive temperature compensation.

7. SAW on AlN/SiC

MEMS resonators based on AlN grown on SiC substrates offer several advantages. The lower lattice mismatch between AlN and SiC results in reduced dislocation density and improved crystal quality, leading to higher Q and superior device performance. SiC's wide bandgap supports operation at high frequencies and elevated temperatures without thermal breakdown. The high thermal conductivity of SiC facilitates superior heat dissipation and enhanced high-temperature stability. Additionally, AlN on SiC exhibits a higher piezoelectric coefficient, resulting in increased electromechanical coupling and enhanced device sensitivity.

The impact of a 3C-SiC buffer layer on the SAW properties of AlN films grown on Si substrates has been investigated. While the SAW velocity and k_t² of the AlN/3C-SiC structure (v = 5020 m/s, k_t² = 0.79%) are slightly smaller compared to the AlN/Si structure (v = 5174 m/s, k_t² = 1.95%), the insertion loss is reduced by 1.97 dB. Moreover, the TC_f of the AlN/3C-SiC/SiO₂/Si sample is measured to be -18 ppm/°C within the temperature range of 30 °C–150 °C, exhibiting an improvement over the value of -30.8 ppm/°C for the AlN/Si structure. The enhanced TC_f and reduced insertion loss are attributed to the closely matched CTE and minimal lattice mismatch (1%) between AlN and 3C-SiC.⁴⁵⁴ Similar results have been obtained in a comparison study on the thermal stability of SAW devices based on AlN/Si (111) substrate and AlN/SiC (0001) substrate in the temperature range from room temperature to 350 °C. The choice of IDT metallization, whether Ti/Al or Pt/Ti/Au, did not significantly impact the TC_f. Furthermore, the TC_f variation for the first-order Rayleigh mode of the AlN/SiC (0001) SAW remained minimal (within 0.5 ppm/°C) when increasing the h_{AlN}/λ from 0.05 to 1.28.⁴⁵⁵

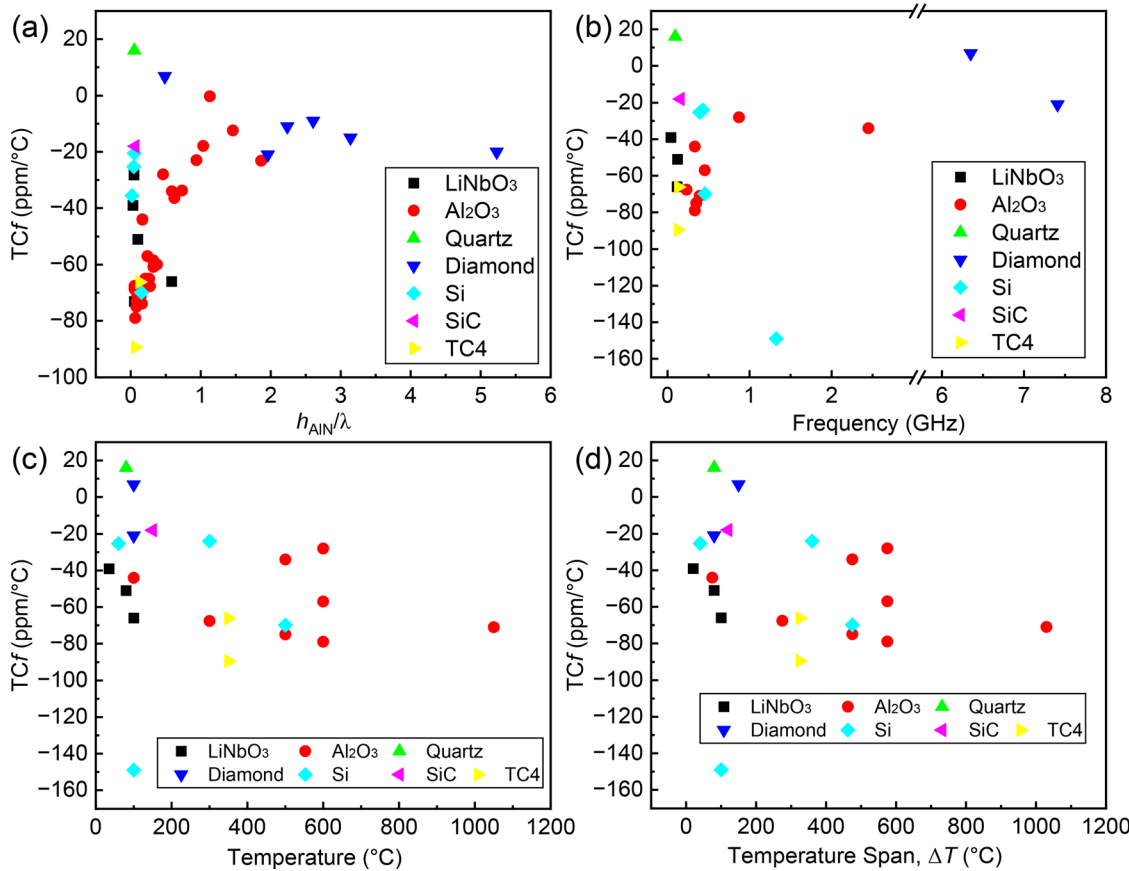


FIG. 24. Variation of the TCf of the AlN SAW devices vs (a) the normalized thickness of AlN film and (b) the operating frequency. (c) The highest temperature and (d) temperature span have been tested for AlN SAW on various substrates.

8. Discussion on the TCf of AlN SAW resonators

Figure 24 provides a summary of the relationship between the TCf and the normalized thickness of the AlN film (h_{AlN}/λ) as well as the frequency. Overall, the absolute TCf value decreases as the h_{AlN}/λ increases. This trend can be attributed to the thicker AlN film, which effectively constrains most of the SAW, causing the TCf to be primarily influenced by the AlN layer rather than the underlying substrate. However, when h_{AlN}/λ is relatively smaller, the SAW can penetrate the AlN layer, resulting in an impact on the TCf that becomes dependent on the properties of the substrate materials. It is noteworthy that for similar h_{AlN}/λ values, the TCf varies among different substrate materials. SiC and quartz exhibit better performance in minimizing the TCf compared to other substrates. Most of the AlN SAW studies focus on frequencies below 1 GHz, and no significant frequency-dependent TCf is observed within this range. The variability in reported TCfs across different studies highlights the intricate nature of TCf and emphasizes the necessity for further experiments with controlled variables to gain a more comprehensive understanding of its behavior.

In terms of the operating temperature range, the TCf studies on AlN SAW devices based on LiNbO₃, quartz, or diamond substrates have predominantly focused on temperatures within the range of 150 °C. Notably, the highest temperature achieved for AlN SAW

devices utilizing Si substrates has been demonstrated at an impressive 500 °C. However, the TCf of AlN SAW devices on SiC substrates remains a relatively unexplored area despite SiC's tremendous potential for high-temperature applications. Another substrate with notable suitability for high-temperature operation is Al₂O₃, which has demonstrated operation above 1000 °C, showcasing its reliability and resilience under elevated temperature conditions.

B. TCf of AlN SMR

The solid mounted resonator (SMR) is an advanced technology that enables higher operating frequencies in the GHz range, resulting in a significant reduction in size and the ability to handle high power. SMRs offer greater flexibility in electrode thickness and materials.⁴⁵⁶ A typical SMR structure consists of a piezoelectric layer sandwiched between two metal electrodes, mounted on an acoustic reflector, also known as a Bragg mirror. The Bragg mirror comprises alternating layers of high and low acoustic impedance materials designed for high acoustic reflection at the device's operating frequency and to prevent acoustic energy leakage. The top layer acts as an air interface, maximizing total acoustic reflection and minimizing acoustic energy dissipation.

Preliminary studies on the thermal effects of AlN SMRs have shown that the TCf can be influenced by altering the AlN and ZnO

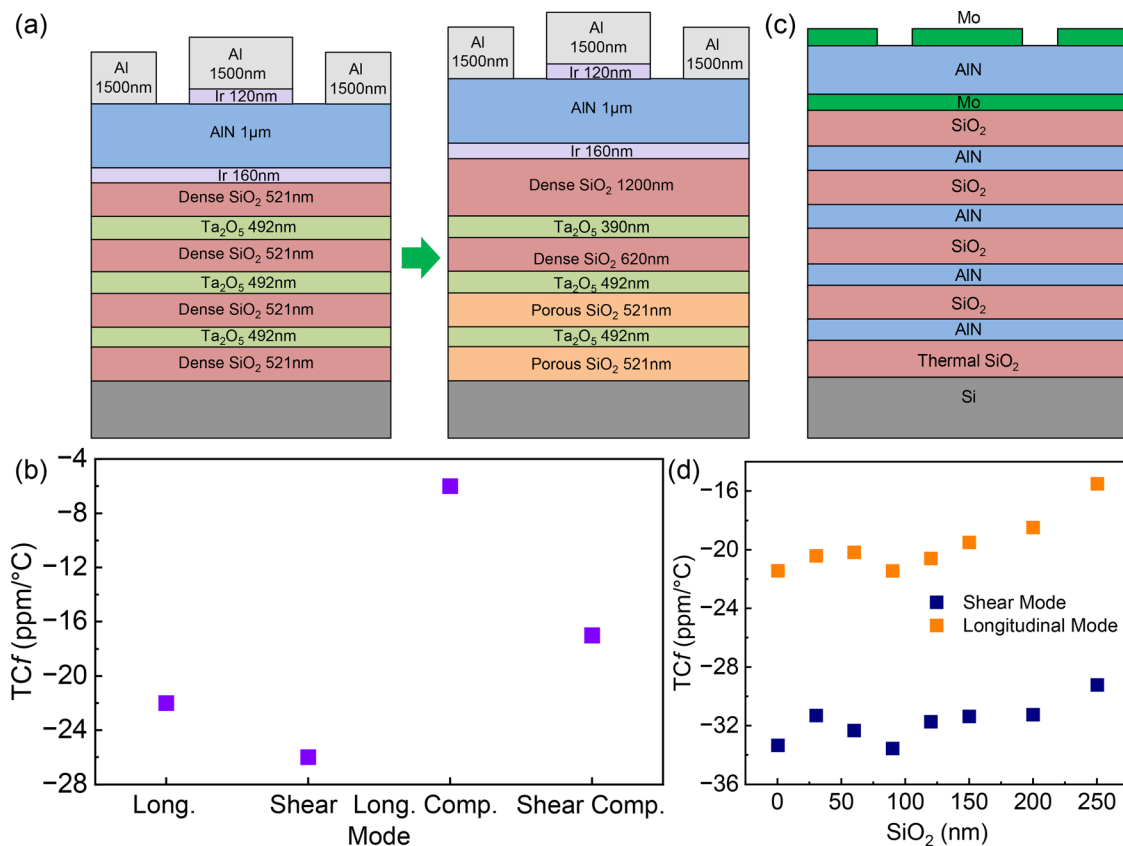


FIG. 25. (a) Structure of the SMR built on Ta₂O₅/dense SiO₂ seven layers symmetric acoustic reflector. (b) Comparison between the TCf of the shear and the longitudinal modes with and without compensation. (c) Structure of the SMR with SiO₂/AlN as acoustic mirror. (d) TCf evolution of the shear and longitudinal mode with deposited SiO₂.

29 June 2025 22:04:31

layer sequence in SMRs with stacked piezoelectric layers of AlN and ZnO. The two resonators exhibit TCfs of -15.8 and -19.9 ppm/ $^{\circ}\text{C}$, respectively, within the temperature range of 25°C – 100°C .⁴⁵⁷ Additionally, doping AlN with chromium (Cr) results in a higher TCf value of -39 ppm/ $^{\circ}\text{C}$ in an SMR utilizing 180-nm AlCrN films deposited on Ir and Mo bottom electrodes.⁴⁵⁸ The shear mode resonant and anti-resonant frequencies of AlN-based SMRs demonstrate different TCfs but identical mass sensitivity, enabling decoupling of mass detection from temperature variations.⁴⁵⁹ Recently, a novel process has been proposed to create fully functional SMRs by transferring high-quality AlN thin films grown on Si wafers using wafer bonding techniques. The TCf of these SMRs is measured to be -14 ppm/ $^{\circ}\text{C}$ within a temperature range of -40°C to 120°C , indicating that the thin-film AlN grown on Si exhibits a positive temperature coefficient of delay.⁴⁶⁰ However, it should be noted that Si substrates are not suitable for SMRs when metallic strips are present on the resonator surface or when integrated into filters or arrays, as Si becomes conductive beyond 250°C and develops significant parasitic capacitance. Researchers have reported that Corning glass substrates can preserve the performance of SMRs up to 400°C .⁴⁶¹

In recent experiments conducted in high-temperature environments, AlN-based SMRs have demonstrated their suitability for challenging applications. SMRs equipped with SiO₂/Mo or SiO₂/AlN

reflectors have proven capable of withstanding temperatures of up to 1000°C during annealing processes. Researchers have performed *in situ* temperature-dependent frequency response tests on SMRs with SiO₂/Mo reflectors, measuring their performance from room temperature up to 550°C . Above 450°C , the signal experiences significant degradation due to the loss of contact between the Al wire and the top electrode of the device. The TCf within the range of room temperature to 450°C is determined to be -20 ppm/ $^{\circ}\text{C}$. For high-temperature applications, Pt or Inconel are identified as the optimal wire materials.⁴⁶²

Compensating for the TCf in SMRs presents technical challenges due to the presence of multiple materials with distinct properties in the stack. Understanding the individual influence of each material on the temperature coefficient becomes complex, necessitating a meticulous design of the compensation structure.⁴⁶³ Studies have indicated that the TCf of AlN SMRs can be engineered by adjusting the thickness and composition of the layers adjacent to the AlN layer. Figure 25(a) illustrates that combining a dense SiO₂ layer with a positive TCf and a Ta₂O₅ layer effectively minimizes the TCf. However, modifying the thickness of these layers reduces mirror reflectivity. To compensate for this effect, porous SiO₂ is utilized for the deepest layers of the reflector due to its lower acoustic impedance and negligible contribution to the TCf in its deep position within the stack. Compared to an SMR with a

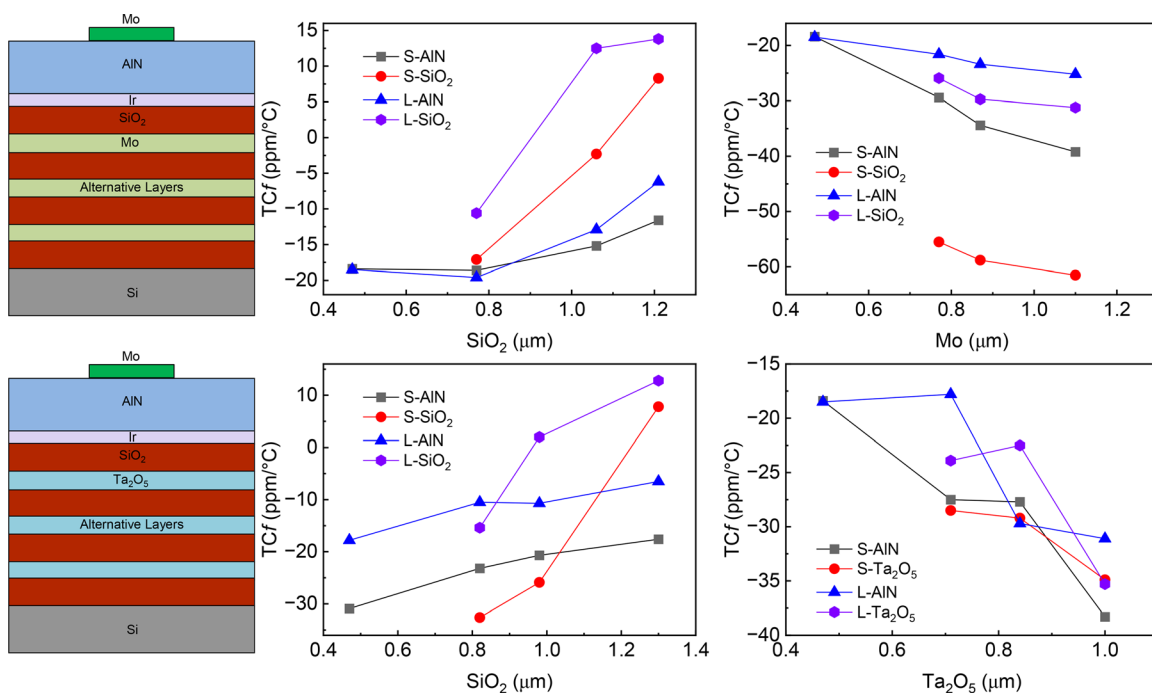


FIG. 26. Structure of the SMR with SiO₂/Mo or SiO₂/Ta₂O₅ as acoustic reflector. TCF of the main (AIN) and secondary (Mo or SiO₂) shear (S) and longitudinal (L) modes for asymmetric resonators as a function of the thickness of SiO₂ and Mo uppermost layers in SMR reflectors.

regular $\lambda/4$ -thick seven-layer-Ta₂O₅/dense SiO₂ acoustic reflector, this device achieves a reduced TCF, specifically decreasing from -26 to -17 ppm/°C for the shear mode and from -22 to -6 ppm/°C for the longitudinal mode, as shown in Fig. 25(b).⁴⁶³ Various factors have been considered to achieve full compensation by adding an SiO₂ layer with an appropriate thickness. However, for biosensing applications involving complex functionalization or mass sensors, the accumulated mass has a significant impact on sensitivity due to energy trapping effects. It is therefore crucial to determine the thickness limit at which the initial TCF and sensitivity of the sensor remain preserved. SMRs with seven alternating layers of SiO₂/AlN exhibit a constant deviation of 2 ppm/°C for SiO₂ deposition up to approximately 150 nm [Figs. 25(c) and 25(d)]. This effect should be considered for accurate sensing applications when detecting very light masses in the ng range.⁴⁶⁴

In-depth studies examining the influence of different materials with specified thicknesses on the TCF of AlN-based SMRs reveal that the TCF is primarily determined by the thickness of the top two layers just below the piezoelectric stack. Increasing the thickness of the SiO₂ layer to nearly twice the ideal $\lambda/4$ -thickness effectively compensates for the TCF in both longitudinal and shear modes. However, varying the thickness of the uppermost high acoustic impedance layer (Mo or Ta₂O₅) makes the TCF of all modes more negative (Fig. 26).⁴⁶⁵

C. TCF of AlN LWR

Lamb waves are a remarkable type of guided wave that propagates through thin plates or sheets of various materials. Named after Horace Lamb, a renowned British mathematician and physicist, Lamb waves were first introduced in 1917 through his mathematical

theory.⁴⁶⁶ Unlike bulk waves, which propagate through the entire thickness of a material, Lamb waves travel solely along the surface of the material, confined to a thin layer near the surface. Consequently, they are highly responsive to any changes in the surface layer

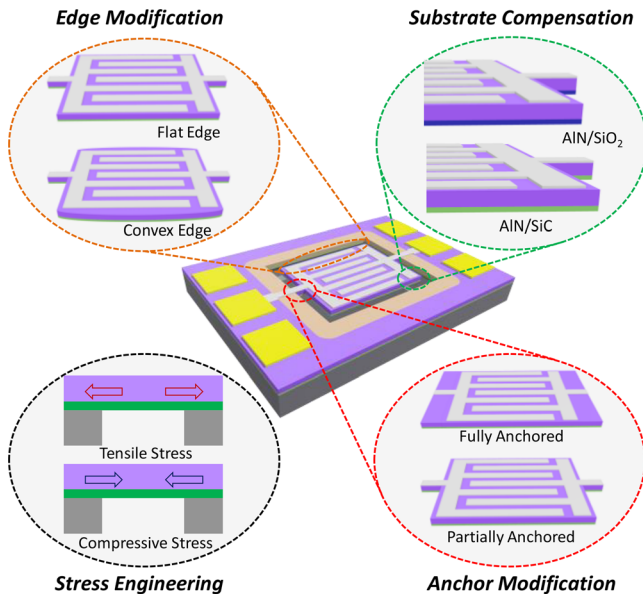


FIG. 27. Commonly used passive compensation techniques for AlN LWR.

properties, such as damage, defects, or alterations in material properties. Lamb waves have a complex dispersion relationship that depends on the plate's geometry, material properties, frequency, and mode of excitation. They can propagate in various modes, including symmetric and antisymmetric modes, and can exhibit interference patterns that can detect the location and nature of surface defects. A Lamb wave resonator is a type of acoustic resonator that uses Lamb waves to create a resonant cavity in a thin plate or sheet of material. A Lamb wave resonator (LWR) typically consists of a thin film of piezoelectric material deposited on a substrate, with interdigital transducers (IDTs) patterned on top. When an electrical signal is applied to the IDTs, an electric field is generated, causing the piezoelectric layer to vibrate and produce Lamb waves. These waves propagate back and forth between the IDT electrodes, forming a standing wave pattern that defines the resonant frequency. LWRs have several advantages over other types of resonators, including lower cost, smaller size, and compatibility with standard microfabrication processes. They are also highly sensitive to changes in the properties of the plate, such as temperature or mass loading, which makes them useful for sensing and measurement applications.

Several studies have been conducted to examine the thermal effects on the resonance of AlN LWRs.^{467–471} A noteworthy AlN/SiO₂/Si composite structure-based LWR displays a TC_f of -31 ppm/°C within the temperature range of 20 °C–70 °C.³⁰³ It has been demonstrated that the addition of an appropriately thick SiO₂ layer can achieve temperature compensation and a zero TC_f in AlN LWRs due to the positive TCE_y of SiO₂. For example, a zero TC_f at 40 °C has been achieved in an AlN/SiO₂ LWR, with respective relative thicknesses of $h_{\text{AlN}}/\lambda = 0.1667$ and $h_{\text{SiO}_2}/\lambda = 0.07$.⁴⁷² Another study has demonstrated excellent temperature compensation utilizing 0.83 μm SiO₂ ($h_{\text{SiO}_2}/\lambda = 0.075$) and 1 μm AlN ($h_{\text{AlN}}/\lambda = 0.0905$).^{473,474}

In addition to adding the SiO₂ compensation layer, other passive compensation efforts have been devoted. Figure 27 illustrates the commonly used passive compensation techniques for AlN LWR. Theoretical analyses indicate that incorporating a 3C-SiC layer with a carefully designed thickness can enhance the electromechanical coupling strength, bolster the Q factor, and reduce the TC_f. It has been experimentally demonstrated that the 3C-SiC layer efficiently increases the k_i^2 from 0.05% to 0.23%, boosts the Q from 1840 to 5510, and reduces the TC_f to -14.76 ppm/°C for the third-order quasi-symmetric Lamb wave mode in a composite membrane composed of a 2.5-μm AlN film and a 2.6-μm 3C-SiC layer.⁴⁷⁵ Efforts to engineer the TC_f have been demonstrated through optimization of the device structure. Notably, the TC_f remains nearly identical for AlN plates with flat and convex edges, while the AlN plate with convex edges exhibits a significant 2.6× increase in Q compared to the resonator with flat edges.⁴⁷⁶ To mitigate self-heating and reduce overall thermal resistance, the AlN LWR with the suspended resonant body is fully anchored to the Si substrate instead of being partially anchored via narrow tethers. Note that there is no apparent difference in the TC_f between the fully anchored and partially anchored devices in open loop measurement.³²⁰ Research has revealed that the in-plane tension of a composite plate plays a significant role in temperature stability. When subjected to initial tensile film stress, the in-plane tension decreases, leading to a constant zero deflection as the temperature rises. Conversely, in cases of initial compressive film stress, the plate experiences zero tension due to undulations, and the stress conditions remain unaltered as the temperature increases.³²²

In high-temperature applications, an AlN LWR operating in air displays a linear TC_f of -24.7 ppm/°C from room temperature up to 600 °C. However, when a compensation layer of SiO₂ with a thickness of 1.13 or 1.39 μm is added, the TC_f curves exhibit strong quadratic behavior and reveal turnover temperatures (local maxima) across the entire measured temperature range. Surprisingly, the SiO₂-compensated devices experience even more severe degradation in Q compared to those without an oxide layer. The observed decrease in Q with temperature can be attributed to material softening, thermoelastic damping, and/or thin film stress.³¹⁰ Since Al has a low melting point of 660 °C, it is not ideal for high-temperature applications. Therefore, Pt, with a significantly higher melting point of 1768 °C, is used as the metallization for the bottom electrode and the IDT in AlN LWRs designed to operate at temperatures up to 700 °C. The turnover temperature can be controlled by adjusting the normalized thicknesses of AlN (h_{AlN}/λ) and SiO₂ (h_{SiO_2}/λ). By varying these parameters, a zero TC_f can be achieved at 214, 430, and 542 °C. However, accurately predicting the exact position of the turnover temperature is challenging as it heavily relies on the TCE_y values of AlN, SiO₂, and the IDT electrode. With reliable TCE_y data, it becomes possible to accurately forecast the turnover point of AlN/SiO₂ LWRs.^{333,477,478}

Figure 28 provides an extensive overview of the intricate relationship between the TC_f and various influencing factors, including the normalized thickness of the AlN film, the normalized thickness of SiO₂, frequency, and the highest operating temperature. Notably, for SiO₂ compensated AlN LWRs, the absolute TC_f values predominantly reside within the range of 20 ppm/°C, signifying a substantial reduction when compared to the uncompensated counterparts. Interestingly, the TC_f does not exhibit a discernible dependency on h_{AlN}/λ , but rather demonstrates significant fluctuations when h_{AlN}/λ falls below 0.1. These fluctuations are indicative of acoustic wave leakage into the SiO₂ layer, a relationship further corroborated by the TC_f's association with the SiO₂ thickness, as depicted in Fig. 28(b). Additionally, it is worth noting that the majority of AlN LWRs operate at frequencies below 4 GHz, with no noteworthy frequency-dependent TC_f observed [Fig. 28(c)]. The highest operating temperature is 700 °C, although the majority of measurements were conducted within the 200 °C range.

D. TC_f of AlN TPoS

Thin-film piezoelectric-on-substrate (TPoS) is a class of lateral extensional resonator, which benefits from piezoelectric transduction. These resonators require a very thin layer of piezoelectric material, thereby the residual stress in the film is tolerable. Compared with the device with only a thin piezoelectric layer, the low-loss substrate leads to improved structural integrity and enhance the power handling ability. It has been observed that the turnover point of TC_f in TPoS resonators can be influenced by factors such as crystalline orientation, doping concentration, and the thickness ratio between the substrate (Si) and the piezoelectric film in the resonant structure.⁴⁷⁹

For TPoS resonators with pure Si aligned to the [110] plane, the resonance frequency drifts linearly within the temperature range of -40 °C to 85 °C. Lightly doped resonators (with doping concentration below $1 \times 10^{16} \text{ cm}^{-3}$) exhibit a TC_f of -28.6 ppm/°C, whereas devices based on n-type-doped Si (with doping concentration of approximately $5 \times 10^{19} \text{ cm}^{-3}$) show a 40% improvement, with a TC_f of -17 ppm/°C. However, for [100]-aligned devices, a typical parabolic

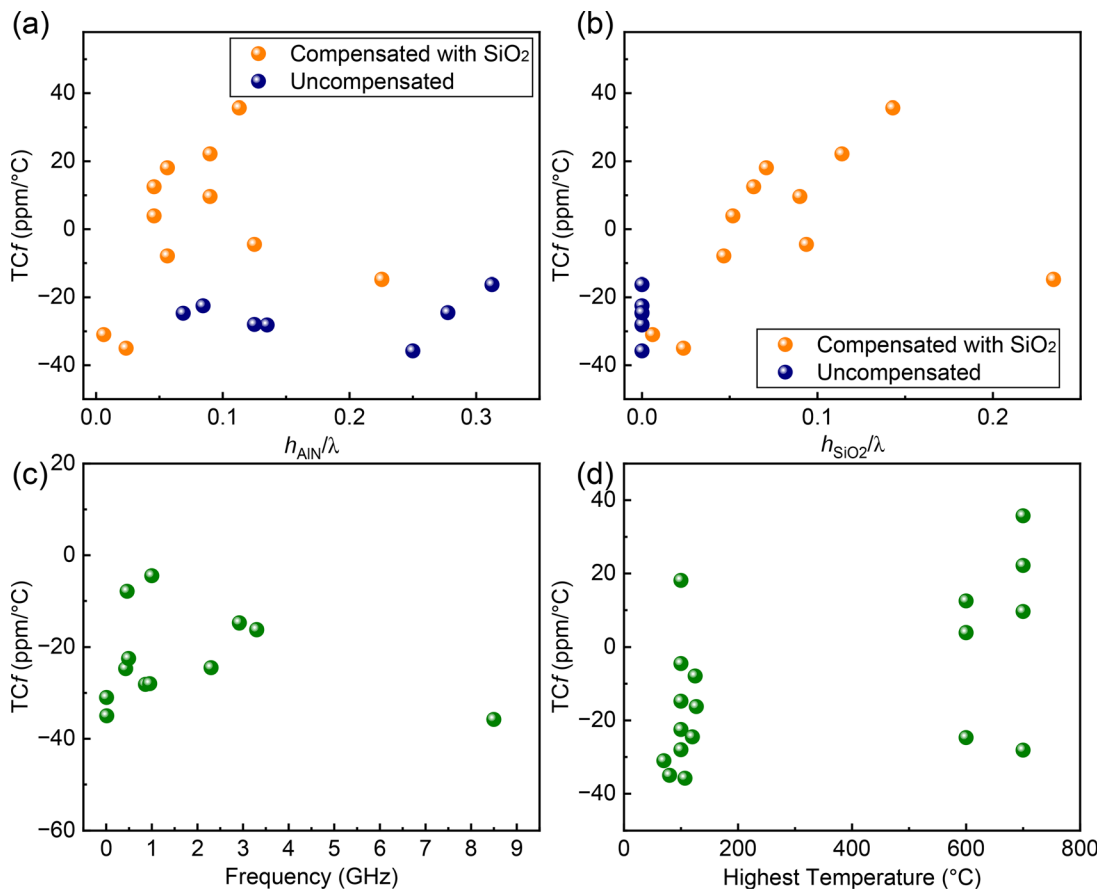


FIG. 28. Variation of the TCf of the AlN LWRs vs (a) the normalized thickness of AlN film, (b) normalized thickness of SiO₂, (c) the operating frequency, and (d) the highest operating temperature.

trend is observed, featuring a turnover point. The overall temperature-induced frequency variation remains below 245 ppm, which is significantly smaller than that of the [110]-aligned device. The turnover point shifts toward higher temperatures as the device thickness and doping concentration increase. The turnover point of TCf can be adjusted by changing the dopants,⁴⁸⁰ as shown in Fig. 29.

Incorporating an oxide layer within the Si body of an AlN-on-Si resonator yields a significantly reduced TCf of -2.4 ppm/°C within the temperature range of 20 °C–70 °C. This TCf value is more than 12 times smaller than that extracted for an uncompensated device.⁴⁸¹ Furthermore, through the uniform distribution of an array of SiO₂ pillars within the Si body of an AlN-on-Si resonator, a parabolic temperature-frequency characteristic is achieved. This characteristic exhibits a frequency shift of 83 ppm over the temperature range of -20 °C to 100 °C, which is approximately 45 times smaller than that measured from the uncompensated counterpart. Notably, a local zero TCf is observed at 40 °C.⁴⁸²

E. TCf of AlN CMR

The AlN contour-mode resonator (CMR) has emerged as a highly promising solution for enabling the fabrication of multiple

frequencies (ranging from 100 MHz to 10 GHz) and high-performance resonators on a single Si substrate. It has been successfully utilized in synthesizing miniaturized reconfigurable CMOS oscillators with remarkable characteristics such as low phase noise and low jitter values.³²⁰ The resonance frequency of both rectangular plate and ring-shaped CMRs, featuring a piezoelectric AlN body sandwiched between bottom and top electrodes, spans a range from 19 to 656 MHz, exhibiting high Q up to 4300. Uncompensated AlN CMRs display a TCf of -25 ppm/°C.⁴⁸³ In the case of a contour-mode MEMS AlN piezoelectric ring resonator, heavily doped Si was utilized as the bottom electrode. The resonance frequency shows a linear downshift with temperature change in both cryogenic cooling tests down to 77 K and heating tests up to 400 K, resulting in a TCf of -9.1 ppm/°C. Interestingly, lower temperatures correspond to higher quality factors, with an increase in 56.43% observed—from 1291.4 at 300 K to 2020.2 at 77 K.³¹⁵ The incorporation of a passive temperature compensation technique involves increasing the SiO₂ thickness in the Al/AlN/Al/SiO₂ ring resonator. Initially, this leads to a smaller negative TCf, but eventually, the TCf transitions to a positive value. Overall, the TCf has been reduced from -21 to 2.5 ppm/°C by increasing the SiO₂ thickness from 400 to 1150 nm.⁴⁸⁴ These results are summarized in Fig. 30.

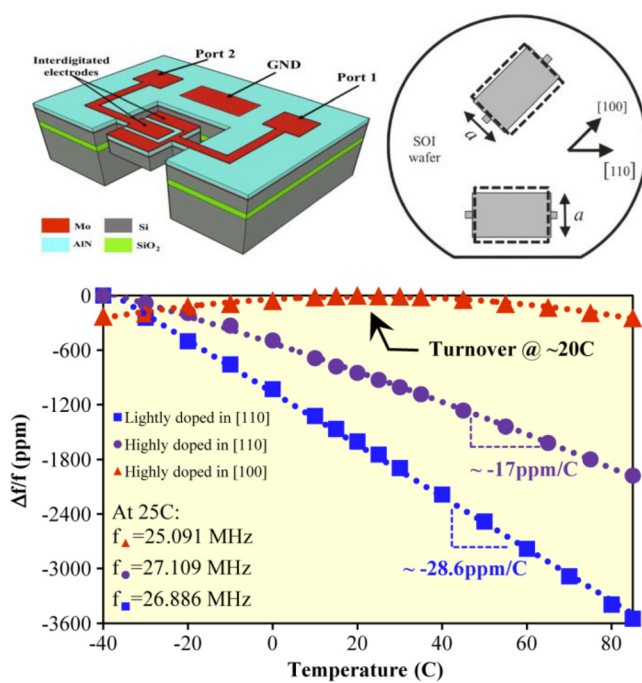


FIG. 29. Schematic representation of a TPoS resonator aligned to [110] and [100] planes in SOI wafer. Measured resonance frequency drift vs temperature for TPoS resonators with pure silicon aligned to [110] plane and n-type-doped silicon ($N \sim 5 \times 10^{19} \text{ cm}^{-3}$) aligned to [110] and [100] planes (Shahmohammadi *et al.*, IEEE Trans. Electron Devices **60**, 1213 (2013). Copyright 2013 IEEE, Creative Commons).⁴⁸⁰

Both passive and active compensation techniques have been employed in an AlN-on-SOI piezoelectric resonator operating in width extensional mode at 27.19 MHz, which achieves an impressive Q of 9520. The presence of SiO_2 within the composite resonator contributes to an overall reduction in $\text{TC}f$, resulting in a frequency drift of less

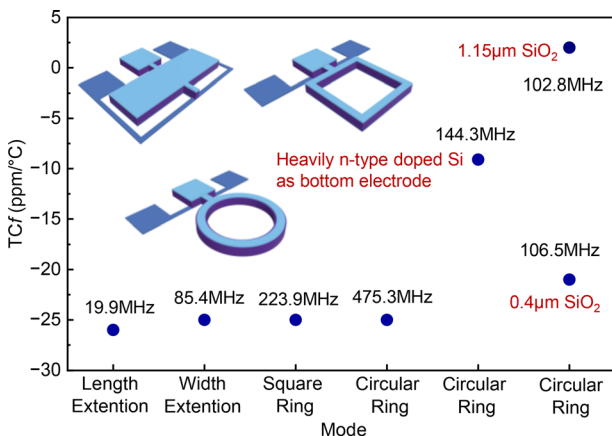


FIG. 30. $\text{TC}f$ of AlN CMRs. Inset shows the schematic of AlN rectangular plate resonator, square-shaped ring resonator, and circular ring resonator.

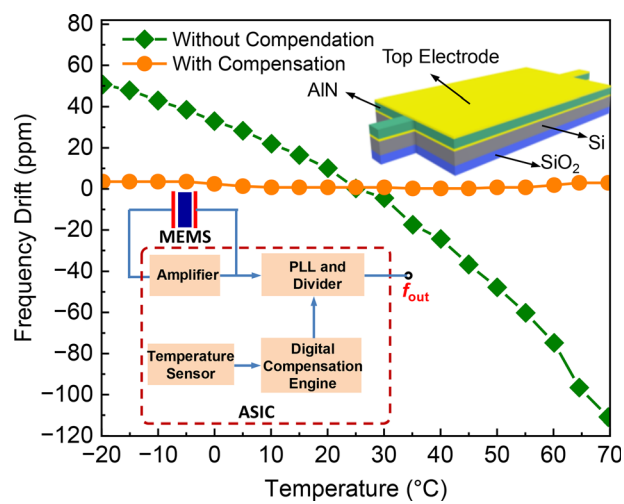


FIG. 31. Comparison of the frequency drifts of AlN width extensional (WE) mode resonator before and after the active temperature compensations. Inset shows the schematic view of the device and block diagram of ASIC (Wu *et al.*, IEEE Trans. Ind. Electron. **65**, 4 (2018). Copyright 2018 IEEE, Creative Commons).⁴⁸⁵

than 160 ppm over the temperature range of -20°C to 70°C . Furthermore, with the implementation of active compensation, the frequency drift is further reduced to less than 3 ppm across the entire temperature range, as shown in Fig. 31. To facilitate integration and monitoring, the diced resonator is interfaced with a customized application-specified integrated circuit (ASIC) featuring an on-chip temperature sensor. This sensor enables real-time temperature monitoring and provides a digital temperature reference to the digital compensation engine.⁴⁸⁵

XII. $\text{TC}f$ OF $\text{Al}_{1-x}\text{Sc}_x\text{N}$ MEMS

The incorporation of scandium (Sc) into the hexagonal wurtzite structure leads to a significant improvement in piezoelectric properties.

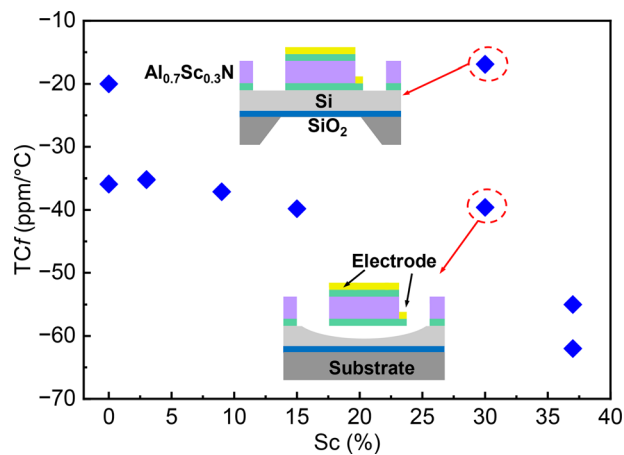


FIG. 32. Comparison of $\text{TC}f$ measured in $\text{Al}_{1-x}\text{Sc}_x\text{N}$ FABRs with various Sc concentration. Inset shows the schematic of $\text{Al}_{1-x}\text{Sc}_x\text{N}$ FBAR released from front side and back side, respectively.

For instance, the piezoelectric coefficient d_{33} increases from 8.4 pC/N for AlN to 23.6 pC/N for $\text{Al}_{1-x}\text{Sc}_x\text{N}$ at 33% Sc concentration. Moreover, a broad peak with high piezoelectric coefficients ranging from 26.9 to 27.3 pC/N is observed between 35% and 43% Sc content.⁴⁸⁶ In addition, $\text{Al}_{1-x}\text{Sc}_x\text{N}$ films exhibit a high spontaneous polarization of above 100 $\mu\text{C}/\text{cm}^2$, providing significant potential for scaling up in ferroelectric random-access memory (FeRAM) devices, leading to increased memory density and reduced power consumption. Its impressive properties, such as tunable coercive electric field (2–7 MV/cm), wide bandgap (4.0–6.2 eV), and high-temperature phase stability (up to 1100 °C), make $\text{Al}_{1-x}\text{Sc}_x\text{N}$ a promising candidate for future electronic devices that can operate under extreme environmental conditions. With its high piezoelectric coefficients and giant remanent polarization, $\text{Al}_{1-x}\text{Sc}_x\text{N}$ is a highly attractive material for a wide range of applications, including actuators, sensors, and memory devices.^{301,487,488} Consequently, the thermal response of $\text{Al}_{1-x}\text{Sc}_x\text{N}$ MEMS has gradually attracted attention.⁴⁸⁹ In this section, we summarize the up-to-date published studies on the TCf for $\text{Al}_{1-x}\text{Sc}_x\text{N}$ MEMS resonators.

A. TCf of $\text{Al}_{1-x}\text{Sc}_x\text{N}$ FBAR

The concentration of Sc has a significant impact on the TCf of $\text{Al}_{1-x}\text{Sc}_x\text{N}$ FBAR, which has led to extensive research in this field. Figure 32 presents the comparison of TCf measured in AlScN FBARs with different Sc concentrations. Increasing the Sc concentration from 0 to 15% results in a slight TCf increase from -35.9 to -39.8 ppm/°C within the temperature range of 25 °C–125 °C.⁴⁹⁰ In another study, when the Sc concentration remains below 20%, a stable TCf of -27.2 ppm/°C is consistently observed for AlScN FBAR within the temperature range of 30 °C–90 °C.⁴⁹¹ These findings suggest that the TCf remains stable as long as the Sc concentration remains below 20%. An $\text{Al}_{0.7}\text{Sc}_{0.3}\text{N}$ FBAR operating at 3.17 GHz exhibits a high k_t^2 of 18% with a Q of 328. The TCf of the FBAR has been measured to be -39.6 ppm/°C in the range from 200 to 600 K. As shown in Fig. 32, instead of releasing the device from the front side by etching the Si device layer, $\text{Al}_{0.7}\text{Sc}_{0.3}\text{N}$ -on-Si composite FBAR released from the backside exhibits a better thermal stability due to the 3.5- μm -thick Si passive layer underneath the resonator stack, with a TCf of -16.9 ppm/°C in the same temperature range.^{492,493} When further increase the concentration of Sc to 37%, TCf values were measured to be -55 and -62 ppm/°C, respectively, in the temperature range from room temperature up to 600 °C, for the quasi-extensional mode and quasi-shear mode of FBAR based on c-axis tilted $\text{Al}_{0.63}\text{Sc}_{0.37}\text{N}$ films, which are much larger than those obtained in non-doped AlN with the TCf of -20 and -27 ppm/°C, respectively.⁴⁹⁴

B. TCf of $\text{Al}_{1-x}\text{Sc}_x\text{N}$ SAW

$\text{Al}_{1-x}\text{Sc}_x\text{N}$ SAW has been demonstrated on various substrates, with the measured TCf exhibiting a strong dependency on the substrate material. SAW resonators based on $\text{Al}_{0.77}\text{Sc}_{0.23}\text{N}$ and sapphire substrates demonstrate, on average, approximately 1.2 ppm/°C lower TCf values compared to those on Si substrates. Furthermore, they exhibit a notable increase in resonance frequency of approximately 3% and a relative increase in electromechanical coupling of 9.6%. The relationship between TCf and Sc concentration in $\text{Al}_{1-x}\text{Sc}_x\text{N}/\text{Al}_2\text{O}_3$ SAW resonators exhibits a non-linear trend.³⁰¹ However, the exact cause of

this non-linearity remains uncertain, primarily due to limited reports on only one of the CTEs that determine TCf. The TCf of a $\text{Al}_{0.8}\text{Sc}_{0.2}\text{N}$ SAW on GaN/sapphire heterostructure, measured for the Rayleigh mode and the 4th Sezawa mode, are -32.1 and -26.7 ppm/°C, respectively, spanning a broad temperature range from 260 to 600 K.⁴⁹⁵ A SAW resonator incorporating $\text{Al}_{0.74}\text{Sc}_{0.26}\text{N}$ and polycrystalline diamond heterostructures showcases a highly linear frequency response to temperature across two distinct temperature ranges. From 20 K to room temperature, it demonstrates a TCf of -12.5 ppm/°C, while from 300 up to 450 K, the TCf measures -34.6 ppm/°C. This behavior can be attributed to a desorption effect occurring during the substrate heating process. Furthermore, the k_t^2 values show a slight increase with temperature up to 300 K but experience a 20% reduction upon further increasing the substrate temperature to 450 K. This phenomenon can be explained by the diminished conversion efficiency between electric and acoustic energy within the piezoelectric thin film due to scattering effects caused by lattice thermal vibrations.⁴⁹⁶ The TCf of SAW resonators utilizing a 400-nm-thick crystalline $\text{Al}_{0.88}\text{Sc}_{0.12}\text{N}$ substrate has been measured to be -102 ppm/°C within the temperature range of 150–600 K. Comparatively, this TCf value is larger than that observed in a LWR based on the same $\text{Al}_{0.88}\text{Sc}_{0.12}\text{N}$ substrate, which exhibits a lower TCf of -59.4 ppm/°C. The notable difference can be attributed to the fully suspended geometry of the LWR, effectively mitigating the stress arising from the thermal expansion coefficient mismatch between AlScN and the Si substrate.⁴⁹⁷

Figure 33 illustrates a comparison of the reported TCf values for AlScN SAW devices. The measured TCf values predominantly range between -20 and -40 ppm/°C. Notably, the smallest and largest TCf values recorded are -12.5 and -102 ppm/°C, respectively. Various substrate materials, including Si, Al_2O_3 , diamond, and GaN, have been utilized in the fabrication of these devices, but no discernible pattern emerges regarding the substrate's impact on TCf. The highest operating temperature assessed in these studies is 325 °C. The absolute TCf values generally exhibit an increasing trend as the normalized thickness of the AlScN film is increased.

C. TCf of $\text{Al}_{1-x}\text{Sc}_x\text{N}$ LWR

The TCf of $\text{Al}_{1-x}\text{Sc}_x\text{N}$ LWRs has been reported to be affected by several factors, including Sc concentration, the relative thickness of $\text{Al}_{1-x}\text{Sc}_x\text{N}$ with respect to wavelength, temperature range, and the different resonant modes with varying frequencies. LWRs based on 500-nm-thick $\text{Al}_{0.85}\text{Sc}_{0.15}\text{N}$ and $\text{Al}_{0.78}\text{Sc}_{0.22}\text{N}$ thin films achieve a Q of over 1000 at resonant frequency of ~300 MHz, as well as 80% and 152% improvement in k_t^2 , compared to pure AlN device. The TCf measured in the range from 25 °C to 120 °C is extracted to be -44 and -46 ppm/°C, respectively.⁴⁹⁸ In the same temperature range, a very close TCf of -44 ppm/°C is measured from a LWR based on 500-nm-thick $\text{Al}_{0.85}\text{Sc}_{0.15}\text{N}$.⁴⁹⁹ Due to the increased CTE and reduced elasticity modulus of $\text{Al}_{1-x}\text{Sc}_x\text{N}$ film as the Sc concentration increases, a larger TCf of -55.92 ppm/°C is extracted in the temperature range of 25 °C–120 °C from a LWR based on 1- μm -thick $\text{Al}_{0.7}\text{Sc}_{0.3}\text{N}$.⁵⁰⁰ Compared with the LWRs with flat boundaries, the same LWRs with butterfly-shaped structure achieve 40% progress in figure of Merit (FoM), with a high k_t^2 of 9.7%. The butterfly-shaped boundaries effectively suppress the displacement in the anchor region, leading to a higher Q due to less energy dissipation. However, it has no effects on the TCf, which is

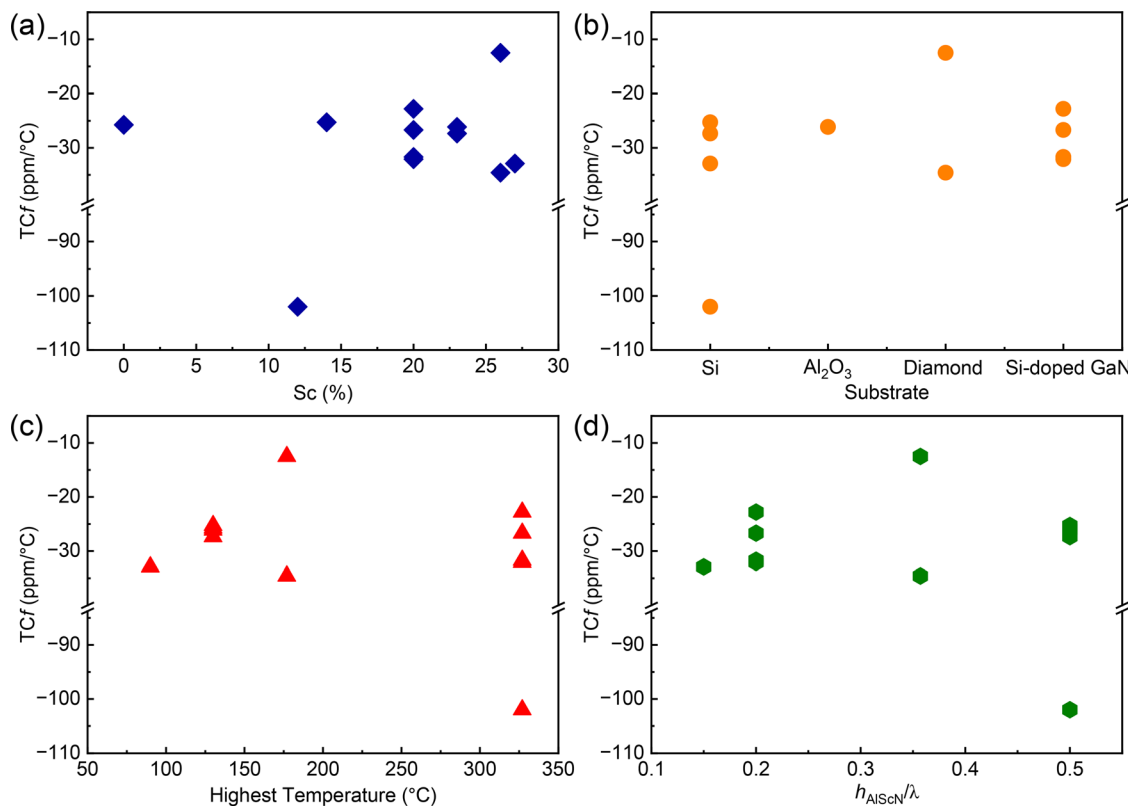


FIG. 33. Variation of the TCf of AlScN SAW vs (a) Sc concentration, (b) substrate materials, (c) the highest operating temperature, and (d) the normalized thickness of AlScN film.

29 June 2025 22:04:31

measured to be $-54.97 \text{ ppm/}^\circ\text{C}$ in the temperature range of 20°C – 70°C ,⁵⁰¹ as shown in Fig. 34.

The TCf of $\text{Al}_{1-x}\text{Sc}_x\text{N}$ LWRs can be engineered by sputtering SiO_2 compensation layer on top of the released resonators. One of the advantages of this method is the simultaneous compensation for different resonant modes with varying frequencies. However, it has been demonstrated that $\text{Al}_{0.83}\text{Sc}_{0.17}\text{N}$ LWRs operating at different frequencies require slightly varying thicknesses of SiO_2 to achieve a zero TCf. Interestingly, when the SiO_2 thickness exceeds that of the resonator stack, the linear frequency response to temperature transforms into a quadratic behavior. By introducing a $1.5\text{-}\mu\text{m}$ SiO_2 layer, near-zero TCf was successfully achieved for AlScN LWRs operating up to 500 MHz.⁵⁰²

Figure 34 illustrates a comparison of the reported TCf values for AlScN LWR devices. The measured TCf values mostly range between -20 and $-60 \text{ ppm/}^\circ\text{C}$ without compensation. The highest operating temperature examined in these studies is 800°C .³³⁰ The smallest and largest recorded TCf values are 0.53 and $-59.4 \text{ ppm/}^\circ\text{C}$, respectively. Interestingly, the absolute TCf values exhibit a significant increase with the normalized thickness of the AlScN film, while the incorporation of a SiO_2 compensation layer leads to a decrease in TCf values. By employing SiO_2 compensation, precise control of TCf within $\pm 10 \text{ ppm/}^\circ\text{C}$ is readily achieved. Notably, a minimal TCf of $0.53 \text{ ppm/}^\circ\text{C}$ has been attained through meticulous adjustments to the SiO_2 layer thickness.

D. TCf of $\text{Al}_{1-x}\text{Sc}_x\text{N}$ TPoS

TCf compensation has been demonstrated in AlScN TPoS resonators. An active wireless MEMS temperature sensor based on a $\text{Al}_{0.8}\text{Sc}_{0.2}\text{N}$ -on-Si TPoS with center frequency at 27 MHz has been demonstrated with a near-constant TCf of $-24.9 \text{ ppm/}^\circ\text{C}$ and a minimum sensitivity of 0.011°C across the temperature range from -40°C to 140°C .⁵⁰³ Degenerate doping of the Si layer at a level of $\sim 5 \times 10^{20} \text{ cm}^{-3}$ in combination with specific crystal axis alignment and optimized thickness ratios between $\text{Al}_{0.85}\text{Sc}_{0.15}\text{N}$ ($0.3 \mu\text{m}$) and Si ($2 \mu\text{m}$) has achieved a TCf of $-7.4 \text{ ppm/}^\circ\text{C}$ in AlScN TPoS devices.⁵⁰⁴

XIII. TCf OF GaN MEMS

Gallium Nitride (GaN) is a wide-bandgap semiconductor material with remarkable properties such as high breakdown voltage, high electron mobility, and excellent thermal conductivity.^{505,506} These qualities make GaN a highly sought-after material for various applications, such as power electronics, RF electronics, lighting, and sensing. GaN MEMS, in particular, show tremendous promise for various applications, including communications, sensing, energy harvesting, and biomedical engineering.^{507,508} GaN MEMS devices are known to operate seamlessly even in harsh environments, including high temperatures and high radiation levels, making them well-suited for aerospace and defense applications.^{509,510} However, the manufacturing of native GaN substrates with high thermal conductivity and low lattice

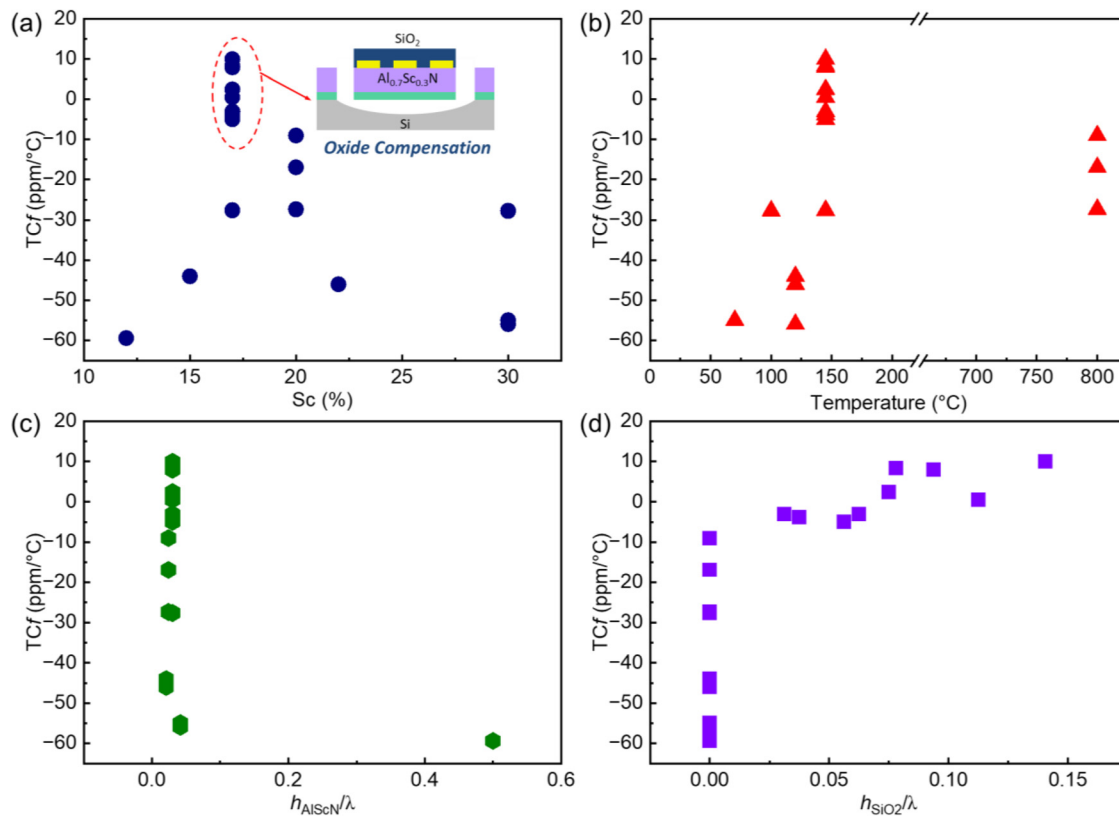


FIG. 34. Variation of the TCf of AlScN LWRs vs (a) Sc concentration, (b) the highest operating temperature, (c) the normalized thickness of AlScN film, and the normalized thickness of SiO₂ compensation layer.

29 June 2025 22:04:31

mismatch with GaN epilayers remains a significant challenge. This limitation hinders the widespread and rapid adoption of GaN devices.⁵¹¹ Significant effort has been dedicated to growing GaN epitaxial films on sapphire and SiC substrates. Sapphire substrates have low thermal conductivity, while SiC substrates are costly despite being well-suited for thermal management. Recently, the epitaxial growth of III-nitride films and heterostructures on Si (111) substrates has garnered attention due to the availability of low-cost, large-sized Si substrates, compatibility with standard Si processes, and potential integration with Si-based devices.⁵¹² However, the growth of GaN on Si is hindered by the large lattice mismatch and CTE mismatch between GaN and Si, resulting in tensile stress during cooling from the high growth temperature.⁶⁴ This mismatch can affect the quality and performance of epitaxial films and devices. This section provides a summary of the research on the impact of temperature on GaN MEMS resonators.

A. TCf of GaN MEMS operating in flexural mode

Cantilever and beam resonators, known for their high Q and small mass, have been widely utilized as sensitive detectors of motion, force, and mass. The TCf of the flexural mode of GaN beam and cantilever has been reported. GaN/AlN heterostructure doubly clamped micro-string resonators offer the highest TCf values up to -512 ppm/°C in the temperature range from 25 °C to 325 °C.⁶⁴ A

linear dependence of resonance frequencies on temperature has been observed near room temperature in GaN nanowires with a typical length of 15 μm and diameter of 100 nm, with a TCf of ~40 ppm/°C.⁵¹³ Stress-relieved GaN cantilever resonator exhibits a TCf of -12.39 ppm/°C in the temperature range of 300–600 K, while the stress modulated buckling modes of GaN beam exhibit excellent frequency stability with increasing temperature, with the TCf varying from -6 ppm/°C near room temperature to -13 ppm/°C at 600 K,^{514,515} as shown in Fig. 35. The improved frequency stability achieved through strain engineering may open the avenue of GaN MEMS for sensing, timing, and filtering applications, especially in harsh environments.

B. TCf of GaN SAW

The TCf of GaN SAW resonators has been extensively studied and has been reported in the range from -40 to 70 ppm/°C without compensation. The TCf of SAW on GaN/sapphire substrate is -60.8 to -50.0 ppm/°C in the temperature range from -25 °C to 50 °C.⁵¹⁶ A SAW filter with AlGaN/sapphire structure exhibits a similar TCf of -51.2 ppm/°C in the temperature range of -30 °C to 60 °C.⁵¹⁷ A slightly higher TCf of -61.82 ppm/°C is reported in another study on GaN SAW on sapphire substrate.⁵¹⁸ A smaller TCf of -40 ppm/°C was measured from GaN SAW resonators operating at 5.4–8.5 GHz in the temperature range of 20 °C–150 °C.⁵¹⁹ TCf for bulk GaN SAW resonators is slightly lower than that for the device fabricated on GaN film

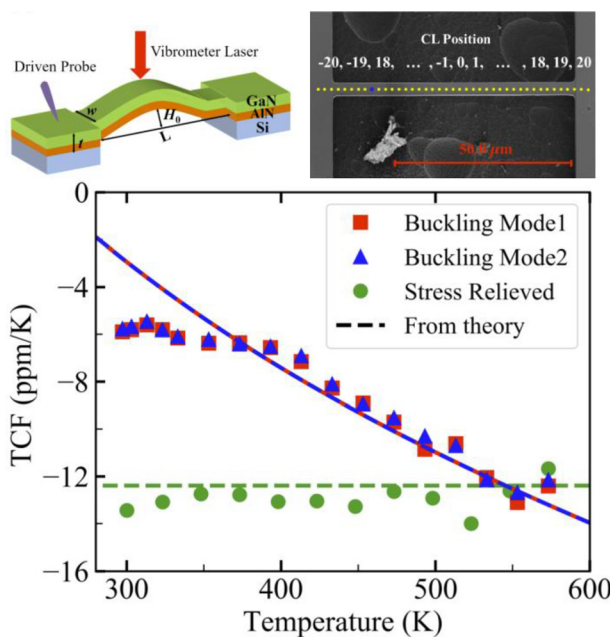


FIG. 35. The temperature dependence of TCf for the flexural mode and the buckling mode of GaN cantilever and beam (Sun *et al.*, J. Appl. Phys. 131, 054502 (2022). Copyright AIP Publishing, Creative Commons).

grown on sapphire substrate.⁵²⁰ Nonlinear changes in frequency with respect to temperature have been observed in GaN SAW devices over a wider temperature range of -267°C to 150°C . The sensitivity ($\text{d}f/\text{dT}$) is lower at negative temperatures, especially below -180°C . Additionally, a slight increase in TCf has been observed in devices with smaller digit/interdigit spacing.⁵²¹ Furthermore, it has been reported that the resonance of the Rayleigh mode is more temperature-sensitive than the Lamb mode, with TCfs of -75 and $-31\text{ ppm}/^{\circ}\text{C}$, respectively.⁵⁰⁸ Figure 36 illustrates a comparison of the reported TCf values for GaN SAW resonators. The variation in TCfs reported across different studies underscores the complexity of TCf, which is influenced by various factors, including material properties, device structure, temperature regulation techniques, measurement setup, and environmental conditions, etc.

Doping has proven to be effective in tuning the TCf in GaN SAW. A study investigating the dopant effect reveals that undoped GaN SAW exhibits a TCf of $-60.8\text{ ppm}/^{\circ}\text{C}$, while Zn-doped GaN SAW with a Zn-doping concentration of $9 \times 10^{19}/\text{cm}^3$ shows a TCf of $-46.8\text{ ppm}/^{\circ}\text{C}$. Mg-doped GaN SAW with an Mg concentration of $4.5 \times 10^{18}/\text{cm}^3$ exhibits a TCf of $-18.3\text{ ppm}/^{\circ}\text{C}$.⁵²² In another study focused on extreme low temperature ranges from -196°C to 27°C , the measured TCf is $-22.79\text{ ppm}/^{\circ}\text{C}$ for undoped GaN SAW and $-21.79\text{ ppm}/^{\circ}\text{C}$ for Si-doped GaN SAW. Notably, the high electrical conductivity of Si-doped GaN enables successful compensation of TCf through the Joule heating effect, resulting in a remarkably low TCf of $2\text{ ppb}/^{\circ}\text{C}$.⁵²³

C. TCf of GaN BAW

Compared to SAW devices, GaN BAW resonators have been found to possess smaller absolute TCf, with values below $35\text{ ppm}/^{\circ}\text{C}$.

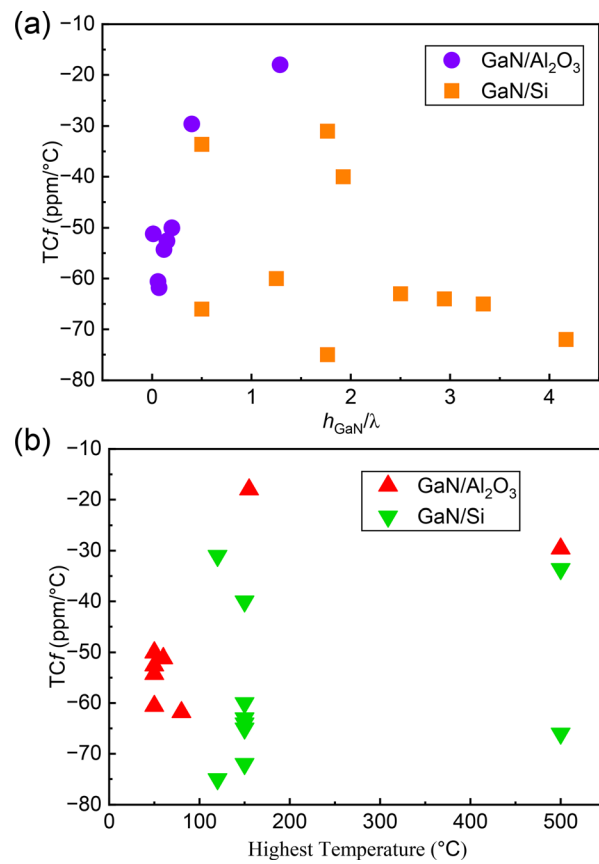


FIG. 36. (a) Variation of the TCf of the GaN SAW devices vs the normalized thickness of GaN film. (b) The highest temperature has been tested for GaN SAW on various substrates.

For instance, a GaN/NbN/SiC epi-HBAR exhibits a linear TCf of $-12\text{ ppm}/^{\circ}\text{C}$ over a temperature range of 290 – 360 K .⁵²⁴ In the case of the thickness-shear mode, a TCf of $-17.9\text{ ppm}/^{\circ}\text{C}$ is measured, which is approximately $6\text{ ppm}/^{\circ}\text{C}$ lower compared to the lateral-extensional modes with a TCf of $-24\text{ ppm}/^{\circ}\text{C}$.⁵²⁵ The fundamental thickness-mode resonance of a GaN BAW resonator exhibits a TCf of $-30\text{ ppm}/^{\circ}\text{C}$, which is higher than the value reported in Ref. 525 due to the presence of a thick AlN (400 nm)/AlGaN (650 nm) layer and thick gold metal electrodes (constituting 10% of the entire stack). However, the deposition of a 400-nm-thick SiO₂ layer with a positive CTE on the stack results in a significant reduction of the GaN-based resonator's TCf by over 50%, from -30 to $-13\text{ ppm}/^{\circ}\text{C}$. Despite not requiring additional fabrication steps, this level of temperature stability is still limited for use in timing references. Future efforts should focus on optimizing the location and thickness of the SiO₂ layer to approach a near-zero TCf.⁵²⁶

XIV. TCf OF ONE- AND TWO-DIMENSIONAL (1D AND 2D) NEMS

There are plenty of room and a plethora of exciting opportunities when scaling resonant MEMS down to sub-micron and the genuinely nanoscale, and even molecular/atomic scale, where resonant

TABLE V. Comparison of TC_f of the reported 2D NEMS resonators.⁵³⁷ (Wu et al., IEEE MEMS (2022). Copyright 2022 IEEE, Creative Commons),⁵³⁸ (Arora et al., IEEE Sensors (2021). Copyright 2021 IEEE, Creative Commons).

Reference	Material	Device image	Dimension	Measurement scheme	Temperature (°C)	f_{ref} (MHz)	TC _f (ppm/°C)	Q
531, 532	Black phosphorus (BP)		Device 1: $t = 85 \text{ nm}$ $d = 9 \mu\text{m}$ Device 2: $t = 30 \text{ nm}$ $d = 8 \mu\text{m}$	Optical	-8 to 27	NA	Device 1: -6300 Device 2: -9500	NA
533–535	Molybdenum disulfide (MoS ₂)		$t = 56 \text{ nm}$ $d = 5 \mu\text{m}$	Optical	20.7–42.4	25.1	-3960	528
536	Hexagonal boron nitride (h-BN)		$t = 10 \text{ nm}$ $d = 10 \mu\text{m}$	Optical	-7 to 141	10.74	-1780	51
537	Bismuth oxyiodide (BiOI)		$d = 7 \mu\text{m}$	Optical	30–36	3.86	70 000	NA
538	Molybdenum disulfide (MoS ₂)		$d = 2 \mu\text{m}$	Electrical	27–107	59.2	-283	NA

nanoelectromechanical systems (NEMS) have been growing, and particularly, playing important roles in fundamental physics exploration, metrology and high-precision instruments, and quantum engineering.^{527,528} At these frontiers, NEMS enabled by low-dimensional advanced materials in special designs make essential mesoscopic transducers that can bridge the classical and quantum worlds. Earlier, 1D nanowire or nanobeam Si and SiC NEMS resonators have exhibited negative TC_f values of -40 to -60 ppm/K (in \sim 20–100 K range),^{529,530} similar to some of their conventional MEMS counterparts. More recently, 2D materials have gained significant attention thanks to their unique atomic-scale thickness, ultrahigh mechanical strain limit and strength, and widely tunable electronic and optical properties. These characteristics make them highly suitable for engineering new NEMS transducers, where minimizing device thickness (or optimizing size-to-thickness ratio) is essential for enhancing sensitivity and functionality. In 2D resonant NEMS, materials like graphene, MoS₂ and other transition metal dichalcogenides (TMDCs) exhibit remarkable mechanical and electronic properties, allowing for high-precision sensors and actuators in applications where ultimately small volumes and masses are desirable. One distinct feature of 2D material NEMS resonators is their pronounced responsivity and sensitivity to environmental factors, including pressure, mass, temperature, etc. Given their

extreme thinness and infinitesimal thermal mass, even small temperature variations can lead to noticeable shifts in their resonant frequencies. This temperature-dependent frequency shift, quantified as TC_f, is often much larger in 2D NEMS than in traditional, 3D bulky counterparts.

As summarized in Table V, large absolute TC_f values on the order of 10^3 – 10^4 ppm/°C have been measured from 2D NEMS resonators. The large TC_f makes 2D NEMS resonators ideal candidates for temperature sensing applications, where even minuscule changes in temperature can be detected by monitoring frequency shifts. 2D NEMS show exciting potential for infrared (IR) thermal sensing. This characteristic of ultrahigh TC_f makes them attractive for applications in areas like environmental monitoring, medical diagnostics, and advanced imaging systems, where detecting small temperature variations is crucial. However, studies on the TC_f for 2D NEMS at high temperatures are still very limited,^{539,540} and the stability and practicality of these devices under such conditions remain to be thoroughly evaluated. Meanwhile, challenges and opportunities exist in achieving scalability with high uniformity in device performance, arrayed optical/electrical characterization, and reliable integration and packaging. Encouragingly, it has been demonstrated recently that temperature compensation can be achieved in graphene 2D NEMS resonators, in

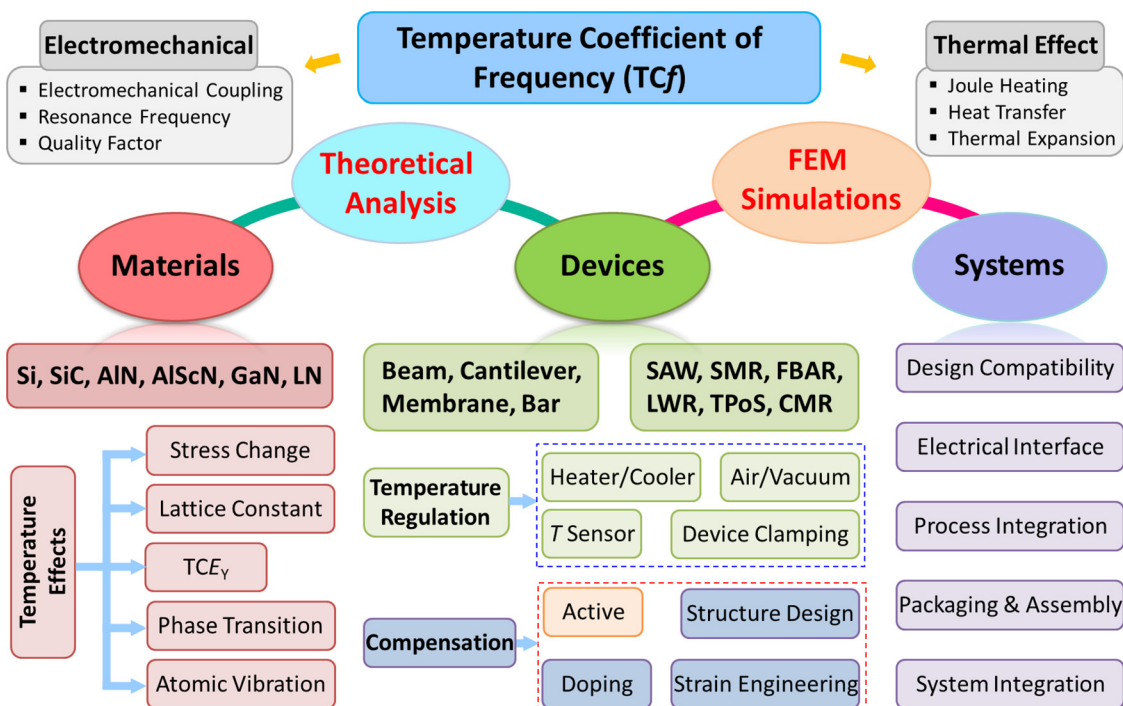


FIG. 37. Summary and outlook of the studies on temperature coefficient of frequency (TCf).

which the innate very high TCf values of ($\sim 10^3$ to 10^4 ppm/ $^\circ\text{C}$) can be very efficiently lowered down to ~ 10 to 10^2 of ppm/ $^\circ\text{C}$ levels, by exploiting the compensating thermal expansion effects between graphene resonators and their clamping electrodes.⁵³²

XV. SUMMARY AND OUTLOOK

Figure 37 shows an overview of the materials, device types, design considerations and system approaches in current state-of-the-art MEMS resonators. We discuss the individual areas as follows:

Materials. The investigation into the TCf of MEMS has encompassed a diverse range of materials, including Si, SiC, AlN, GaN, AlScN, LiNbO₃, etc. Si exhibits limitations in high-temperature applications due to its deteriorating electronic properties, whereas WBG materials, such as SiC, AlN, AlScN, and GaN, demonstrate remarkable performance at elevated temperatures and hold substantial potential for applications in harsh environments. However, MEMS based on these materials do not inherently possess zero TCf. To address this, intricate passive and/or active compensation techniques must be employed to counteract the temperature effects and strive toward achieving localized zero TCf. Developing a deep understanding of how material properties change with temperature is essential and extremely important for engineering the TCf of MEMS devices. Presently, there remains an incomplete understanding of the material properties concerning TCf, such as the TCE_Y and the stress evaluation with temperature, particularly due to the mismatch in the CTE and lattice constant at the interface between the functional layer and the substrate or within multilayer heterostructures. Additionally, the exploration of microscopic vibrations at the atomic level is relatively scarce, especially under varying temperatures, impeding a comprehensive

understanding of the TCf mechanisms. To advance in this field, it is imperative that further research efforts should be focused on bridging the aforementioned gaps. Through the explorations of material properties across wide temperature ranges, researchers can deepen their understanding of material behavior and pave the way for the development of innovative temperature compensation techniques or the engineering of TCf for sensing applications, particularly in high-temperature scenarios and harsh environments.

Devices. Extensive research has been conducted on TCf in a diverse range of MEMS structures, such as beam, cantilever, tuning fork, plate, disk, ring resonators, SAW, LWR, SMR, FABR, TPoS, CMR, etc. Among these, beam, cantilever, diaphragm, and membrane MEMS resonators have been extensively investigated across various materials thanks to their relative structural simplicity, making them well-suited for probing the mechanical properties of materials, such as E_Y and stress, through the measurement of resonance frequencies (can benefit from multimode resonances). For example, cantilever resonators demonstrate a direct dependence of resonance frequency on E_Y , enabling the exploration of TCE_Y through TCf measurement. Operating predominantly in the flexural mode, these MEMS resonators typically exhibit higher absolute TCf values compared to their BAW counterparts, thereby showcasing their potential for temperature sensing applications. SAW devices have garnered substantial attention owing to their straightforward fabrication processes, with operational frequencies predominantly below 4 GHz. Temperature compensation in SAW devices primarily involves fine-tuning the normalized thickness of the piezoelectric layer relative to the wavelength of the surface acoustic wave (h/λ), as well as tailoring the interface properties between the piezoelectric layer and the substrate. In recent years, LWR

devices have gained increasing attention and endeavor, pushing the frontiers with state-of-the-art frequencies surpassing 20 GHz. Furthermore, leveraging lithographic techniques allows for the realization of multi-frequency capabilities on a single chip through precise dimensional control. TC_f engineering in LWR devices is primarily accomplished by incorporating a SiO₂ layer at the bottom to achieve effective regulation. Compensating for the TC_f in SMRs presents technical challenges because of the presence of multiple materials with distinct properties in the stack. Many efforts have focused on optimizing the sequence and thicknesses of the stacking materials within the acoustic mirror to achieve effective TC_f compensation in SMRs.

Temperature regulation methods in controlling MEMS demonstrate considerable diversity. Factors such as the non-uniform temperature distribution of the heater, the method of attaching the device to the heater, and the surrounding environmental conditions (e.g., vacuum or air) during testing play a critical role in determining the TC_f accurately. These influential variables can introduce variations in temperature measurements for both the reference temperature sensor and the MEMS transducer, subsequently leading to deviations in frequency measurements. Discrepancies observed in reported TC_f values for similar structures of the same material across various literature sources can, in part, result from challenges associated with temperature regulation and measurement. Therefore, addressing and standardizing these factors is crucial. This ensures the reproducibility and comparability of TC_f, thereby facilitating advancements in device design and performance optimization.

Temperature compensation. Various temperature compensation methods have been explored; however, achieving precise control over the TC_f remains challenging. While these methods compensate for TC_f to some extent, attaining accurate control necessitates a comprehensive understanding of material properties and device physics. Passive compensation methods generally offer greater potential for practical applications compared to active methods, albeit with current limitations in adjustment accuracy. Strain engineering has emerged as a promising and effective approach for temperature compensation in MEMS devices. One strategy involves precise control of growth conditions during material deposition to manipulate film stress. Adjusting parameters such as growth temperature and deposition rate enables tailored stress engineering; however, careful consideration is needed to avoid excessive prestress that can compromise the structural integrity of suspended elements and lead to crack formation. Another approach focuses on modulating the interface stress by manipulating the thermal expansion and lattice constant through the introduction of buffer layers or appropriate substrate selection, thereby influencing the stress within the entire thin film stack. Post-fabrication stress adjustment can be achieved using external mechanical devices, allowing for dynamic control of strain. Integrating MEMS devices with flexible substrates represents an intriguing direction for strain engineering, offering enhanced design flexibility and expanded application possibilities. However, successful implementation of this approach still poses challenges that require further investigation and development.

Structure optimization. Structure optimization stands out as the predominant approach to passive temperature compensation in resonant MEMS. This strategy involves adjusting the thickness and sequence of materials within the stack layer, carefully selecting appropriate substrate materials, introducing SiO₂ layers, or incorporating embedded SiO₂ pillars in Si. While these methods offer partial

temperature compensation, a comprehensive understanding of the heat transfer and mechanical vibration characteristics at the device level is still lacking. Further analysis and evaluation of these structures are crucial for unraveling their intricate thermal and mechanical properties, thereby enhancing the efficacy of passive compensation techniques. Advancements in theoretical and experimental investigations of these structures will play a pivotal role in the development of more robust and precise temperature compensation approaches for MEMS transducers. Future research should focus on advancing passive compensation methods while capitalizing on the strengths of active compensation, ultimately realizing higher levels of accuracy in temperature compensation.

Theoretical modeling. An accurate theoretical model is crucial in guiding MEMS design. Currently, there is a well-established understanding of the theoretical analysis of mechanical properties in simple structures such as beams, cantilevers, plates, and membranes. They often involve simplified assumptions and mathematical equations, allowing for analytical expressions of key parameters such as displacement, frequency, and stress. However, the absence of models for complex structural devices and intricate boundary conditions is a significant limitation. FEM simulations utilize computational techniques to analyze complex geometries, material properties, and boundary conditions, which provide detailed and accurate insights into the mechanical behavior of MEMS, including the effects of temperature, stress distribution, and mode shapes. In the analysis and simulation of TC_f, it is essential to couple thermal effects alongside mechanical analysis. While some studies have explored the coupling of temperature field and mechanics, the complexity of TC_f has necessitated simplifications in terms of structural considerations and material property definitions. As a result, there are notable discrepancies between simulation and experimental results. Currently, there is a dearth of thermal models specifically tailored for various piezoelectric MEMS transducers. The absence of a comprehensive thermal transfer model within these devices, especially when influenced by external temperature profile, is a significant limitation. Moreover, insufficient research has been conducted to investigate how material interface properties impact heat transfer and subsequently affect the mechanical characteristics of the structural stack of the device. For instance, devices like SMRs with multi-layered structures present considerable challenges in terms of coupling temperature and mechanical fields. Addressing these issues requires prior understanding of the temperature variation characteristics of material properties.

System integration. System integration involves the harmonization of temperature compensation mechanisms with the overall system's requirements. Collaborative efforts from mechanical, electrical, and software engineering are crucial in devising a comprehensive compensation strategy. Calibration routines, feedback loops, and real-time monitoring systems can be integrated to continuously optimize TC_f compensation as the system operates under changing temperature conditions. In terms of design compatibility, precise TC_f compensation ensures that the resonator's frequency remains stable across varying temperatures, aligning with the system's intended functionality. This demands meticulous consideration of materials with low thermal expansion coefficients and an adaptable resonator geometry that counteracts temperature-induced shifts. Regarding electrical interface, temperature compensation involves intricate circuitry that dynamically adjusts the driving voltage or current to counteract TC_f variations.

Accurate compensation allows for reliable and consistent resonator behavior, ensuring the system's stability over its operational temperature range. This demands sophisticated analog and digital components that interface seamlessly with the resonator and maintain the desired frequency response. The fabrication process must incorporate techniques to control the material properties, dimensions, and stress gradients within the MEMS resonator. Precise process control helps minimize the impact of temperature on resonator behavior and optimizes the TCf compensation mechanism. Integrating temperature-sensitive elements within the MEMS structure, such as integrated heaters or temperature sensors, further enhances the compensation accuracy. Packaging and assembly also play a significant role in TCf compensation. The encapsulation of MEMS resonators within temperature-controlled environments or insulating packaging materials can significantly reduce the influence of external temperature variations. Moreover, precision assembly techniques ensure that the resonator's mechanical integrity is maintained, mitigating any unwanted frequency shifts during integration into the larger system. As technology advances, the synergy among these factors will continue to refine temperature compensation techniques, enabling MEMS resonators to fulfill their potential as essential components in diverse and growing arrays of applications.

ACKNOWLEDGMENTS

The authors are grateful for the financial support of the Defense Threat Reduction Agency (DTRA) (Award/Contract Number HDTRA1-19-1-0035), the Interaction of Ionizing Radiation with Matter University Research Alliance (Award/Contract Number HDTRA1-20-2-0002), the National Science Foundation (NSF) through the CCSS EAGER Program (Award/Contract Number ECCS-2221881), and the Air Force Office of Scientific Research (AFOSR) through the Basic Research Program (Award/Contract Number FA9550-23-1-0304). P.X.-L.F. acknowledges the support of the Defense Advanced Research Projects Agency (DARPA) OptIM Program (Award/Contract Number HR00112320028).

AUTHOR DECLARATIONS

Conflict of Interest

The authors have no conflicts to disclose.

Author Contributions

Wen Sui: Conceptualization (equal); Data curation (lead); Formal analysis (equal); Investigation (lead); Methodology (equal); Validation (equal); Writing – original draft (lead); Writing – review & editing (equal). **Stephen J. Pearton:** Conceptualization (equal); Data curation (supporting); Investigation (supporting); Resources (supporting); Validation (supporting); Writing – original draft (supporting); Writing – review & editing (supporting). **Philip X.-L. Feng:** Conceptualization (lead); Data curation (supporting); Formal analysis (equal); Funding acquisition (lead); Investigation (supporting); Methodology (equal); Project administration (lead); Resources (lead); Supervision (lead); Validation (equal); Writing – original draft (equal); Writing – review & editing (equal).

DATA AVAILABILITY

The data that support the findings of this study are available from the corresponding author upon reasonable request.

REFERENCES

- ¹S. Ba Hashwan, M. H. Khir, I. M. Nawi, M. R. Ahmad, M. Hanif, F. Zahoor, Y. Al-Douri, A. S. Algamili, U. I. Bature, S. S. Alabsi, M. O. Sabbea, and M. Junaid, *Discover Nano* **18**, 25 (2023).
- ²M. Sawane and M. Prasad, *Mater. Sci. Semicond.* **158**, 107324 (2023).
- ³A. Kumar, A. Varghese, G. Sharma, M. Kumar, G. K. Sharma, M. Prasad, V. Janyani, R. P. Yadav, and K. Elgaid, *Micro Nanostruct.* **179**, 207592 (2023).
- ⁴Z. Liu and F. Ayazi, *IEEE Trans. Ultrason. Ferroelectr. Freq. Control* **70**, 1172–1188 (2023).
- ⁵W. Sui, T. Kaisar, H. Wang, Y. Wu, J. Lee, H. Xie, and P. X.-L. Feng, *IEEE Sens. J.* **24**, 7273–7283 (2024).
- ⁶P. X.-L. Feng, D. J. Young, and C. A. Zorman, “MEMS/NEMS devices and applications,” in *Springer Handbook Nanotechnology*, edited by B. Bhushan (Springer, Berlin, Heidelberg, 2017).
- ⁷W. H. Lai, B. Li, S. H. Fu, and Y. S. Lin, *Micromachines* **14**, 169 (2023).
- ⁸C. He, S. Liu, G. Zhong, H. Wu, L. Cheng, J. Lin, and Q. Huang, *Micromachines* **14**, 130 (2023).
- ⁹H. C. Cheng, S. C. Liu, C. C. Hsu, H. Y. Lin, F. Shih, M. Wu, K. C. Liang, M. F. Lai, and W. Fang, *Sens. Actuators A: Phys.* **349**, 114010 (2023).
- ¹⁰F. Giacomozi, E. Proietti, G. Capoccia, G. M. Sardi, G. Bartolucci, J. Iannacci, G. Tagliapietra, B. Margesin, and R. Marcelli, *Sensors* **23**, 466 (2023).
- ¹¹W. Sui, S. M. E. H. Yousuf, Y. Liu, S. J. Pearton, and P. X.-L. Feng, *Adv. Mater. Technol.* **9**, 2301356 (2024).
- ¹²O. Solgaard, A. A. Godil, R. T. Howe, L. P. Lee, Y. A. Peter, and H. Zappe, *J. Microelectromech. Syst.* **23**, 517–538 (2014).
- ¹³R. Nathanael, V. Pott, H. Kam, J. Jeon, and T.-J. K. Liu, in *2009 IEEE International Electron Device Meeting (IEDM)*, Baltimore, MD, 7–9 December (IEEE, 2009), pp. 223–226.
- ¹⁴X. L. Feng, M. H. Matheny, C. A. Zorman, M. Mehregany, and M. L. Roukes, *Nano Lett.* **10**, 2891–2896 (2010).
- ¹⁵A. Yao and T. Hikihara, *Appl. Phys. Lett.* **105**, 123104 (2014).
- ¹⁶J. Yaung, L. Hutin, J. Jeon, and T.-J. K. Liu, *J. Microelectromech. Syst.* **23**, 198–203 (2014).
- ¹⁷L. Cao, S. Mantell, and D. Polla, *Sens. Actuators A: Phys.* **94**, 117–125 (2001).
- ¹⁸G. Kotzar, M. Freas, P. Abel, A. Fleischman, S. Roy, C. Zorman, J. M. Moran, and J. Melzak, *Biomaterials* **23**, 2737–2750 (2002).
- ¹⁹F. Pop, S. D. Calisgan, B. Herrera, A. Risso, S. Kang, V. Rajaram, Z. Qian, and M. Rinaldi, *IEEE Trans. Electron Devices* **69**, 1327–1332 (2022).
- ²⁰E. Pengwang, K. Rabenorosoa, M. Rakotondrabe, and N. Andreff, *Micromachines* **7**, 24 (2016).
- ²¹Y. Hasegawa, C. Shimohira, M. Matsushima, T. Sugiyama, T. Kawabe, and M. Shikida, *IEEE Trans. Electr. Electron. Eng.* **18**, 139–146 (2022).
- ²²H. R. Shea, *SPIE Proc.* **7928**, 96 (2011).
- ²³M. Numazawa, Y. Ezoe, K. Ishikawa, D. Ishi, A. Fukushima, S. Sakuda, T. Uchino, A. Inagaki, H. Morishita, Y. Ueda, T. Murakawa, L. Sekiguchi, Y. Tsuij, I. Mitsuishi, H. Nakajima, Y. Kanamori, K. Morishita, and K. Mitsuda, *Space Telescopes Instrum.* **12181**, 245–1380 (2022).
- ²⁴C. Rossi, T. D. Conto, D. Estève, and B. Larangot, *Smart Mater. Struct.* **10**, 1156 (2001).
- ²⁵S. Chen, Q. Zhao, and J. Cui, *IEEE Trans. Electron Devices* **69**, 5155–5161 (2022).
- ²⁶W. Sui, X.-Q. Zheng, J.-T. Lin, J. Lee, J. L. Davidson, R. A. Reed, R. D. Schrimpf, B. W. Alphenaar, M. L. Alles, and P. X.-L. Feng, *IEEE Trans. Nucl. Sci.* **69**, 216–224 (2022).
- ²⁷L. Wang, H. Liu, and X. Liu, *Micromachines* **13**, 743 (2022).
- ²⁸N. F. De Rooij, S. Gautsch, D. Briand, C. Marxer, G. Milet, W. Noell, H. Shea, U. Stauffer, and B. Van Der Schoot, in *Proceedings of International Conference on Solid-State Sensors, Actuators and Microsystems (Transducers)*, Denver, CO, 21–25 June (IEEE, 2009), pp. 17–24.

- ²⁹T. Marwan, A. Kechaf, A. Giani, P. Combette, G. Kock, C. Gauthier-Blum, and M Schneider, in *Symposium on Design, Test, Integration & Packaging of MEMS and MOEMS (DTIP)*, Paris, France, 12–15 May (IEEE, 2019), pp. 1–4.
- ³⁰C. Acar, A. R. Schofield, A. A. Trusov, L. E. Costlow, and A. M. Shkel, *IEEE Sens. J.* **9**, 1895–1906 (2009).
- ³¹P. Verma, D. Punetha, and S. K. Pandey, *Silicon* **12**, 2663–2671 (2020).
- ³²R. Alcesilas, P. Rey, C. Jouvaud, M. Sansa, J. C. Bastien, and C. Delaveaud, in *Proceedings of 2022 Smart Systems Integration (SSI)*, Grenoble, France, 27–28 April (IEEE, 2022), pp. 1–4.
- ³³C. Wu, X. Fang, Q. Kang, Z. Fang, J. Wu, H. He, D. Zhang, L. Zhao, B. Tian, and R. Maeda, *Microsyst. Nanoeng.* **9**, 41 (2023).
- ³⁴W. A. Gill, I. Howard, I. Mazhar, and K. McKee, *Sensors* **22**, 7405 (2022).
- ³⁵J. Mo, S. Shankar, G. Zhang, and S. Vollebregt, in *Proceedings of IEEE 36th International Conference on Micro Electro Mechanical Systems (MEMS)*, Munich, Germany, 15–19 January (IEEE, 2023), pp. 72–75.
- ³⁶B. Sun, J. Mo, H. Zhang, H. W. van Zeijl, W. D. van Driel, and G. Zhang, in *Proceedings of IEEE 36th International Conference on Micro Electro Mechanical Systems (MEMS)*, Munich, Germany, 15–19 January (IEEE, 2023), pp. 621–624.
- ³⁷J. Han, P. Cheng, H. Wang, C. Zhang, J. Zhang, Y. Wang, L. Duan, and G. Ding, *Mater. Lett.* **125**, 224–226 (2014).
- ³⁸A. Ghosh, C. Zhang, S. Q. Shi, and H. Zhang, *CLEAN—Soil, Air, Water* **47**, 1800491 (2019).
- ³⁹M. K. Dounkal, R. K. Bhan, and N. Kumar, *Microsyst. Technol.* **26**, 377–394 (2020).
- ⁴⁰A. Kourani, E. Hegazi, and Y. Ismail, *Microelectron. J.* **46**, 496–505 (2015).
- ⁴¹D. M. Tanner, *Microelectron. Reliab.* **49**, 937–940 (2009).
- ⁴²M. Hommel, H. Knab, and S. G. Yousef, *Microelectron. Reliab.* **126**, 114252 (2021).
- ⁴³W. Dong, S. Liu, S. J. Bae, and Y. Cao, *Reliab. Eng. Syst. Saf.* **205**, 107260 (2021).
- ⁴⁴X. Geng, P. Patel, and D. D. Meng, in *Proceedings of IEEE 23rd International Conference on Micro Electro Mechanical Systems (MEMS)*, Hong Kong, China, 24–28 January (IEEE, 2010), pp. 148–151.
- ⁴⁵M. A. R. Tahir, S. A. R. Bukhari, and M. M. Saleem, in *Proceedings of IEEE 23rd International Multitopic Conference (INMIC)*, Bahawalpur, Pakistan, 05–07 November (IEEE, 2020), pp. 1–6.
- ⁴⁶P. Mahanta, F. Anwar, and R. Coutou, *Sensors* **19**, 579 (2019).
- ⁴⁷Y. K. Kim, E. K. Kim, S. W. Kim, and B. K. Ju, *Sens. Actuators A Phys.* **143**, 323–328 (2008).
- ⁴⁸M. Mehregany and C. A. Zorman, *Thin Solid Films* **355–356**, 518–524 (1999).
- ⁴⁹W. Chen, W. Jia, Y. Xiao, Z. Feng, and G. Wu, *IEEE Electron Device Lett.* **42**, 1382–1385 (2021).
- ⁵⁰Y. Wang, R. Cao, C. Li, and R. N. Dean, *IEEE Sens. J.* **21**, 92–119 (2021).
- ⁵¹E. H. Amalu, N. Ekere, and R. Bhatti, in *Proceedings of IEEE 2nd International Conference on Adaptive Science & Technology (ICAST)*, Accra, Ghana, 14–16 January (IEEE, 2009), pp. 146–153.
- ⁵²H. Lee, A. Partridge, and F. Assaderaghi, in *Proceedings of IEEE International Frequency Control Symposium (IFCS)*, Baltimore, MD, USA, 21–24 May (IEEE, 2012), pp. 1–5.
- ⁵³X. Guo, Q. Xun, Z. Li, and S. Du, *Micromachines* **10**, 406 (2019).
- ⁵⁴L. F. Allard, W. C. Bigelow, M. Jose-Yacaman, D. P. Nackashi, J. Damiano, and S. E. Mick, *Microsc. Res. Technol.* **72**, 208–215 (2009).
- ⁵⁵V. Nerguzian and I. Stiharu, *SAE Trans.* **112**, 263–269 (2003), <http://www.jstor.org/stable/44699200>.
- ⁵⁶B. Kim, M. A. Hopcroft, R. N. Candler, C. M. Jha, M. Agarwal, R. Melamud, S. A. Chandorkar, G. Yama, and T. W. Kenny, *J. Microelectromech. Syst.* **17**, 755–766 (2008).
- ⁵⁷L. Lin, *Microelectron. J.* **34**, 179–185 (2003).
- ⁵⁸D. L. DeVoe, *IEEE Trans. Compon. Packag. Manuf. Technol.* **25**, 576–583 (2002).
- ⁵⁹W. N. Sharpe, *Appl. Mech. Mater.* **3**, 59–64 (2006).
- ⁶⁰A. Witvrouw, H. A. C. Tilmans, and I. D. Wolf, *Microelectron. Eng.* **76**, 245–257 (2004).
- ⁶¹J. A. Krogstad, C. Keimel, and K. J. Hemker, *J. Mater. Res.* **29**, 1597–1608 (2014).
- ⁶²C. C. Chen, H. T. Yu, G. H. Li, and S. S. Li, in *Proceedings of 26th IEEE International Conference on Micro Electro Mechanical Systems (MEMS)*, Taipei, Taiwan, 20–24 January (IEEE, 2013), pp. 765–768.
- ⁶³M. Goel, *Curr. Sci.* **85**, 443–453 (2003), <http://www.jstor.org/stable/24108537>.
- ⁶⁴W. Sui, X.-Q. Zheng, J.-T. Lin, B. W. Alphenaar, and P. X.-L. Feng, *J. Microelectromech. Syst.* **30**, 521–529 (2021).
- ⁶⁵N. Marsi, B. Y. Majlis, A. A. Hamzah, and F. Mohd-Yasin, *Energy Procedia* **68**, 471–479 (2015).
- ⁶⁶C. S. Fuller and R. A. Logan, *J. Appl. Phys.* **28**, 1427–1436 (1957).
- ⁶⁷P. W. Chapman, O. N. Tufte, J. D. Zook, and D. Long, *J. Appl. Phys.* **34**, 3291–3295 (1963).
- ⁶⁸J. P. Dismukes, L. Ekstrom, E. F. Steigemeier, I. Kudman, and D. S. Beers, *J. Appl. Phys.* **35**, 2899–2907 (1964).
- ⁶⁹K. Tonisch, V. Cimalla, C. Foerster, H. Romanus, O. Ambacher, and D. Dontsov, *Sens. Actuator A Phys.* **132**, 658–663 (2006).
- ⁷⁰Y. Guo, H. Zhu, and Q. Wang, *ACS Appl. Mater. Interfaces* **11**, 1033–1039 (2019).
- ⁷¹V. Cimalla, J. Pezoldt, and O. Ambacher, *J. Phys. D: Appl. Phys.* **40**, S19 (2007).
- ⁷²P. Wang, D. Wang, S. Mondal, and Z. Mi, in *Proceedings of Device Research Conference (DRC)*, Columbus, OH, USA, 26–29 June (IEEE, 2022), pp. 1–2.
- ⁷³B. Uppalapati, D. Gajula, F. Bayram, A. Kota, A. Gunn, D. Khan, V. P. Chodavarapu, and G. Koley, *ACS Photonics* **9**, 1908–1918 (2022).
- ⁷⁴P. Leclaire, E. Frayssinet, C. Morelle, Y. Cordier, D. Theron, and M. Faucher, *J. Micromech. Microeng.* **26**, 105015 (2016).
- ⁷⁵K. Brueckner, F. Niebelshuetz, K. Tonisch, C. Foerster, V. Cimalla, R. Stephan, J. Pezoldt, T. Stauden, O. Ambacher, and M. Hein, *Phys. Status Solidi A* **208**, 357–376 (2011).
- ⁷⁶G. Vanko, P. Hudek, J. Zehetner, J. Dzuba, P. Choleva, V. Kutiš, M. Vallo, I. Rýger, and T. Lalinský, *Microelectron. Eng.* **110**, 260–264 (2013).
- ⁷⁷L. Wang, Y. Zhao, Y. Yang, X. Pang, L. Hao, Y. Zhao, and J. Liu, *IEEE Trans. Electron Devices* **69**, 2009–2014 (2022).
- ⁷⁸P. Moll, G. Pfusterschmid, and U. Schmid, in *Proceedings of 36th IEEE International Conference on Micro Electro Mechanical Systems (MEMS)*, Munich, Germany, 15–19 January (IEEE, 2023), pp. 590–593.
- ⁷⁹F. La Via, D. Alquier, F. Giannazzo, T. Kimoto, P. Neudeck, H. Ou, A. Roncaglia, S. E. Saddow, and S. Tudisco, *Micromachines* **14**, 1200 (2023).
- ⁸⁰K. Jonnalagadda, S. W. Cho, I. Chasiotis, T. Friedmann, and J. Sullivan, *J. Mech. Phys. Solids* **56**, 388–401 (2008).
- ⁸¹E. Peiner, A. Tibrewala, R. Bandorf, H. Lüthje, L. Doering, and W. Limmer, *J. Micromech. Microeng.* **17**, S83 (2007).
- ⁸²J. K. Luo, Y. Q. Fu, H. R. Le, J. A. Williams, S. M. Spearing, and W. I. Milne, *J. Micromech. Microeng.* **17**, S147 (2007).
- ⁸³H. Sun, L. Yang, H. Wu, and L. Zhao, *Lubricants* **11**, 186 (2023).
- ⁸⁴O. Ambacher, *J. Phys. D: Appl. Phys.* **31**, 2653–2710 (1998).
- ⁸⁵S. P. DenBaars, D. Feezell, K. Kelchner, S. Pimpuktar, C. C. Pan, C. C. Yen, S. Tanaka, Y. Zhao, N. Pfaff, R. Farrell, M. Iza, S. Keller, U. Mishra, J. S. Speck, and S. Nakamura, *Acta Mater.* **61**, 945–951 (2013).
- ⁸⁶M. Faucher, B. Grimbert, Y. Cordier, N. Baron, A. Wilk, H. Lahreche, P. Bove, M. François, P. Tilmant, T. Gehin, C. Legrand, M. Werquin, L. Bouchaillet, C. Gaquière, and D. Théron, *Appl. Phys. Lett.* **94**, 233506 (2009).
- ⁸⁷T. Zimmermann, M. Neuburger, P. Benkart, F. J. Hernandez-Guillen, C. Pietzka, M. Kunze, I. Daumiller, A. Dadgar, A. Krost, and E. Kohn, *IEEE Electron Device Lett.* **27**, 309–312 (2006).
- ⁸⁸A. Hassan, Y. Savaria, and M. Sawan, *IEEE Access* **6**, 78790–78802 (2018).
- ⁸⁹S. Faramehr, N. Jankovic, and P. Igic, in *Proceedings of 20th IEEE International Conference on Solid-State Sensors, Actuators and Microsystems & EuroSensors XXXIII (Transducers'19 & EuroSensors XXXIII)*, Berlin, Germany, 23–27 June (IEEE, 2019), pp. 1985–1988.
- ⁹⁰T. Feng, Q. Yuan, D. Yu, B. Wu, and H. Wang, *Micromachines* **13**, 2195 (2022).
- ⁹¹V. Zega, A. Opreni, G. Mussi, H. K. Kwon, G. Vukasin, G. Gattere, G. Langfelder, A. Frangi, and T. W. Kenny, in *Proceedings of 33rd IEEE International Conference on Micro Electro Mechanical Systems (MEMS)*, Vancouver, BC, Canada, 18–22 January (IEEE, 2020), pp. 1207–1210.
- ⁹²S. J. Suresha, M. Haj-Taieb, K. Bade, J. Aktaa, and K. J. Hemker, *Scr. Mater.* **63**, 1141–1144 (2010).
- ⁹³S. Sonmezoglu, S. E. Alper, and T. Akin, in *Proceedings of 17th IEEE International Conference on Solid-State Sensors, Actuators and Microsystems (TRANSDUCERS & EUROSENSORS XXVII)*, Barcelona, Spain, 16–20 June (IEEE, 2013), pp. 2519–2522.

- ⁹⁴B. Kim, R. N. Candler, M. A. Hopcroft, M. Agarwal, W. T. Park, and T. W. Kenny, *Sens. Actuator A Phys.* **136**, 125–131 (2007).
- ⁹⁵V. Kaajakari, A. Pangaro, Y. Goto, T. Nishimura, T. Okawa, H. Seki, A. Suzuki, and K. Umeda, in *Proceedings of Joint Conference of IEEE IEEE International Frequency Control Symposium & European Frequency and Time Forum (EFTF/IFC)*, Orlando, FL, USA, 14–18 April (IEEE, 2012), pp. 1–5.
- ⁹⁶X. Zou, S. Ahmed, N. Jaber, and H. Fariborzi, in *Proceedings of 21st IEEE International Conference on Solid-State Sensors, Actuators and Microsystems (Transducers)*, Orlando, FL, USA, 20–24 June (IEEE, 2021), pp. 1239–1242.
- ⁹⁷W. C. Chen, M. H. Li, Y. C. Liu, W. Fang, and S. S. Li, *IEEE Electron Device Lett.* **33**, 721–723 (2012).
- ⁹⁸G. Mussi, M. Bestetti, V. Zega, A. A. Frangi, G. Gattere, and G. Langfelder, *IEEE Trans. Ind. Electron.* **67**, 6996–7004 (2020).
- ⁹⁹H. K. Kwon, G. D. Vukasin, N. E. Bousse, and T. W. Kenny, *J. Microelectromech. Syst.* **29**, 1130–1131 (2020).
- ¹⁰⁰A. R. Kolahdouz-Moghaddam, S. Nabavi, and F. Nabki, *J. Microelectromech. Syst.* **23**, 314–326 (2023).
- ¹⁰¹H. Zhu, C. Tu, and J. Y. Lee, in *Proceedings of 26th IEEE International Conference on Micro Electro Mechanical Systems (MEMS)*, Taipei, Taiwan, 20–24 January (IEEE, 2013), pp. 757–760.
- ¹⁰²W. Jia, W. Chen, Y. Xiao, Z. Wu, and G. Wu, *IEEE Trans. Electron Devices* **69**, 2597–2603 (2022).
- ¹⁰³C. Y. Liu, M. H. Li, C. Y. Chen, and S. S. Li, in *Proceedings of IEEE International Frequency Control Symposium (IFCS)*, New Orleans, LA, USA, 09–12 May (IEEE, 2016), pp. 1–3.
- ¹⁰⁴W. C. Chen, W. Fang, and S. S. Li, *J. Micromech. Microeng.* **21**, 065012 (2011).
- ¹⁰⁵E. J. Ng, C. H. Ahn, Y. Yang, V. A. Hong, C. F. Chiang, E. Ahadi, M. Ward, and T. W. Kenny, in *Proceedings of 17th IEEE International Conference on Solid-State Sensors, Actuators and Microsystems (TRANSDUCERS & EUROSENSORS XXVII)*, Barcelona, Spain, 16–20 June (IEEE, 2013), pp. 2419–2422.
- ¹⁰⁶T. Kose, K. Azgin, and T. Akin, in *Proceedings of IEEE International Symposium on Inertial Sensors and Systems*, Laguna Beach, CA, USA, 22–25 February (IEEE, 2016), pp. 33–36.
- ¹⁰⁷W. T. Hsu and M. Pai, in *Proceedings of 57th Electronic Components and Technology Conference*, Sparks, NV, USA, 29 May–01 June (IEEE, 2007), pp. 1895–1899.
- ¹⁰⁸M. T. Jan, F. Ahmad, N. H. Hamid, M. H. Md Khir, K. Ashraf, and M. Shoaib, *Microelectron. Reliab.* **57**, 64–70 (2016).
- ¹⁰⁹G. Zhang, J. Ding, W. Xu, Y. Liu, R. Wang, J. Han, B. Bai, C. Xue, J. Liu, and W. Zhang, *Mech. Syst. Signal Process.* **104**, 607–618 (2018).
- ¹¹⁰X. Shen, K. Wu, H. Sun, L. Sang, Z. Huang, M. Imura, Y. Koide, S. Koizumi, and M. Liao, *Diam. Relat. Mater.* **116**, 108403 (2021).
- ¹¹¹P. R. Cantwell, H. Kim, M. M. Schneider, H. H. Hsu, D. Peroulis, E. A. Stach, and A. Strachan, *J. Microelectromech. Syst.* **21**, 840–849 (2012).
- ¹¹²A. Ben Amar, M. Faucher, V. Brandli, Y. Cordier, and D. Théron, *Phys. Status Solidi A* **211**, 1655–1659 (2014).
- ¹¹³X.-Q. Zheng and P. X.-L. Feng, in *Proceedings of IEEE 34th IEEE International Conference on Micro Electro Mechanical Systems (MEMS)*, Gainesville, FL, USA, 25–29 January (IEEE, 2021), pp. 165–167.
- ¹¹⁴S. Dutta, M. Imran, R. Pal, K. K. Jain, and R. Chatterjee, *Microsyst. Technol.* **17**, 1739–1745 (2011).
- ¹¹⁵S. Dutta and A. Pandey, *J. Mater. Sci. Mater. Electron.* **32**, 6705–6741 (2021).
- ¹¹⁶A. K. Pandey, K. Venkatesh, and R. Pratap, *Sadhana* **34**, 651–661 (2009).
- ¹¹⁷Samridhi, M. Kumar, S. Dhariwal, K. Singh, and P. Alvi, *Int. J. Mod. Phys. B* **33**, 1950040 (2019).
- ¹¹⁸A. Ballestra, A. Soma, and R. Pavanello, *Sensors* **8**, 767–783 (2008).
- ¹¹⁹A. Soma and A. Ballestra, *J. Micromech. Microeng.* **19**, 095023 (2009).
- ¹²⁰Y. Cao, D. Torres, T. Wang, X. Tan, and N. Sepúlveda, *Smart Mater. Struct.* **26**, 085032 (2017).
- ¹²¹G. Hummel, Y. Hui, Z. Qian, and M. Rinaldi, in *Proceedings of International Conference on Solid-State Sensors, Actuators, and Microsystems Workshop (IEEE, 2014)*, pp. 431–434. https://transducer-research-foundation.org/technical_digests/HiltonHead_2014/hh2014_0431.pdf.
- ¹²²G. Hummel, Y. Hui, and M. Rinaldi, in *Proceedings of IEEE International Frequency Control Symposium (IFCS)*, Taipei, Taiwan, 19–22 May (IEEE, 2014), pp. 1–3.
- ¹²³G. Hummel, Y. Hui, and M. Rinaldi, *J. Microelectromech. Syst.* **24**, 2145–2151 (2015).
- ¹²⁴M. M. Howlader, F. Zhang, and M. J. Kim, *J. Microelectromech. Syst.* **20**, 17–20 (2010).
- ¹²⁵V. K. Khanna, *J. Phys. D: Appl. Phys.* **44**, 034004 (2011).
- ¹²⁶K. Komvopoulos, *Wear* **200**, 305–327 (1996).
- ¹²⁷H. Kahn, A. Avishai, R. Ballarini, and A. Heuer, *Scr. Mater.* **59**, 912–915 (2008).
- ¹²⁸Y. Huang, A. S. S. Vasan, R. Doraiswami, M. Osterman, and M. Pecht, *IEEE Trans. Device Mater. Reliab.* **12**, 482–493 (2012).
- ¹²⁹S. M. Allameh, P. Shrotriya, A. Butterwick, S. B. Brown, and W. O. Soboyejo, *J. Microelectromech. Syst.* **12**, 313–324 (2003).
- ¹³⁰Z. Djurić, O. Jakšić, and D. Randjelović, *Sens. Actuator A Phys.* **96**, 244–251 (2002).
- ¹³¹M. Bharati, L. Rana, R. Gupta, A. Sharma, P. K. Jha, and M. Tomar, *Anal. Chim. Acta* **1249**, 340929 (2023).
- ¹³²P. O. Theillet and O. N. Pierron, *Sens. Actuator A Phys.* **171**, 375–380 (2011).
- ¹³³J. O. Dennis, A. Y. Ahmed, M. M. Khir, and A. Rabih, *Appl. Math. Infor. Sci.* **9**, 729–737 (2015).
- ¹³⁴I. Jokić, M. Frantović, and Z. Djurić, in *Proceedings of 29th International Conference on Microelectronics (MIEL)*, Belgrade, Serbia, 12–14 May (IEEE, 2014), pp. 117–124.
- ¹³⁵L. Mele, F. Santagata, E. Iervolino, M. Mihailovic, T. Rossi, A. Tran, H. Schellevis, J. Creemer, and P. Sarro, *Sens. Actuator A Phys.* **188**, 173–180 (2012).
- ¹³⁶S. M. Spearing, *Acta Mater.* **48**, 179–196 (2000).
- ¹³⁷H. Tada, A. E. Kumpel, R. E. Lathrop, J. B. Slanina, P. Nieva, P. Zavracky, IN. Miaoulis, and P. Y. Wong, *J. Appl. Phys.* **87**, 4189–4193 (2000).
- ¹³⁸C. L. Cheng, M. H. Tsai, and W. Fang, *J. Micromech. Microeng.* **25**, 025014 (2015).
- ¹³⁹V. Lehmann, in *Proceedings of 9th International Workshop on Micro Electromechanical Systems*, San Diego, CA, USA, 11–15 February (IEEE, 1996), pp. 1–6.
- ¹⁴⁰J. Spannhake, O. Schulz, A. Helwig, A. Krenkow, G. Müller, and T. Doll, *Sensors* **6**, 405–419 (2006).
- ¹⁴¹P. L. Neumann, J. Radó, J. M. Bozorádi, and J. Volk, *Micro Nano Eng.* **19**, 100198 (2023).
- ¹⁴²M. Yuan, J. Niroula, Q. Xie, N. S. Rajput, K. Fu, S. Luo, S. K. Das, A. J. B. Iqbal, B. Sikder, and M. F. Isamotu, *IEEE Electron Device Lett.* **44**, 1068–1071 (2023).
- ¹⁴³Y. Enns, A. Kazakin, A. Mizerov, K. Shubina, I. Morozov, D. Mokhov, and A. Bouravleuv, *Proc. J. Phys.: Conf. Ser.* **1695**, 012019 (2020).
- ¹⁴⁴L. Sang, M. Liao, X. Yang, H. Sun, J. Zhang, M. Sumiya, and B. Shen, *Sci. Technol. Adv. Mater.* **21**, 515–523 (2020).
- ¹⁴⁵I. Ahmed, U. Rawat, J. T. Chen, and D. Weinstein, *IEEE Trans. Ultrason. Ferroelectr. Freq. Control* **70**, 291–301 (2023).
- ¹⁴⁶W. Sui, X.-Q. Zheng, J.-T. Lin, B. W. Alphenaar, and P. X.-L. Feng, in *Proceedings of IEEE 34th IEEE International Conference on Micro Electro Mechanical Systems (MEMS)*, Gainesville, FL, USA, 25–29 January (IEEE, 2021), pp. 478–481.
- ¹⁴⁷G. Rezazadeh, A. Keyvani, and S. Jafarmadar, *Measurement* **45**, 580–589 (2012).
- ¹⁴⁸D. C. Abeyasinghe, S. Dasgupta, H. E. Jackson, and J. T. Boyd, *J. Micromech. Microeng.* **12**, 229 (2002).
- ¹⁴⁹H. Campanella, M. Narducci, S. Merugu, and N. Singh, *IEEE Trans. Electron Devices* **64**, 3368–3376 (2017).
- ¹⁵⁰C. Y. Lee and G. B. Lee, in *Proceedings of SENSORS*, Toronto, ON, Canada, 22–24 October (IEEE, 2003), pp. 384–388.
- ¹⁵¹A. S. Algarni, M. H. Khir, A. Y. Ahmed, A. A. Rabih, S. S. Ba-Hashwan, S. S. Alabsi, O. L. Al-Mahdi, U. B. Isyaku, M. G. Ahmed, and M. Junaid, *Micromachines* **13**, 525 (2022).
- ¹⁵²A. Uranga, J. Verd, and N. Barniol, “CMOS-MEMS resonators: From devices to applications,” *Microelectron. Eng.* **132**, 58–73 (2015).
- ¹⁵³L. C. Ortiz, H.-K. Kwon, J. Rodriguez, Y. Chen, G. D. Vukasin, D. B. Heinz, D. D. Shin, and T. W. Kenny, *J. Microelectromech. Syst.* **29**, 190–201 (2020).
- ¹⁵⁴C. T.-C. Nguyen, *IEEE Trans. Ultrason. Ferroelectr. Freq. Control* **54**, 251–270 (2007).
- ¹⁵⁵E. Ng, Y. Yang, V. Hong, C. Ahn, D. Heinz, I. Flader, Y. Chen, C. Everhart, B. Kim, and R. Melamud, in *Proceedings of 28th EEE International Conference on*

- Micro Electro Mechanical Systems (MEMS)*, Estoril, Portugal, 18–22 January (IEEE, 2015), pp. 1–2.
- ¹⁵⁶W.-T. Hsu, in *Proceedings of IEEE MTT-S International Microwave Symposium Digest*, San Francisco, CA, USA, 11–16 June (IEEE, 2006), pp. 672–675.
- ¹⁵⁷D. E. Serrano, M. F. Zaman, A. Rahafrooz, P. Hrudey, R. Lipka, D. Younkin, S. Nagpal, I. Jafri, and F. Ayazi, *Microsyst. Nanoeng.* **2**, 1–10 (2016).
- ¹⁵⁸B. W. Chui, Y. Hishinuma, R. Budakian, H. J. Mamin, T. W. Kenny, and D. Rugar, in *Proceedings of 12nd International Conference on Solid-State Sensors, Actuators and Microsystems (Transducers'03)*, Boston, MA, USA 8–12 June (IEEE, 2003), pp. 1120–1123.
- ¹⁵⁹S. C. Lin, B. S. Lee, W. J. Wu, and C. K. Lee, in *Proceedings of IEEE International Ultrasonic Symposium (IUS)*, Rome, Italy, 20–23 September (IEEE, 2009), pp. 755–758.
- ¹⁶⁰Z. Qian, Y. Hui, F. Liu, S. Kang, S. Kar, and M. Rinaldi, *Microsyst. Nanoeng.* **2**, 1–7 (2016).
- ¹⁶¹J. E.-Y. Lee and A. A. Seshia, *Sens. Actuator A Phys.* **167**, 237–244 (2011).
- ¹⁶²E. Colinet, J. Arcamone, A. Niel, E. Lorent, S. Hentz, and E. Ollier, in *Proceedings of 2010 IEEE International Frequency Control Symposium (IFCS)*, Newport Beach, CA, USA, 01–04 June (IEEE, 2010), pp. 174–178.
- ¹⁶³H. Y. Chen, S. S. Li, and M. H. Li, *IEEE Electron Device Lett.* **42**, 1045–1048 (2021).
- ¹⁶⁴F. M. Alsaeem, M. I. Younis, and L. Ruzziconi, *J. Microelectromech. Syst.* **19**, 794–806 (2010).
- ¹⁶⁵A. T. Lin, J. E. Lee, J. Yan, and A. A. Seshia, in *Proceedings of IEEE International Conference on Solid-State Sensors, Actuators and Microsystems (Transducers)*, Denver, CO, USA, 21–25 June (IEEE, 2009), pp. 561–564.
- ¹⁶⁶G. Piazza, P. J. Stephanou, and A. P. Pisano, *Solid-State Electron.* **51**, 1596–1608 (2007).
- ¹⁶⁷R. Lu, M. H. Li, Y. Yang, T. Manzaneque, and S. Gong, *J. Microelectromech. Syst.* **28**, 209 (2019).
- ¹⁶⁸H. Zhu and J. E. Y. Lee, in *Proceedings of 28th IEEE International Conference on Micro Electro Mechanical Systems (MEMS)*, Estoril, Portugal, 18–22 January (IEEE, 2015), pp. 797–800.
- ¹⁶⁹J. Li, Z. Chen, W. Liu, J. Yang, Y. Zhu, and F. Yang, *J. Micromech. Microeng.* **32**, 035002 (2022).
- ¹⁷⁰T. L. Naing, T. O. Rocheleau, E. Alon, and C. T.-C. Nguyen, *IEEE Trans. Ultrason. Ferroelectr. Freq. Control* **67**, 1377–1391 (2020).
- ¹⁷¹S. Ghasemi, S. Afrang, G. Rezazadeh, S. Darbasi, and B. Sotoudeh, *Microsyst. Technol.* **26**, 2389–2398 (2020).
- ¹⁷²J. Han, Y. Xiao, W. Chen, W. Jia, K. Zhu, and G. Wu, *J. Microelectromech. Syst.* **31**, 723–725 (2022).
- ¹⁷³Y. W. Lin, S. S. Li, Y. Xie, Z. Ren, and C. T.-C. Nguyen, in *Proceedings of IEEE International Frequency Control Symposium and Exposition*, Vancouver, BC, 29–31 August (IEEE, 2005), pp. 128–134.
- ¹⁷⁴J. Toledo, V. Ruiz-Díez, M. Bertke, H. Suryo Wasisto, E. Peiner, and J. L. Sánchez-Rojas, *Micromachines* **10**, 145 (2019).
- ¹⁷⁵H. Fatemi, M. J. Modarres-Zadeh, and R. Abdolvand, in *Proceedings of 28th IEEE International Conference on Micro Electro Mechanical Systems (MEMS)*, Estoril, Portugal, 18–22 January (IEEE, 2015), pp. 909–912.
- ¹⁷⁶J. Lu, T. Sagawa, L. Zhang, H. Takagi, D. F. Wang, T. Itoh, and R. Maeda, in *Proceedings of 8th Annual IEEE International Conference on Nano/Micro Engineered and Molecular Systems*, Suzhou, China, 07–10 April (IEEE, 2013), pp. 163–166.
- ¹⁷⁷S. A. K. M. Tadigadapa and K. Mateti, *Meas. Sci. Technol.* **20**, 092001 (2009).
- ¹⁷⁸C. Xu, J. Segovia-Fernandez, H. J. Kim, and G. Piazza, *J. Microelectromech. Syst.* **26**, 187–195 (2016).
- ¹⁷⁹G. Pillai and S. S. Li, *IEEE Sens. J.* **21**, 12589–12605 (2020).
- ¹⁸⁰T. Zhang, C. Guo, Z. Jiang, and X. Wei, *J. Appl. Phys.* **126**, 164506 (2019).
- ¹⁸¹D. Platz and U. Schmid, *J. Micromech. Microeng.* **29**, 123001 (2019).
- ¹⁸²M. T. Phan, X. T. Trinh, Q. C. Le, V. K. T. Ngo, and C. T.-C. Nguyen, *Sens. Imaging* **22**, 6 (2021).
- ¹⁸³A. Mustafazade, M. Pandit, C. Zhao, G. Sobreviela, Z. Du, P. Steinmann, X. Zou, R. T. Howe, and A. A. Seshia, *Sci. Rep.* **10**, 10415 (2020).
- ¹⁸⁴Y. Yuan, Q. Yang, H. Li, S. Shi, P. Niu, C. Sun, B. Liu, M. Zhang, and W. Pang, *J. Micromech. Microeng.* **33**, 085009 (2023).
- ¹⁸⁵Y. Zhang, Y. Yoshioka, M. Iimori, B. Qiu, X. Liu, and K. Hirakawa, *Appl. Phys. Lett.* **119**, 163503 (2021).
- ¹⁸⁶B. Qiu, Y. Zhang, K. Akahane, N. Nagai, and K. Hirakawa, *Appl. Phys. Lett.* **117**, 203503 (2020).
- ¹⁸⁷T. Ozaki, N. Ohta, and M. Fujiyoshi, *J. Micromech. Microeng.* **32**, 097001 (2022).
- ¹⁸⁸C. Li, B. Qiu, Y. Yoshioka, K. Hirakawa, and Y. Zhang, *Phys. Rev. Appl.* **19**, 024025 (2023).
- ¹⁸⁹D. I. Caruntu and R. Oyervides, *Int. J. Non-Linear Mech.* **149**, 104310 (2023).
- ¹⁹⁰D. I. Caruntu, M. A. Botello, C. A. Reyes, and J. S. Beatriz, *J. Comput. Nonlinear Dyn.* **14**, 031005 (2019).
- ¹⁹¹A. Deshmukh and V. K. Rao, *Eng. Res. Express* **4**, 035020 (2022).
- ¹⁹²Q. C. Le, M. T. Phan, X. T. Trinh, H. L. Truong, V. K. T. Ngo, and C. C. Nguyen, *Sens. Imaging* **22**, 36 (2021).
- ¹⁹³A. Setiono, M. Fahrbach, A. Deutschinger, E. J. Fantner, C. H. Schwalb, I. Syamsu, H. S. Wasisto, and E. Peiner, *Sensors* **21**, 4088 (2021).
- ¹⁹⁴J. E. Y. Lee, B. Bahreyni, and A. A. Seshia, *Sens. Actuator A Phys.* **148**, 395–400 (2008).
- ¹⁹⁵J. Wang, C. Zhao, G. Zhao, X. Jin, S. Zhang, and J. Zou, *Procedia Eng.* **120**, 857–860 (2015).
- ¹⁹⁶D. Han, J. Wang, S. Yuan, T. Yang, B. Chen, G. Teng, W. Luo, Y. Chen, Y. Li, and M. Wang, in *Proceedings of 20th International Conference on Solid-State Sensors, Actuators and Microsystems & Eurosensors XXXIII (TRANSDUCERS & EUROSENSORS XXXIII)*, Berlin, Germany, 23–27 June (IEEE, 2019), pp. 2061–2064.
- ¹⁹⁷J. Liang, Y. Chai, G. Meng, and X. Chen, *Micro Nano Lett.* **8**, 52–55 (2013).
- ¹⁹⁸W. Zhang, H. Zhu, and J. E. Y. Lee, *IEEE Trans. Electron Devices* **62**, 1596–1602 (2015).
- ¹⁹⁹E. E. Moreira, B. Kuhlmann, J. Gaspar, and L. A. Rocha, in *Proceedings of 20th International Conference on Solid-State Sensors, Actuators and Microsystems & Eurosensors XXXIII (TRANSDUCERS & EUROSENSORS XXXIII)*, Berlin, Germany, 23–27 June (IEEE, 2019), pp. 602–605.
- ²⁰⁰M. C. M. Lee and M. C. Wu, in *Proceedings of IEEE/LEOS International Conference on Optical MEMS (MEMS)*, Waikoloa, HI, USA, 18–21 August (IEEE, 2003), pp. 28–29.
- ²⁰¹M. C. M. Lee and M. C. Wu, *IEEE Photonics Technol. Lett.* **17**, 1034–1036 (2005).
- ²⁰²M. C. M. Lee and M. C. Wu, *Opt. Express* **14**, 4703–4712 (2006).
- ²⁰³D. Xia, L. Huang, and L. Zhao, *Sensors* **19**, 2798 (2019).
- ²⁰⁴A. Kanj, P. Ferrari, A. M. van der Zande, A. F. Vakakis, and S. Tawfick, *Mech. Syst. Signal Process.* **196**, 110331 (2023).
- ²⁰⁵P. Ullmann, C. Brethauer, M. Schneider, and U. Schmid, *Sens. Actuator A Phys.* **349**, 114003 (2023).
- ²⁰⁶J. E. Graebner, B. P. Barber, P. L. Gammel, D. S. Greywall, and S. Gopani, *Appl. Phys. Lett.* **78**, 159–161 (2001).
- ²⁰⁷J. Lee, Z. Wang, K. He, J. Shan, and P. X.-L. Feng, *Appl. Phys. Lett.* **105**, 023104 (2014).
- ²⁰⁸D. R. Southworth, H. G. Craighead, and J. Parpia, *Appl. Phys. Lett.* **94**, 213506 (2009).
- ²⁰⁹H. Schlicke, C. J. Schröter, and T. Vossmeyer, *Nanoscale* **8**, 15880–15887 (2016).
- ²¹⁰M. Park and A. Ansari, *J. Microelectromech. Syst.* **28**, 429–431 (2019).
- ²¹¹J. B. Messaoud, J. F. Michaud, D. Certon, M. Camarda, N. Piluso, L. Colin, F. Barcella, and D. Alquier, *Micromachines* **10**, 801 (2019).
- ²¹²X. C. Zhang, E. B. Myers, J. E. Sader, and M. L. Roukes, *Nano Lett.* **13**, 1528–1534 (2013).
- ²¹³B. Gadhavi, F. Golnaraghi, and B. Bahreyni, *Sensors* **22**, 7889 (2022).
- ²¹⁴L. Zhao, Y. Hu, T. Wang, J. Ding, X. Liu, Y. Zhao, and Z. Jiang, *Sensors* **16**, 830 (2016).
- ²¹⁵R. M. White and F. W. Voltmer, *Appl. Phys. Lett.* **7**, 314–316 (1965).
- ²¹⁶D. T. Bell and R. C. Li, *Proc. IEEE* **64**, 711–721 (1976).
- ²¹⁷W. Dong, X. Ji, W. Wang, T. Li, J. Huang, T. Zhou, Y. Fan, and K. Xu, *Mater. Res. Express* **6**, 095903 (2019).
- ²¹⁸S. M. Quintero, S. W. O. Figueiredo, V. L. Takahashi, R. A. W. Llerena, and A. M. B. Braga, *Sensors* **17**, 1635 (2017).
- ²¹⁹S. Alam, T. Islam, and U. Mittal, *IEEE Sens. J.* **20**, 546–551 (2020).
- ²²⁰L. Shu, B. Peng, Y. Cui, D. Gong, Z. Yang, X. Liu, and W. Zhang, *Sensors* **16**, 1436 (2016).

- ²²¹O. Legrani, O. Elmazria, A. Bartasyte, T. Aubert, and A. Talbi, in *Proceedings of IEEE International Ultrasonics Symposium*, Dresden, Germany, 07–10 October (IEEE, 2012), pp. 2102–2105.
- ²²²W. Chen, W. Jia, Y. Xiao, and G. Wu, *J. Microelectromech. Syst.* **31**, 318–327 (2022).
- ²²³S. A. Bhave and R. T. Howe, in *Proceedings of Solid-State Sensors, Actuators and Microsystem* (IEEE, 2004), pp. 59–60. https://transducer-research-foundation.org/technical_digests/HiltonHead_2004/hh2004_0059.pdf.
- ²²⁴Y. Liu, Y. Cai, Y. Zhang, A. Tovstopyat, S. Liu, and C. Sun, *Micromachines* **11**, 630 (2020).
- ²²⁵Y. Yang, E. J. Ng, P. M. Polunin, Y. Chen, I. B. Flader, S. W. Shaw, M. I. Dykman, and T. W. Kenny, *J. Microelectromech. Syst.* **25**, 859–869 (2016).
- ²²⁶G. Pillai, A. A. Zope, and S. S. Li, *J. Microelectromech. Syst.* **28**, 4–13 (2018).
- ²²⁷L. Wang, C. Wang, Y. Wang, A. Quan, M. Keshavarz, B. P. Madeira, H. Zhang, C. Wang, and M. Kraft, *Sensors* **22**, 3857 (2022).
- ²²⁸F. J. Giessibl, F. Pielmeier, T. Eguchi, T. An, and Y. Hasegawa, *Phys. Rev. B* **84**, 125409 (2011).
- ²²⁹T. D. Ha, *Arch. Appl. Mech.* **92**, 1493–1505 (2022).
- ²³⁰A. Qamar, S. Sherrit, X. Q. Zheng, J. Lee, P. X.-L. Feng, and M. Rais-Zadeh, *J. Microelectromech. Syst.* **28**, 619–627 (2019).
- ²³¹H. Chandralahim, S. A. Bhave, R. G. Polcawich, J. S. Pulskamp, and R. Kaul, in *Proceedings of IEEE International Ultrasonics Symposium (IUS)*, Rome, Italy, 20–23 September (IEEE, 2009), pp. 2145–2148.
- ²³²A. B. Amar, D. Bahloul, F. Gagnon, and A. B. Kouki, *Microsyst. Technol.* **21**, 1567–1576 (2015).
- ²³³V. Tas, S. Olcum, M. D. Aksoy, and A. Atalar, *IEEE Trans. Ultrason. Ferroelectr. Freq. Control* **57**, 448–454 (2010).
- ²³⁴K. E. Wojciechowski, R. H. Olsson, C. D. Nordquist, and M. R. Tuck, in *Proceedings of IEEE International Ultrasonics Symposium (IUS)*, Rome, Italy, 20–23 September (IEEE, 2009), pp. 1179–1182.
- ²³⁵S. Ghosh and J. Y. Lee, *Appl. Phys. Lett.* **110**, 253507 (2017).
- ²³⁶W. Chen, W. Jia, Y. Xiao, and G. Wu, *IEEE Sens. J.* **23**, 15454–15460 (2023).
- ²³⁷V. Kaajakari, T. Mattila, A. Oja, J. Kiihamaki, and H. Seppa, *IEEE Electron Device Lett.* **25**, 173–175 (2004).
- ²³⁸V. Kaajakari, T. Mattila, A. Oja, J. Kiihamaki, H. Kattelus, M. Koskenvuori, P. Rantakari, I. Tittonen, and H. Seppa, in *Proceedings of 12th IEEE International Conference on Solid-State Sensors, Actuators and Microsystem*, Boston, MA, USA, 08–12 June (IEEE, 2003), pp. 951–954.
- ²³⁹K. Y. Fong, M. Poot, and H. X. Tang, *Nano Lett.* **15**, 6116–6120 (2015).
- ²⁴⁰Z. Chen, T. Wang, Q. Jia, J. Yang, Q. Yuan, Y. Zhu, and F. Yang, *Int. J. Mech. Sci.* **204**, 106484 (2021).
- ²⁴¹C. Cassella, Y. Hui, Z. Qian, G. Hummel, and M. Rinaldi, *J. Microelectromech. Syst.* **25**, 275–285 (2016).
- ²⁴²G. Chen, C. Cassella, Z. Qian, G. Hummel, and M. Rinaldi, *J. Micromech. Microeng.* **27**, 034003 (2017).
- ²⁴³K. Nakamura and K. Kumakura, in *Proceedings of IEEE International Ultrasonics Symposium (IUS)*, Seattle, WA, USA, 07–10 November (IEEE, 1995), pp. 999–1002.
- ²⁴⁴V. Thakar and M. Rais-Zadeh, in *Proceedings of IEEE International Frequency Control Symposium & European Frequency and Time Forum (IFCS-EFTF)*, Prague, Czech Republic, 21–25 July (IEEE, 2013), pp. 129–132.
- ²⁴⁵C. Cassella, G. Chen, Z. Qian, G. Hummel, and M. Rinaldi, *IEEE Trans. Electron Devices* **64**, 237–243 (2017).
- ²⁴⁶J. Zhou, Y. Liu, Q. Xu, Y. Xie, Y. Cai, J. Liu, W. Liu, A. Tovstopyat, and C. Sun, *J. Microelectromech. Syst.* **30**, 677–679 (2021).
- ²⁴⁷Z. Hao, S. Pourkamali, and F. Ayazi, *J. Microelectromech. Syst.* **13**, 1043–1053 (2004).
- ²⁴⁸P. K. Joshi, L. H. Bhalotiya, S. W. Jaiswal, V. W. Butram, M. A. Hasamnis, and S. Upadhyay, *Mater. Today: Proc.* **73**, 50–53 (2023).
- ²⁴⁹J. Hu, L. Callaghan, R. Ruby, and B. Otis, in *Proceedings of IEEE Radio Frequency Integrated Circuits Symposium*, Anaheim, CA, USA, 23–25 May (IEEE, 2010), pp. 325–328.
- ²⁵⁰Y. C. Chang, Y. C. Chen, B. R. Li, W. C. Shih, J. M. Lin, W. T. Chang, and C. C. Cheng, *Coat* **11**, 397 (2021).
- ²⁵¹M. Z. Koohi, S. Lee, and A. Mortazawi, *IEEE Trans. Ultrason. Ferroelectr. Freq. Control* **65**, 1468–1474 (2018).
- ²⁵²W. Pang, M. Zhang, and Q. Yang, in *Proceedings of IEEE MTT-S International Microwave Workshop Series on Advanced Materials and Processes for RF and THz Applications (IMWS-AMP)*, Guangzhou, China, 27–29 November (IEEE, 2022).
- ²⁵³C. M. Yang, K. Uehara, S. K. Kim, S. Kameda, H. Nakase, and K. Tsubouchi, in *Proceedings of IEEE International Ultrasonics Symposium (IUS)*, Honolulu, HI, USA, 05–08 October (IEEE, 2003), pp. 170–173.
- ²⁵⁴J. D. Larson, P. D. Bradley, S. Wartenberg, and R. C. Ruby, in *Proceedings of IEEE International Ultrasonics Symposium (IUS)*, San Juan, PR, USA, 22–25 October (IEEE, 2000), pp. 863–868.
- ²⁵⁵R. Ruby, M. Small, F. Bi, D. Lee, L. Callaghan, R. Parker, and S. Ortiz, *IEEE Trans. Ultrason. Ferroelectr. Freq. Control* **59**, 334–345 (2012).
- ²⁵⁶R. C. Ruby, P. Bradley, Y. Oshmyansky, A. Chien, and J. D. Larson, in *Proceedings of IEEE International Ultrasonics Symposium (IUS)*, Atlanta, GA, USA, 07–10 October (IEEE, 2001), pp. 813–821.
- ²⁵⁷H. Sun, S. Lv, F. Long, C. Song, X. Sun, F. Tan, and J. Zhao, *Solid-State Electron.* **195**, 108404 (2022).
- ²⁵⁸J. Zou, A. Gao, and A. P. Pisano, *Appl. Phys. Lett.* **116**, 023505 (2020).
- ²⁵⁹X. Sun, M. Zhang, C. Gao, Y. Ning, Y. Yuan, and W. Pang, *Appl. Phys. Lett.* **115**, 093501 (2019).
- ²⁶⁰G. Esteves, T. R. Young, Z. Tang, S. Yen, T. M. Bauer, M. D. Henry, and R. H. Olsson, *Appl. Phys. Lett.* **118**, 171902 (2021).
- ²⁶¹F. Parsapour, V. Paschenko, H. Champon, P. Nicolay, I. Bleyl, U. Roesler, and P. Muralt, *Appl. Phys. Lett.* **114**, 223103 (2019).
- ²⁶²M. Park, Z. Hao, D. G. Kim, A. Clark, R. Dargis, and A. Ansari, in *Proceedings of 20th IEEE International Conference on Solid-State Sensors, Actuators and Microsystem & Eurosensors XXXIII (TRANSDUCERS & EUROSENSORS XXXIII)*, Berlin, Germany, 23–27 June (IEEE, 2019), pp. 450–453.
- ²⁶³Z. Luo, S. Shao, and T. Wu, *IEEE Trans. Ultrason. Ferroelectr. Freq. Control* **69**, 3108–3116 (2021).
- ²⁶⁴M. Park and A. Ansari, in *Proceedings of Joint Conference of the IEEE International Frequency Control Symposium and International Symposium on Applications of Ferroelectrics (IFCS-ISAF)*, Keystone, CO, USA, 19–23 July (IEEE, 2020), pp. 1–3.
- ²⁶⁵M. Faizan and L. G. Villanueva, *J. Micromech. Microeng.* **30**, 015008 (2020).
- ²⁶⁶T. H. Hsu, S. S. Tung, Y. M. H. G. L. Wu, C. Y. Chang, Y. Ho, Y. H. Chen, Y. Pradeep, R. Chand, and M. H. Li, *J. Micromech. Microeng.* **33**, 054001 (2023).
- ²⁶⁷M. Bharati, L. Rana, K. Jindal, R. Gupta, A. Sharma, and M. Tomar, *IEEE Sens. J.* **23**, 10568–10576 (2023).
- ²⁶⁸T. Luo, Y. Liu, Y. Zou, J. Zhou, W. Liu, G. Wu, Y. Cai, and C. Sun, *Micromachines* **13**, 87 (2022).
- ²⁶⁹H. Sun, S. Lv, A. Zhang, C. Song, X. Sun, F. Tan, L. Liang, Y. Zhu, and J. Zhao, *Micromachines* **13**, 779 (2022).
- ²⁷⁰S. Rassay, D. Mo, and R. Tabrizian, *Micromachines* **13**, 1003 (2022).
- ²⁷¹W. He, L. Li, Z. Tong, H. Liu, Q. Yang, and T. Gao, *Sensors* **23**, 2357 (2023).
- ²⁷²G. Giribaldi, L. Colombo, and M. Rinaldi, *IEEE Trans. Ultrason. Ferroelectr. Freq. Control* **70**, 1201–1212 (2023).
- ²⁷³S. S. Tung, T. H. Hsu, Y. Ho, Y. H. Chen, Y. R. Pradeep, R. Chand, and M. H. Li, in *Proceedings of IEEE International Conference on Micro Electro Mechanical Systems (MEMS)*, Munich, Germany, 15–19 January (IEEE, 2023), pp. 1198–1201.
- ²⁷⁴J. Zou, J. Liu, and G. Tang, *IEEE Access* **7**, 67059–67067 (2019).
- ²⁷⁵J. Zou, A. Gao, and A. P. Pisano, *IEEE Trans. Ultrason. Ferroelectr. Freq. Control* **67**, 671–674 (2019).
- ²⁷⁶W. Z. Wang, Y. Ruan, and Z. You, in *Proceedings of 19th International Conference on Solid-State Sensors, Actuators and Microsystems (Transducers'17)*, Kaohsiung, Taiwan, 18–22 June (IEEE, 2017), pp. 942–945.
- ²⁷⁷J. Liu, T. B. Workie, T. Wu, Z. Wu, K. Gong, J. Bao, and K. Y. Hashimoto, *Micromachines* **11**, 1130 (2020).
- ²⁷⁸W. Liu, Y. Lu, Z. Chen, Q. Jia, J. Zhao, B. Niu, W. Wang, Y. Hao, Y. Zhu, J. Yang, and F. Yang, *Sensors* **23**, 3808 (2023).
- ²⁷⁹G. Wu, D. Xu, B. Xiong, Y. Wang, Y. Wang, and Y. Ma, *J. Microelectromech. Syst.* **21**, 1484–1491 (2012).
- ²⁸⁰M. Park, J. Wang, R. Dargis, A. Clark, and A. Ansari, in *Proceedings of IEEE International Ultrasonics Symposium (IUS)*, Glasgow, UK, 6–9 October (IEEE, 2019), pp. 1689–1692.

- ²⁸¹C. Gao, Y. Zou, J. Zhou, Y. Liu, W. Liu, Y. Cai, and C. Sun, *Micromachines* **13**, 102 (2022).
- ²⁸²T. D. Ha, *J. Electron. Sci. Technol.* **19**, 100120 (2021).
- ²⁸³S. Bendida, J. Koning, J. Bontemps, J. Van Beek, D. Wu, M. A. van Gils, and S. Nath, *Microelectron. Reliab.* **48**, 1227–1231 (2008).
- ²⁸⁴K. Liu, Y. Lu, and T. Wu, *IEEE Electron Device Lett.* **44**, 305–308 (2023).
- ²⁸⁵Z. Hou, X. Wu, D. Xiao, Z. Chen, and J. Su, *J. Micro/Nanolithogr.* **13**, 013016 (2014).
- ²⁸⁶H. Ahmed, P. Rajai, and M. J. Ahamed, *AIP Adv.* **12**, 015319 (2022).
- ²⁸⁷M. A. S. Silva, T. S. M. Fernandes, and A. S. B. Sombra, *J. Appl. Phys.* **112**, 074106 (2012).
- ²⁸⁸A. Jaakkola, M. Prunnila, T. Pensala, J. Dekker, and P. Pekko, *IEEE Trans. Ultrason. Ferroelectr. Freq. Control* **61**, 1063–1074 (2014).
- ²⁸⁹M. Gonzalez, A. Jourdain, B. Vandevelde, and H. A. Tilmans, in *Proceedings of EuroSimE 2008-International Conference on Thermal, Mechanical and Multi-Physics Simulation and Experiments in Microelectronics and Microsystems*, Freiburg im Breisgau, Germany, 20–23 April (IEEE, 2008), pp. 1–5.
- ²⁹⁰A. Jaakkola, M. Prunnila, T. Pensala, J. Dekker, and P. Pekko, in *Proceedings of IEEE International Frequency Control Symposium & European Frequency and Time Forum (IFCS-EFTF)*, Prague, Czech Republic, 21–25 July (IEEE, 2013), pp. 421–424.
- ²⁹¹H. Yu, W. Pang, H. Zhang, and E. S. Kim, in *Proceedings of 18th IEEE International Conference on Micro Electro Mechanical Systems (MEMS)*, Miami Beach, FL, USA, 30 January–03 February (IEEE, 2005), pp. 28–31.
- ²⁹²M. Shahmohammadi, B. P. Harrington, J. Gonzales, and R. Abdolvand, in *Proceedings of Solid-State Sensors, Actuators and Microsystem Workshop* (IEEE, 2012), pp. 371–374.
- ²⁹³B. Jiang, S. Huang, J. Zhang, and Y. Su, *Micromachines* **12**, 26 (2020).
- ²⁹⁴S. Wang, W. C. Chen, B. Bahr, W. Fang, S. S. Li, and D. Weinstein, *IEEE Trans. Ultrason. Ferroelectr. Freq. Control* **62**, 1166–1178 (2015).
- ²⁹⁵A. Bokaian, *J. Sound Vib.* **142**, 481–498 (1990).
- ²⁹⁶J. Zhou, N. Moldovan, L. Stan, H. Cai, D. A. Czaplewski, and D. López, *Nano Lett.* **20**, 5693–5698 (2020).
- ²⁹⁷S. C. Jun, X. M. H. Huang, X. M. H. Manolidis, C. A. Zorman, M. Mehregany, and J. Hone, *Nanotechnology* **17**, 1506 (2006).
- ²⁹⁸M. J. Lachut and J. E. Sader, *Phys. Rev. B* **85**, 085440 (2012).
- ²⁹⁹R. B. Karabalin, L. G. Villanueva, M. H. Matheny, J. E. Sader, and M. L. Roukes, *Phys. Rev. Lett.* **108**, 236101 (2012).
- ³⁰⁰H. Suzuki, N. Yamaguchi, and H. Izumi, *Acoust. Sci. Technol.* **30**, 348–354 (2009).
- ³⁰¹A. Ding, M. Reusch, Y. Lu, N. Kurz, R. Lozar, T. Christoph, R. Driad, O. Ambacher, and A. Zukauskaite, in *Proceedings of IEEE International Ultrasonics Symposium*, Kobe, Japan, 22–25 October (IEEE, 2018), pp. 1–9.
- ³⁰²A. Ding, N. Kurz, R. Driad, Y. Lu, R. Lozar, T. Christoph, L. Kirste, O. Ambacher, and A. Zukauskaite, in *Proceedings of IEEE International Ultrasonics Symposium*, Glasgow, UK, 06–09 October (IEEE, 2019), pp. 710–715.
- ³⁰³R. Hino, M. Esashi, and S. Tanaka, in *Proceedings of 23rd IEEE International Conference on Micro Electro Mechanical Systems (MEMS)*, Hong Kong, China, 24–28 January (IEEE, 2010), pp. 871–874.
- ³⁰⁴E. Kamiyama and K. Sueoka, *AIP Adv.* **13**, 085224 (2023).
- ³⁰⁵E. J. Boyd, L. Li, R. Blue, and D. Uttamchandani, *Sens. Actuator A Phys.* **198**, 75–80 (2013).
- ³⁰⁶J. B. Wachtman, W. E. Tefft, D. G. Lam, and C. S. Apstein, *Phys. Rev.* **122**, 1754–1759 (1961).
- ³⁰⁷G. Boldeiu, G. E. Ponchak, A. Nicoloiu, C. Nastase, I. Zdru, A. Dinescu, and A. Müller, *IEEE Access* **10**, 741–752 (2022).
- ³⁰⁸M. Hu and F. L. Duan, *Solid-State Electron.* **150**, 28–34 (2018).
- ³⁰⁹W. Sui, T. Kaisar, H. Wang, Y. Wu, J. Lee, H. Xie, and P. X.-L. Feng, in *Proceedings of IEEE Sensors*, Dallas, TX, USA, 30 October–02 November (IEEE, 2022), pp. 1–4.
- ³¹⁰T. T. Yen, C. M. Lin, X. Zhao, V. V. Felmetser, D. G. Senesky, M. A. Hopcroft, and A. P. Pisano, in *Proceedings of 23rd IEEE International Conference on Micro Electro Mechanical Systems (MEMS)*, Hong Kong, China, 24–28 January (IEEE, 2010), pp. 731–734.
- ³¹¹M. Pozzi, M. Hassan, A. J. Harris, J. S. Burdess, L. Jiang, K. K. Lee, R. Cheung, G. J. Phelps, N. G. Wright, and C. A. Zorman, *J. Phys. D: Appl. Phys.* **40**, 3335 (2007).
- ³¹²W. Sui, H. Wang, J. Lee, A. Qamar, M. Rais-Zadeh, and P. X.-L. Feng, *Adv. Funct. Mater.* **32**, 2202204 (2022).
- ³¹³H. Lv, X. Shi, Y. Ai, Z. Liu, D. Lin, L. Jia, Z. Cheng, J. Yang, and Y. Zhang, *J. Semicond.* **43**(11), 114101 (2022).
- ³¹⁴T. Aubert, J. Bardong, O. Legrani, O. Elmazria, M. Badreddine Assouar, G. Bruckner, and A. Talbi, *J. Appl. Phys.* **114**, 014505 (2013).
- ³¹⁵S. Fei and H. Ren, *Micromachines* **12**, 143 (2021).
- ³¹⁶A. K. Samarao and F. Ayazi, *IEEE Trans. Electron Devices* **59**, 87–93 (2012).
- ³¹⁷A. Hajjam, A. Rahafrooz, and S. Pourkamali, in *2010 IEEE International Electron Device Meeting (IEDM)*, San Francisco, CA, USA, 06–08 December (IEEE, 2010), pp. 7.5.1–7.5.4.
- ³¹⁸A. Hajjam, A. Logan, and S. Pourkamali, *J. Microelectromech. Syst.* **21**, 681–687 (2012).
- ³¹⁹M. A. Hopcroft, W. D. Nix, and T. W. Kenny, *J. Microelectromech. Syst.* **19**, 229–238 (2010).
- ³²⁰M. Rinaldi, A. Tazzoli, J. Segovia-Fernandez, V. Felmetser, and G. Piazza, in *Proceedings of 25th IEEE International Conference on Micro Electro Mechanical Systems (MEMS)*, Paris, France, 29 January–02 February (IEEE, 2012), pp. 696–699.
- ³²¹J. R. Liu and W. C. Li, *J. Micromech. Microeng.* **30**, 014002 (2020).
- ³²²M. Reusch, K. Holc, V. Lebedev, N. Kurz, A. Žukauskaitė, and O. Ambacher, *IEEE Sens. J.* **18**, 7810–7818 (2018).
- ³²³R. Melamud, M. Hopcroft, C. Jha, B. Kim, S. Chandorkar, R. Candler, and T. W. Kenny, in *Proceedings of International Conference on Solid-State Sensors, Actuators and Microsystems (Transducers'05)*, Seoul, Korea (South), 05–09 June (IEEE, 2005), pp. 392–395.
- ³²⁴R. A. Schneider, T. Lin Naing, T. O. Rocheleau, and C. T.-C. Nguyen, in *Proceedings of IEEE International Frequency Control Symposium & European Frequency and Time Forum (IFCS-EFTF)*, Denver, CO, USA, 12–16 April (IEEE, 2015), pp. 700–705.
- ³²⁵M. H. Li, C. Y. Chen, C. S. Li, C. H. Chin, and S. S. Li, *J. Microelectromech. Syst.* **24**, 446–457 (2015).
- ³²⁶Y. Zheng, S. M. H. Gangaraj, J. Wang, M. Park, Y. Fang, and A. Ansari, *J. Microelectromech. Syst.* **33**, 620–630 (2024).
- ³²⁷M. Narducci, M. Ferrari, V. Ferrari, and H. Campanella, *Procedia Eng.* **87**, 1152–1155 (2014).
- ³²⁸H. K. Kwon, L. C. Ortiz, G. D. Vukasin, Y. Chen, D. D. Shin, and T. W. Kenny, in *Proceedings of 20th International Conference on Solid-State Sensors, Actuators and Microsystem & Eurosensors XXXIII (TRANSDUCERS & EUROSENSORS XXXIII)*, Berlin, Germany, 23–27 June (IEEE, 2019), pp. 2072–2075.
- ³²⁹W. Sui, M. Sheplak, and P. X.-L. Feng, in *Proceedings of 37th IEEE International Conference on Micro Electro Mechanical Systems (MEMS)*, Austin, TX, USA, 21–25 January (IEEE, 2024), pp. 638–641.
- ³³⁰W. Sui and P. X.-L. Feng, *Appl. Phys. Lett.* **125**, 022201 (2024).
- ³³¹T. Aubert, O. Elmazria, B. Assouar, L. Bouvot, and M. Oudich, *Appl. Phys. Lett.* **96**, 203503 (2010).
- ³³²T. Aubert, O. Elmazria, B. Assouar, L. Bouvot, M. Hehn, S. Weber, M. Oudich, and D. Geneve, *IEEE Trans. Ultrason. Ferroelectr. Freq. Control* **58**, 603–610 (2011).
- ³³³C. M. Lin, T. T. Yen, V. V. Felmetser, M. A. Hopcroft, J. H. Kuypers, and A. P. Pisano, *Appl. Phys. Lett.* **97**, 083501 (2010).
- ³³⁴G. Esteves, S. D. Habermehl, P. J. Clews, C. Fritch, and B. A. Griffin, *J. Microelectromech. Syst.* **28**, 859–864 (2019).
- ³³⁵A. Qamar, S. R. Eisner, D. G. Senesky, and M. Rais-Zadeh, *J. Microelectromech. Syst.* **29**, 900–905 (2020).
- ³³⁶Y. Naito, P. Helin, K. Nakamura, J. De Coster, B. Guo, L. Haspeslagh, K. Onishi, and H. A. C. Tilmans, in *2010 IEEE Int. Electron Device Meeting (IEDM)*, San Francisco, CA, USA, 06–08 December (IEEE, 2010), pp. 7.1.1–7.1.4.
- ³³⁷A. Koumela, D. Mercier, C. Marcoux, L. Duraffourg, and S. T. Purcell, in *Proceedings of IEEE International Frequency Control Symposium (IFCS)*, Baltimore, MD, USA, 21–24 May (IEEE, 2012), pp. 1–4.
- ³³⁸H. Zhu and J. E. Y. Lee, in *Proceedings of International Frequency Control Symposium (IFCS)*, Taipei, Taiwan, 19–22 May (IEEE, 2014), pp. 1–4.
- ³³⁹M. A. Hopcroft, M. Agarwal, K. K. Park, B. Kim, C. M. Jha, R. N. Candler, G. Yama, B. Murmann, and T. W. Kenny, in *Proceedings of 19th IEEE International Conference on Micro Electro Mechanical Systems (MEMS)*, Istanbul, Turkey, 22–26 January (IEEE, 2006), pp. 222–225.

- ³⁴⁰S. Shahraini, R. Abdolvand, and H. Fatemi, in *Proceedings of IEEE International Frequency Control Symposium (IFCS)*, Olympic Valley, CA, USA, 21–24 May (IEEE, 2018), pp. 1–5.
- ³⁴¹G. Mussi, M. Carrara, G. Langfelder, and G. Gattere, in *Proceedings of IEEE International Frequency Control Symposium & European Frequency and Time Forum (IFCS-EFTF)*, Orlando, FL, USA, 14–18 April (IEEE, 2019), pp. 1–3.
- ³⁴²T. Kose, K. Azgin, and T. Akin, *J. Micromech. Microeng.* **26**, 045012 (2016).
- ³⁴³C. M. Jha, G. Bahl, R. Melamud, S. A. Chandorkar, M. A. Hopcroft, B. Kim, M. Agarwal, J. Salvia, H. Mehta, and T. W. Kenny, in *Proceedings of International Conference on Solid-State Sensors, Actuators and Microsystems (Transducers'07)*, Lyon, France, 10–14 June (IEEE, 2007), pp. 229–232.
- ³⁴⁴T. Y. Chen, C. P. Tsai, and W. C. Li, in *Proceedings of 36th IEEE International Conference on Micro Electro Mechanical Systems (MEMS)*, Munich, Germany, 15–19 January (IEEE, 2023), pp. 185–188.
- ³⁴⁵M. U. Demirci and C. T.-C. Nguyen, in *Proceedings of IEEE International Frequency Control Symposium & European Frequency and Time Forum (IFCS-EFTF)*, Tampa, FL, USA, 04–08 May (IEEE, 2003), pp. 810–818.
- ³⁴⁶J. R. Clark, A. R. Brown, G. He, and W.-T. Hsu, in *Proceedings of 17th IEEE International Conference on Solid-State Sensors, Actuators and Microsystems (TRANSDUCERS & EUROSENSORS XXVII)*, Barcelona, Spain, 16–20 June (IEEE, 2013), pp. 794–797.
- ³⁴⁷B. Kim, R. Melamud, M. A. Hopcroft, S. A. Chandorkar, G. Bahl, M. Messana, R. N. Candler, G. Yama, and T. Kenny, in *Proceedings of IEEE International Frequency Control Symposium & European Frequency and Time Forum (IFCS-EFTF)*, Geneva, Switzerland, 29 May–01 June (IEEE, 2007), pp. 1214–1219.
- ³⁴⁸S. Moradian, S. Shahraini, and R. Abdolvand, in *Proceedings of 2016 IEEE International Frequency Control Symposium (IFCS)*, New Orleans, LA, USA, 09–12 May (IEEE, 2016), pp. 1–4.
- ³⁴⁹F. Casset, C. Durand, Y. Civet, E. Ollier, J. F. Carpentier, P. Ancey, and P. Robert, in *Proceedings of IEEE 11th International Thermal, Mechanical & Multi-Physics Simulation, and Experiments in Microelectronics and Microsystems (EuroSimE)*, Bordeaux, France, 26–28 April (IEEE, 2010), pp. 1–5.
- ³⁵⁰Z. Wu and M. Rais-Zadeh, in *Proceedings of 28th IEEE International Conference on Micro Electro Mechanical Systems (MEMS)*, Estoril, Portugal, 18–22 January (IEEE, 2015), pp. 793–796.
- ³⁵¹T. Pensala, A. Jaakkola, M. Prunnila, and J. Dekker, in *Proceedings of IEEE International Ultrasonics Symposium*, Orlando, FL, USA, 18–21 October (IEEE, 2011), pp. 1952–1955.
- ³⁵²A. K. Samarao and F. Ayazi, in *2009 IEEE International Electron Devices Meeting (IEDM)*, Baltimore, MD, 7–9 December (IEEE, 2009), pp. 1–4.
- ³⁵³A. Hajjam, A. Rahaftrooz, and S. Pourkamali, in *Proceedings of 24th IEEE International Conference on Micro Electro Mechanical Systems (MEMS)*, Cancun, Mexico, 23–27 January (IEEE, 2011), pp. 801–804.
- ³⁵⁴A. Jaakkola, M. Prunnila, and T. Pensala, in *Proceedings of IEEE International Frequency Control Symposium (IFCS)*, Baltimore, MD, USA, 21–24 May (IEEE, 2012), pp. 1–5.
- ³⁵⁵T. Pensala, M. Prunnila, and A. Jaakkola, in *Proceedings of IEEE International Frequency Control Symposium (IFCS)*, Baltimore, MD, USA, 21–24 May (IEEE, 2012), pp. 1–4.
- ³⁵⁶T. Pensala, A. Jaakkola, M. Prunnila, and J. Dekker, in *Proceedings of IEEE International Ultrasonics Symposium (IUS)*, Orlando, FL, USA, 18–21 October (IEEE, 2011), pp. 1952–1955.
- ³⁵⁷H. Zhu, C. Tu, G. Shan, and J. E. Y. Lee, *Sens. Actuator A Phys.* **215**, 189–196 (2014).
- ³⁵⁸D. D. Shin, D. B. Heinz, H. K. Kwon, Y. Chen, and T. W. Kenny, in *Proceedings of IEEE International Symposium on Inertial Sensors and Systems (INERTIAL)*, Lake Como, Italy, 26–29 March (IEEE, 2018), pp. 1–4.
- ³⁵⁹A. K. Samarao and F. Ayazi, in *Proceedings of IEEE International Frequency Control Symposium (IFCS)*, Newport Beach, CA, USA, 01–04 June (IEEE, 2010), pp. 334–339.
- ³⁶⁰A. K. Samarao, G. Casinovi, and F. Ayazi, in *Proceedings of 23rd IEEE International Conference on Micro Electro Mechanical Systems (MEMS)*, Hong Kong, China, 24–28 January (IEEE, 2010), pp. 116–119.
- ³⁶¹W. T. Hsu and C. T.-C. Nguyen, in *Proceedings of 15th IEEE International Conference on Micro Electro Mechanical Systems (MEMS)*, Las Vegas, NV, USA, 24–24 January (IEEE, 2002), pp. 731–734.
- ³⁶²J. R. Liu and W. C. Li, in *Proceedings of 32nd IEEE International Conference on Micro Electro Mechanical Systems (MEMS)*, Seoul, Korea (South), 27–31 January (IEEE, 2019), pp. 161–164.
- ³⁶³K. W. Lan, I. F. Chung, C. P. Tsai, T. Y. Chen, and W. C. Li, in *Proceedings of 37th IEEE International Conference on Micro Electro Mechanical Systems (MEMS)*, Austin, TX, USA, 21–25 January (IEEE, 2024), pp. 140–143.
- ³⁶⁴I. C. Hsieh, H. S. Zheng, C. P. Tsai, T. Y. Chen, and W. C. Li, in *Proceedings of 36th IEEE International Conference on Micro Electro Mechanical Systems (MEMS)*, Munich, Germany, 15–19 January (IEEE, 2023), pp. 1155–1158.
- ³⁶⁵R. Perelló-Roig, S. Barceló, J. Verd, S. Bota, and J. Segura, *Sens. Actuator A Phys.* **373**, 115435 (2024).
- ³⁶⁶W.-T. Hsu and C. T.-C. Nguyen, in *Proceedings of IEEE International Ultrasonics Symposium*, Sendai, Japan, 05–08 October (IEEE, 1998), pp. 945–948.
- ³⁶⁷W.-T. Hsu, J. R. Clark, and C. T.-C. Nguyen, in *2000 IEEE Int. Electron Device Meeting (IEDM)*, San Francisco, CA, USA, 10–13 December (IEEE, 2000), pp. 399–402.
- ³⁶⁸J. R. Clark, M. A. Abdelmoneum, and C. T.-C. Nguyen, in *Proceedings of IEEE International Frequency Control Symposium & European Frequency and Time Forum (IFCS-EFTF)*, Prague, Czech Republic, 04–08 May (IEEE, 2003), pp. 802–809.
- ³⁶⁹X. Liu, Q. Xie, A. Ozgurluk, Q. Jin, and C. T.-C. Nguyen, in *Proceedings of 36th IEEE International Conference on Micro Electro Mechanical Systems (MEMS)*, Austin, TX, USA, 21–25 January (IEEE, 2024), pp. 144–147.
- ³⁷⁰J. Han, Y. Xiao, W. Chen, K. Zhu, and G. Wu, *J. Microelectromech. Syst.* **32**, 271–278 (2023).
- ³⁷¹M. Defoort, P. Taheri-Tehrani, and D. Horsley, *Appl. Phys. Lett.* **109**, 153502 (2016).
- ³⁷²S. G. Zadeh, T. Saha, K. Allidina, F. Nabki, and M. N. El-Gamal, in *IEEE Midwest Symposium on Circuits and Systems*, Seattle, WA, USA, 01–04 August (IEEE, 2010), pp. 1193–1196.
- ³⁷³C. S. Liu, R. Tabrizian, and F. Ayazi, *IEEE Trans. Ultrason. Ferroelectr. Freq. Control* **65**, 1492–1499 (2018).
- ³⁷⁴G. Xereas and V. P. Chodavarapu, in *Proceedings of Micromachining and Microfabrication Process Technology XIX*, San Francisco, CA, USA (IEEE, 2014), pp. 159–168.
- ³⁷⁵M.-H. Li, C.-Y. Chen, C.-S. Li, C.-H. Chin, C.-C. Chen, and S.-S. Li, in *2013 IEEE International Electron Device Meeting (IEDM)*, Washington, DC, USA, 09–11 December (IEEE, 2013), pp. 18.4.1–18.4.4.
- ³⁷⁶M.-H. Li, C.-Y. Chen, C.-S. Li, C.-H. Chin, and S.-S. Li, *J. Microelectromech. Syst.* **24**, 360–372 (2015).
- ³⁷⁷H. Nakanishi, H. Nakamura, T. Tsurunari, J. Fujiwara, Y. Hamaoka, and K. Y. Hashimoto, *Jpn. J. Appl. Phys.* **51**, 07GC15 (2012).
- ³⁷⁸R. Goto, J. Fujiwara, H. Nakamura, T. Tsurunari, H. Nakanishi, and Y. Hamaoka, *Jpn. J. Appl. Phys.* **52**, 07HD12 (2013).
- ³⁷⁹Y. J. Guo, J. Zhang, C. Zhao, P. A. Hu, X. T. Zu, and Y. Q. Fu, *Optik* **125**, 5800–5802 (2014).
- ³⁸⁰T. Fujimaki, M. Suzuki, and S. Kakio, *Jpn. J. Appl. Phys.* **59**, SKKC01 (2020).
- ³⁸¹J. Hayashi, K. Yamaya, S. Asakawa, M. Suzuki, S. Kakio, A. Tezuka, H. Kuwae, T. Yonai, K. Kishida, and J. Mizuno, *Jpn. J. Appl. Phys.* **58**, SGGC12 (2019).
- ³⁸²W. Gubinelli, L. Colombo, R. Tetro, W. Sui, N. Maietta, Y. Sautriot, P. Simeoni, P. X.-L. Feng, and M. Rinaldi, in *Proceedings of IEEE Sensors*, Kobe, Japan, 20–23 October (IEEE, 2024), pp. 1–4.
- ³⁸³R. Wang, S. A. Bhave, and K. Bhattacharjee, in *Proceedings of IEEE International Frequency Control Symposium (IFCS)*, Taipei, Taiwan, 19–22 May (IEEE, 2014), pp. 1–4.
- ³⁸⁴Y. Majd and R. Abdolvand, “Designing the turnover temperature in Lamb-wave lithium tantalate resonators,” *IEEE Electron Device Lett.* **45**, 1508–1511 (2024).
- ³⁸⁵K. Yamanouchi and T. Ishii, *Jpn. J. Appl. Phys.* **41**, 3480 (2002).
- ³⁸⁶C. C. Cheng, C. J. Chang, Y. C. Chen, and K. S. Kao, in *Proceedings of IEEE International Ultrasonics Symposium*, Montreal, QC, Canada, 23–27 August (IEEE, 2004), pp. 1884–1887.

- ³⁸⁷M. Kadota, T. Nakao, K. Nishiyama, S. Kido, M. Kato, R. Omote, H. Yonekura, N. Takada, and R. Kita, *Jpn. J. Appl. Phys.* **46**, 4714 (2007).
- ³⁸⁸T. Nakao, M. Kadota, K. Nishiyama, Y. Nakai, D. Yamamoto, Y. Ishiura, T. Komura, N. Takada, and R. Kita, *Jpn. J. Appl. Phys.* **46**, 4760 (2007).
- ³⁸⁹H. Nakamura, H. Nakanishi, R. Goto, K. Y. Hashimoto, and M. Yamaguchi, *Jpn. J. Appl. Phys.* **49**, 07HD20 (2010).
- ³⁹⁰H. Nakanishi, H. Nakamura, T. Tsurunari, J. Fujiwara, Y. Hamaoka, and K. Y. Hashimoto, *Jpn. J. Appl. Phys.* **50**, 07HD13 (2011).
- ³⁹¹S. Wu, Z. Wu, H. Qian, F. Bao, G. Tang, F. Xu, and J. Zou, in *Proceedings of 36th IEEE International Conference on Micro Electro Mechanical Systems (MEMS)*, Munich, Germany, 15–19 January (IEEE, 2023), pp. 631–634.
- ³⁹²M. H. Li, C. Y. Chen, R. Lu, Y. Yang, T. Wu, and S. Gong, *J. Microelectromech. Syst.* **28**, 799–809 (2019).
- ³⁹³A. E. Hassanien, R. Lu, and S. Gong, in *Proceedings of IEEE MTT-S International Microwave Symposium*, Atlanta, GA, USA, 07–25 June (IEEE, 2021), pp. 218–221.
- ³⁹⁴A. E. Hassanien and S. Gong, in *Proceedings of IEEE International Ultrasonics Symposium*, Xi'an, China, 11–16 September (IEEE, 2021), pp. 1–4.
- ³⁹⁵S. Wu, L. Wu, F. C. Chang, and J. H. Chang, *Jpn. J. Appl. Phys.* **40**, L471 (2001).
- ³⁹⁶S. Wu, Y. C. Chen, and Y. S. Chang, *Jpn. J. Appl. Phys.* **41**, 4605 (2002).
- ³⁹⁷J. Xu, J. S. Thakur, G. Hu, Q. Wang, Y. Danylyuk, H. Ying, and G. W. Auner, *Appl. Phys. A* **83**, 411–415 (2006).
- ³⁹⁸K. S. Kao, C. C. Cheng, Y. C. Chen, and Y. H. Lee, *Appl. Phys. A* **76**, 1125–1127 (2003).
- ³⁹⁹K. S. Kao, C. C. Cheng, Y. C. Chen, and C. H. Chen, *Appl. Surf. Sci.* **230**, 334–339 (2004).
- ⁴⁰⁰F. Huang, C. Ma, J. Jiang, X. He, F. Yang, J. C. Q. Ren, Y. Ma, and N. Wang, in *Proceedings of IEEE International Conference on Microw. Acoust. Mech. (IC-MAM)*, Chengdu, China, 13–15 May (IEEE, 2024), pp. 73–76.
- ⁴⁰¹F. La Via, A. Severino, R. Anzalone, C. Bongiorno, G. Litrico, M. Mauceri, M. Schoeler, P. Schuh, and P. Wellmann, *Mater. Sci. Semicond. Process.* **78**, 57–68 (2018).
- ⁴⁰²H. Jianqiang, Z. Changchun, L. Junhua, and H. Yongning, *Sens. Actuator A Phys.* **101**, 37–41 (2002).
- ⁴⁰³R. Sandberg, W. Svendsen, K. Mølhav, and A. Boisen, *J. Microelectromech. Microeng.* **15**, 1454 (2005).
- ⁴⁰⁴T. He, J. Lee, Z. Wang, and P. X.-L. Feng, in *Proceedings of IEEE 27th International Conference on Micro Electro Mechanical Systems (MEMS 2014)*, San Francisco, CA, USA, 26–30 January (IEEE, 2014), pp. 1079–1082.
- ⁴⁰⁵C. M. Su, M. Wuttig, A. Fekade, and M. Spencer, *J. Appl. Phys.* **77**, 5611–5615 (1995).
- ⁴⁰⁶T. Yibibulla, Y. Jiang, S. Wang, and H. Huang, *Appl. Phys. Lett.* **118**, 043103 (2021).
- ⁴⁰⁷S. Perisanu, V. Gouttenoire, P. Vincent, A. Ayari, M. Choueib, M. Bechelany, D. Cornu, and S. T. Purcell, *Phys. Rev. B* **77**, 165434 (2008).
- ⁴⁰⁸D. Leisen, R. Rusanov, F. Rohlfing, T. Fuchs, C. Eberl, H. Riesch-Oppermann, and O. Kraft, *Rev. Sci. Instrum.* **86**, 055104 (2015).
- ⁴⁰⁹X. Zhao, F. Yang, H. Zhang, and P. Xiao, *J. Raman Spectrosc.* **43**, 945–948 (2012).
- ⁴¹⁰M. Ziae-Moayyed, S. D. Habermehl, D. W. Branch, P. J. Clews, and R. Olsson, in *Proceedings of 24th IEEE International Conference on Micro Electro Mechanical Systems (MEMS)*, Cancun, Mexico, 23–27 January (IEEE, 2011), pp. 788–792.
- ⁴¹¹J. Yang, B. Hamelin, and F. Ayazi, *J. Microelectromech. Syst.* **29**, 1473–1482 (2020).
- ⁴¹²R. Yang, Z. Wang, J. Lee, K. Ladhave, D. J. Young, and P. X.-L. Feng, in *Proceedings of 2015 IEEE International Frequency Control Symposium (IFCS)*, Taipei, Taiwan, May (IEEE, 2014), pp. 1–3.
- ⁴¹³J. Bjurström, G. Wingqvist, V. Yantchev, and I. Katardjiev, *J. Microelectromech. Microeng.* **17**, 651 (2007).
- ⁴¹⁴S. U. Son, I. Song, J. Shin, H. S. Park, J. Cui, C. S. Kim, and D. H. Kim, in *IEEE/MTT-S International Microwave Symposium*, Montreal, QC, 17–22 June (IEEE, 2012), pp. 1–3.
- ⁴¹⁵S. U. Son, I. Song, J. Shin, H. S. Park, J. Cui, C. S. Kim, and D. H. Kim, in *Proceedings of IEEE 42nd European Microwave Conference*, Amsterdam, Netherlands, 9 October–1 November (IEEE, 2012), pp. 100–103.
- ⁴¹⁶W. C. Ang, P. Kropelnicki, H. Campanella, Y. Zhu, A. B. Randles, H. Cai, Y. A. Gu, K. C. Leong, and C. S. Tan, in *Proceedings of 25th IEEE International Conference on Micro Electro Mechanical Systems (MEMS)*, San Francisco, CA, USA, 26–30 January (IEEE, 2014), pp. 688–691.
- ⁴¹⁷Q. Xie, N. Wang, C. Sun, A. B. Randles, P. Singh, X. Zhang, and Y. Gu, *Appl. Phys. Lett.* **110**, 083501 (2017).
- ⁴¹⁸M. Moosavifar, A. Ansari, and M. Rais-Zadeh, in *Proceedings of IEEE Sensors*, Orlando, FL, USA (IEEE, 2016), pp. 1–3.
- ⁴¹⁹N. Wang, Y. Zhu, B. Chen, and Y. Zhang, in *Proceedings of IEEE International Ultrasonics Symposium*, Glasgow, UK, 06–09 October (IEEE, 2019), pp. 1714–1716.
- ⁴²⁰L. Lamanna, F. Rizzi, V. R. Bhethanabotla, and M. D. Vittorio, *Sens. Actuators A: Phys.* **315**, 112268 (2020).
- ⁴²¹X. Le, X. Wang, J. Pang, Y. Liu, B. Fang, Z. Xu, C. Gao, Y. Xu, and J. Xie, *Sens. Actuators B: Chem.* **255**, 2454–2461 (2018).
- ⁴²²Y. Wang, J. Xu, Z. J. Jia, X. Xu, and Y. C. Xie, in *Symposium on Piezoelectricity, Acoustic Waves, and Device Applications (SPAUDA)*, Chengdu, China, 27–30 October (IEEE, 2017), pp. 103–106.
- ⁴²³X. Le and J. Xie, in *Proceedings of 30th IEEE International Conference on Micro Electro Mechanical Systems (MEMS)*, Las Vegas, NV, USA, 22–26 January (IEEE, 2017), pp. 1060–1063.
- ⁴²⁴H. L. Kao, W. C. Chen, W. C. Chien, H. F. Lin, T. C. Chen, C. Y. Lin, Y. T. Lin, J. I. Chyi, and C. H. Hsu, *Jpn. J. Appl. Phys.* **47**, 124–129 (2008).
- ⁴²⁵G. Bu, D. Ciplys, M. Shur, L. J. Schowalter, S. Schujman, and R. Gaska, *Electron. Lett.* **39**, 755 (2003).
- ⁴²⁶K. S. Kao, C. C. Cheng, and Y. C. Chen, *IEEE Trans. Ultrason. Ferroelectr. Freq. Control* **49**, 345–349 (2002).
- ⁴²⁷J. H. Kuypers, C. M. Lin, G. Vigevani, and A. P. Pisano, in *Proceedings of IEEE International Frequency Control Symposium (IFCS)*, Honolulu, HI, USA, 19–21 May (IEEE, 2008), pp. 240–249.
- ⁴²⁸G. Chance, T. Meyer, S. Stoeckl, B. Neurauter, G. Patane, B. Neubauer, G. Minichshofer, J. H. Kuypers, J. Schoepf, R. Rebel, and D. Weninger, in *Proceedings of IEEE International Frequency Control Symposium (IFCS)*, Taipei, Taiwan, 19–22 May (IEEE, 2014), pp. 1–3.
- ⁴²⁹J. L. Fu, R. Tabrizian, and F. Ayazi, *IEEE Trans. Electron Devices* **61**, 591–597 (2014).
- ⁴³⁰Y. Long, Z. Liu, C. Wehner, and A. Farrokh, in *Proceedings of IEEE International Symposium on Inertial Sensors and Systems (INERTIAL)*, Lihue, HI, USA, 28–31 March (IEEE, 2023), pp. 1–4.
- ⁴³¹M. Gillinger, K. Shaposhnikov, T. Knobloch, M. Schneider, M. Kaltenbacher, and U. Schmid, *Appl. Phys. Lett.* **108**, 231601 (2016).
- ⁴³²C. Caliendo, *Appl. Phys. Lett.* **83**, 4851–4853 (2003).
- ⁴³³Y. Wang, G. Sha, C. Harlow, M. Yazbeck, and M. Khafizov, *Nucl. Instrum. Methods Phys. Res. B* **481**, 35–41 (2020).
- ⁴³⁴Y. Ai, H. Lv, Y. Huang, J. He, Y. Wang, J. Wu, and Y. Zhang, *IEEE Sens. J.* **23**, 8261–8267 (2023).
- ⁴³⁵W. Dong, X. Ji, J. Huang, T. Zhou, T. Li, Y. Fan, and K. Xu, *Semicond. Sci. Technol.* **34**, 055005 (2019).
- ⁴³⁶E. Blampain, O. Elmazria, O. Legrani, S. McMurtry, F. Montaigne, C. Fu, K. K. Lee, and S. S. Yang, in *Proceedings of IEEE International Ultrasonics Symposium*, Prague, Czech Republic, 21–25 July (IEEE, 2013), pp. 1081–1084.
- ⁴³⁷E. Blampain, O. Elmazria, T. Aubert, B. Assouar, and O. Legrani, in *Proceedings of IEEE SENSORS*, Limerick, Ireland, 28–31 October (IEEE, 2011), pp. 610–613.
- ⁴³⁸E. Blampain, O. Elmazria, T. Aubert, B. M. Assouar, and O. Legrani, *IEEE Sens. J.* **13**, 4607–4612 (2013).
- ⁴³⁹J. Streque, J. Camus, T. Laroche, S. Hage-Ali, H. M'Jahed, M. Rammal, T. Aubert, M. A. Djouadi, S. Ballandras, and O. Elmazria, *IEEE Sens. J.* **20**, 6985–6991 (2020).
- ⁴⁴⁰T. Aubert, O. Elmazria, B. Assouar, E. Blampain, A. Hamdan, D. Geneve, and S. Weber, *IEEE Trans. Ultrason. Ferroelectr. Freq. Control* **59**, 999–1005 (2012).
- ⁴⁴¹K. S. Kao, Y. C. Chen, Y. H. Lee, and C. C. Cheng, in *Proceedings of IEEE International Ultrasonics Symposium*, Munich, Germany, 08–11 October (IEEE, 2002), pp. 239–242.
- ⁴⁴²M. B. Assouar, O. Elmazria, M. Elhakiki, and P. Alnot, *J. Vac. Sci. Technol. B* **22**, 1717–1722 (2004).

- ⁴⁴³M. B. Assouar, O. Elmazria, P. Kirsch, P. Alnot, and V. Mortet, in *Proceedings of IEEE International Ultrasonics Symposium*, New York, NY, USA, 28–31 October (IEEE, 2007), pp. 284–287.
- ⁴⁴⁴S. Fujii, S. Kawano, T. Umeda, M. Fujioka, and M. Yoda, in *Proceedings of IEEE International Ultrasonics Symposium*, Beijing, China, 02–05 November (IEEE, 2008), pp. 1916–1919.
- ⁴⁴⁵L. Shu, B. Peng, Y. Cui, D. Gong, X. Liu, and W. Zhang, *Sens. Actuator A Phys.* **249**, 57–61 (2016).
- ⁴⁴⁶Y. C. Chen and C. C. Cheng, *IEEE Trans. Ultrason., Ferroelectr., Freq. Contr.* **43**, 417–421 (1996).
- ⁴⁴⁷S. Wu, Y. C. Chen, and M. S. Lee, *J. Electron. Mater.* **32**, 191–194 (2003).
- ⁴⁴⁸S. Pan, M. M. Memon, J. Wan, T. Wang, and W. Zhang, *IEEE Sens. J.* **22**, 3097–3104 (2022).
- ⁴⁴⁹X. Zhou, Q. Tan, X. Liang, B. Lin, T. Guo, and Y. Gan, *Micromachines* **12**, 643 (2021).
- ⁴⁵⁰C. Li, X. Liu, L. Shu, and Y. Li, *Mater. Express* **5**, 367–370 (2015).
- ⁴⁵¹C. Li, X. Z. Liu, B. Peng, L. Shu, and Y. R. Li, *Rare Met.* **35**, 408–411 (2016).
- ⁴⁵²A. Nicoloiu, G. E. Stan, C. Nastase, G. Boldeiu, C. Beşleagă, A. Dinescu, and A. Müller, *IEEE Trans. Ultrason. Ferroelectr. Freq. Control* **68**, 1938–1948 (2020).
- ⁴⁵³A. B. Randles, J. M. Tsai, P. Kropelnicki, and H. Cai, *J. Autom. Control Eng.* **2**, 191–194 (2014).
- ⁴⁵⁴G. Chung and H. Hong, *J. Korean Phys. Soc.* **55**, 1446–1450 (2009).
- ⁴⁵⁵R. Cuerdo, J. Pedrós, A. Navarro, A. F. Brana, J. L. Pau, E. Munoz, and F. Calle, *J. Mater. Sci.: Mater. Electron.* **19**, 189–193 (2008).
- ⁴⁵⁶E. Lugo-Hernández, T. Mirea, J. M. Carmona-Cejas, M. Clement, J. Olivares, C. Collado, and J. Mateu, in *Proceedings of IEEE International Ultrasonics Symposium*, Xi'an, China, 11–16 September (IEEE, 2021), pp. 1–3.
- ⁴⁵⁷M. DeMiguel-Ramos, M. Clement, J. Goicuria, J. Olivares, T. Mirea, E. Iborra, G. Rughoobur, A. J. Flewitt, and W. I. Milne, in *Proceedings of IEEE International Ultrasonics Symposium*, Chicago, IL, USA, 03–06 September (IEEE, 2014), pp. 1484–1487.
- ⁴⁵⁸V. V. Felmetser and M. K. Mikhov, in *Proceedings of IEEE International Ultrasonics Symposium*, Orlando, FL, USA, 18–21 October (IEEE, 2011), pp. 835–839.
- ⁴⁵⁹T. Mirea, M. Clement, J. Olivares, and E. Iborra, *IEEE Electron Device Lett.* **41**, 609–612 (2020).
- ⁴⁶⁰M. Abd Allah, R. Thalhammer, J. Kaitila, T. Herzog, W. Weber, and D. Schmitt-Landsiedel, *Solid-State Electron.* **54**, 1041–1046 (2010).
- ⁴⁶¹T. Mirea, J. Olivares, M. Clement, J. Sangrador, and E. Iborra, in *Proceedings of IEEE International Ultrasonics Symposium*, Kobe, Japan, 22–25 October (IEEE, 2018), pp. 1–4.
- ⁴⁶²T. Mirea, J. Olivares, M. Clement, J. L. Olivera, J. Sangrador, and E. Iborra, in *Proceedings of IEEE European Frequency and Time Forum & International Frequency Control Symposium (EFTF-IFCS)*, Besancon, France, 09–13 July (IEEE, 2017), pp. 519–522.
- ⁴⁶³M. DeMiguel-Ramos, J. Olivares, M. Clement, T. Mirea, J. Sangrador, E. Iborra, and M. Barba, in *Proceedings of IEEE SENSORS*, Valencia, Spain, 02–05 November (IEEE, 2014), pp. 966–969.
- ⁴⁶⁴T. Mirea, M. Clement, J. Olivares, and E. Iborra, in *Proceedings of IEEE European Frequency and Time Forum (EFTF)*, Turin, Italy, 10–12 April (IEEE, 2018), pp. 17–19.
- ⁴⁶⁵J. Munir, M. DeMiguel-Ramos, H. J. Lee, M. A. Saeed, and E. Iborra, *J. Microelectromech. Syst.* **26**, 1306–1315 (2017).
- ⁴⁶⁶H. Lamb, *Proc. R. Soc. London Ser. A* **93**, 114–128 (1917).
- ⁴⁶⁷Z. Qian, V. Rajaram, S. Kang, and M. Rinaldi, in *Proceedings of IEEE European Frequency and Time Forum & International Frequency Control Symposium (EFTF-IFCS)*, Besancon, France, 09–13 July (IEEE, 2017), pp. 500–501.
- ⁴⁶⁸S. Gong, N. K. Kuo, and G. Piazza, in *Proceedings of IEEE International Frequency Control Symposium & European Frequency and Time Forum (EFTF-IFCS)*, San Francisco, CA, USA, 02–05 May (IEEE, 2011), pp. 1–5.
- ⁴⁶⁹X. Le, J. Pang, D. Li, and J. Xie, in *Proceedings of 13th IEEE Annual International Conference on Nano/Micro Engineered and Molecular Systems*, Singapore, 22–26 April (IEEE, 2018), pp. 566–569.
- ⁴⁷⁰S. Link, R. Lu, S. Zhang, S. Gong, A. Dissanayake, and S. M. Bowers, in *Proceedings of Joint Conference of the IEEE International Frequency Control Symposium and International Symposium on Applications of Ferroelectrics (IFCS-ISAF)*, Keystone, CO, USA, 19–23 July (IEEE, 2020), pp. 1–4.
- ⁴⁷¹M. Rinaldi, C. Zuniga, and G. Piazza, in *Proceedings of 22nd IEEE International Conference on Micro Electro Mechanical Systems (MEMS)*, Sorrento, Italy, 25–29 January (IEEE, 2009), pp. 916–919.
- ⁴⁷²G. Wingqvist, L. Arapan, V. Yantchev, and I. Katardjiev, in *Proceedings of IEEE International Ultrasonics Symposium*, Beijing, China, 02–05 November (IEEE, 2008), pp. 1207–1210.
- ⁴⁷³C. M. Lin, T. T. Yen, Y. J. Lai, V. V. Felmetser, M. A. Hopcroft, J. H. Kuypers, and A. P. Pisano, in *Proceedings of IEEE International Frequency Control Symposium & European Frequency and Time Forum (IFCS-EFTF)*, Besancon, France, 20–24 April (IEEE, 2009), pp. 5–9.
- ⁴⁷⁴C. M. Lin, T. T. Yen, Y. J. Lai, V. V. Felmetser, M. A. Hopcroft, J. H. Kuypers, and A. P. Pisano, *IEEE Trans. Ultrason. Ferroelectr. Freq. Control* **57**, 524–532 (2010).
- ⁴⁷⁵C. M. Lin, Y. Y. Chen, V. V. Felmetser, D. G. Senesky, and A. P. Pisano, in *Proceedings of IEEE International Ultrasonics Symposium*, Prague, Czech Republic, 21–25 July (IEEE, 2013), pp. 1093–1096.
- ⁴⁷⁶C. M. Lin, Y. J. Lai, T. T. Yen, J. C. Hsu, Y. Y. Chen, D. G. Senesky, and A. P. Pisano, in *Proceedings of 16th International Conference on Solid-State Sensors, Actuators and Microsystems (Transducers'11)*, Beijing, China, 05–09 June (IEEE, 2011), pp. 1512–1515.
- ⁴⁷⁷C. M. Lin, T. T. Yen, V. V. Felmetser, M. A. Hopcroft, J. H. Kuypers, and A. P. Pisano, in *Proceedings of IEEE International Frequency Control Symposium (IFCS)*, Newport Beach, CA, USA, 01–04 June (IEEE, 2010), pp. 14–18.
- ⁴⁷⁸C. M. Lin, T. T. Yen, V. V. Felmetser, J. H. Kuypers, and A. P. Pisano, in *Proceedings of IEEE International Ultrasonics Symposium*, Orlando, FL, USA, 18–21 October (IEEE, 2011), pp. 2078–2081.
- ⁴⁷⁹W. Pan and F. Ayazi, in *Proceedings of 23rd IEEE International Conference on Micro Electro Mechanical Systems (MEMS)*, Hong Kong, China, 24–28 January (IEEE, 2010), pp. 727–730.
- ⁴⁸⁰M. Shahmohammadi, B. P. Harrington, and R. Abdolvand, *IEEE Trans. Electron Devices* **60**, 1213–1220 (2013).
- ⁴⁸¹R. Abdolvand, H. M. Lavasani, G. K. Ho, and F. Ayazi, *IEEE Trans. Ultrason. Ferroelectr. Freq. Control* **55**, 2596–2606 (2008).
- ⁴⁸²R. Tabrizian, M. Pardo, and F. Ayazi, in *Proceedings of 25th IEEE International Conference on Micro Electro Mechanical Systems (MEMS)*, Paris, France, 29 January–02 February (IEEE, 2012), pp. 23–26.
- ⁴⁸³G. Piazza, P. J. Stephanou, and A. P. Pisano, *J. Microelectromech. Syst.* **15**, 1406–1418 (2006).
- ⁴⁸⁴R. H. Olsson, C. M. Washburn, J. E. Stevens, M. R. Tuck, and C. D. Nordquist, in *Proceedings of IEEE International Frequency Control Symposium (IFCS)*, Honolulu, HI, USA, 19–21 May (IEEE, 2008), pp. 634–639.
- ⁴⁸⁵G. Wu, J. Xu, X. Zhang, N. Wang, D. Yan, J. L. K. Lim, Y. Zhu, W. Li, and Y. Gu, *IEEE Trans. Ind. Electron.* **65**, 3576–3584 (2018).
- ⁴⁸⁶O. Zyowitzki, T. Modes, S. Barth, H. Bartzsch, and P. Frach, *Surf. Coat. Technol.* **309**, 417–422 (2017).
- ⁴⁸⁷W. Wang, Y. Q. Fu, J. J. Chen, W. P. Xuan, J. K. Chen, X. Z. Wang, P. Mayrhofer, P. F. Duan, A. Bittner, U. Schmid, and J. K. Luo, *J. Micromech. Microeng.* **26**, 075006 (2016).
- ⁴⁸⁸H. Wang, L. Zhang, Z. Zhou, and L. Lou, *Micromachines* **14**, 1065 (2023).
- ⁴⁸⁹S. Rassay, F. Hakim, M. Ramezani, and R. Tabrizian, in *Proceedings of 33rd IEEE International Conference on Micro Electro Mechanical Systems (MEMS)*, Vancouver, BC, Canada, 18–22 January (IEEE, 2020), pp. 1254–1257.
- ⁴⁹⁰M. A. Moreira, J. Bjurström, V. Yantchev, and I. Katardjiev, *IOP Conf. Ser.: Mater. Sci. Eng.* **41**, 012014 (2012).
- ⁴⁹¹T. Yanagitani and M. Suzuki, *Appl. Phys. Lett.* **105**, 122907 (2014).
- ⁴⁹²J. Wang, M. Park, and A. Ansari, in *Proceedings of 34th IEEE International Conference on Micro Electro Mechanical Systems (MEMS)*, Gainesville, FL, USA, 25–29 January (IEEE, 2021), pp. 214–217.
- ⁴⁹³J. Wang, M. Park, S. Mertin, T. Pensala, F. Ayazi, and A. Ansari, *J. Microelectromech. Syst.* **29**, 741–747 (2020).
- ⁴⁹⁴T. Yanagitani, K. Arakawa, K. Kano, A. Teshigahara, and M. Akiyama, in *Proceedings of IEEE International Ultrasonics Symposium*, San Diego, CA, USA, 11–14 October (IEEE, 2010), pp. 2095–2098.

- ⁴⁹⁵Y. Zheng, J. Wang, M. Park, P. Wang, D. Wang, Z. Mi, and A. Ansari, in *Proceedings of 25th IEEE International Conference on Micro Electro Mechanical Systems (MEMS)*, Tokyo, Japan, 09–13 January (IEEE, 2022), pp. 1046–1049.
- ⁴⁹⁶M. S. Lozano, Z. Chen, O. A. Williams, and G. F. Iriarte, *Smart Mater. Struct.* **27**, 075015 (2018).
- ⁴⁹⁷M. Park, Z. Hao, R. Dargis, A. Clark, and A. Ansari, *J. Microelectromech. Syst.* **29**, 490–498 (2020).
- ⁴⁹⁸S. Shao, Z. Luo, Y. Lu, A. Mazzalai, C. Tosi, and T. Wu, *J. Microelectromech. Syst.* **31**, 328–337 (2022).
- ⁴⁹⁹S. Shao, Z. Luo, and T. Wu, in *Proceedings of 21st International Conference on Solid-State Sensors, Actuators and Microsystems (Transducers'21)*, Orlando, FL, USA, 20–24 June (IEEE, 2021), pp. 1371–1374.
- ⁵⁰⁰S. Shao, Z. Luo, and T. Wu, *IEEE Electron Device Lett.* **42**, 1378–1381 (2021).
- ⁵⁰¹Z. Luo, S. Shao, K. Liu, Y. Lu, A. Mazzalai, C. Tosi, and T. Wu, *Appl. Phys. Lett.* **120**, 173508 (2022).
- ⁵⁰²A. Lozzi, E. T. T. Yen, P. Muralt, and L. G. Villanueva, *IEEE Trans. Ultrason. Ferroelectr. Freq. Control* **66**, 146–153 (2018).
- ⁵⁰³S. Ji, P. Akhakandi, Y. Qi, R. Abdolvand, and H. M. Lavasani, *IEEE Sens. J.* **23**, 9194–9203 (2023).
- ⁵⁰⁴S. Ghosh, J. Sharma, E. J. Ng, D. J. Goh, S. Merugu, Y. Koh, and A. Lal, in *Proceedings of IEEE International Ultrasonics Symposium (IUS)*, Xi'an, China, 11–16 September (IEEE, 2021), pp. 1–4.
- ⁵⁰⁵V. J. Gokhale, J. Roberts, and M. Rais-Zadeh, in *Proceedings of 16th International Conference on Solid-State Sensors, Actuators and Microsystems (Transducers'11)*, Beijing, China, 05–09 June (IEEE, 2011), pp. 926–929.
- ⁵⁰⁶F. Bartoli, T. Aubert, M. Moutaouekkil, J. Streque, P. Pigeat, S. Zhgoon, A. Talbi, S. Hage-Ali, H. M'Jahed, and O. Elmazria, *Sens. Actuator A Phys.* **283**, 9–16 (2018).
- ⁵⁰⁷A. Müller, G. Konstantinidis, V. Buiculescu, A. Dinescu, A. Stavrinidis, A. Stefanescu, G. Stavrinidis, I. Giangu, A. Cismaru, and A. Modoveanu, *Sens. Actuators A: Phys.* **209**, 115–123 (2014).
- ⁵⁰⁸A. Müller, G. Konstantinidis, A. Stefanescu, I. Giangu, A. Stavrinidis, M. Pasteanu, G. Stavrinidis, and A. Dinescu, in *Proceedings of 19th International Conference on Solid-State Sensors, Actuators and Microsystems (Transducers'17)*, Kaohsiung, Taiwan, 18–22 June (IEEE, 2017), pp. 1073–1076.
- ⁵⁰⁹W. Soluch and E. Brzozowski, *IEEE Trans. Electron Devices* **61**, 3395–3398 (2014).
- ⁵¹⁰I. Ahmed, U. Rawat, J. T. Chen, and D. Weinstein, in *Proceedings of 35th IEEE International Conference on Micro Electro Mechanical Systems (MEMS)*, Tokyo, Japan, 09–13 January (IEEE, 2022), pp. 192–195.
- ⁵¹¹S. V. Pettersen, T. Tybell, A. Rønneklev, S. Rooth, V. Schwegler, and J. K. Grepstad, *Mater. Res. Soc. Symp. Proc.* **743**, L6-37 (2002).
- ⁵¹²A. Ansari, V. J. Gokhale, V. A. Thakar, J. Roberts, and M. Rais-Zadeh, in *2011 IEEE Int. Electron Device Meeting (IEDM)*, Washington, DC, USA, 05–07 December (IEEE, 2011), pp. 20.3.1–20.3.4.
- ⁵¹³J. R. Montague, K. A. Bertness, N. A. Sanford, V. M. Bright, and C. T. Rogers, *Appl. Phys. Lett.* **101**, 173101 (2012).
- ⁵¹⁴L. Sang, H. Sun, X. Yang, T. Li, B. Shen, and M. Liao, in *2020 IEEE International Electron Device Meeting (IEDM)*, San Francisco, CA, USA, 12–18 December (IEEE, 2020), pp. 26.4.1–26.4.4.
- ⁵¹⁵H. Sun, L. Sang, X. Shen, X. Yang, T. Li, J. Q. You, B. Shen, and M. Liao, *J. Appl. Phys.* **131**, 054502 (2022).
- ⁵¹⁶H. H. Jeong, S. K. Kim, Y. C. Jung, H. C. Choi, J. H. Lee, and Y. H. Lee, *Phys. Status Solidi A* **188**, 247–250 (2001).
- ⁵¹⁷C. Y. Jang, M. J. Park, S. Y. Ryu, H. C. Choi, J. H. Lee, and Y. H. Lee, *Phys. Status Solidi C* **1**, 248–252 (2003).
- ⁵¹⁸S. K. Kim, M. J. Park, C. Y. Jang, J. H. Lee, H. C. Choi, J. H. Lee, and Y. H. Lee, in *Proceedings of IEEE International Ultrasonics Symposium*, Atlanta, GA, USA, 07–10 October (IEEE, 2001), pp. 257–260.
- ⁵¹⁹A. C. Bunea, D. Neculoiu, and A. Dinescu, in *Proceedings of IEEE Asia Pacific Microwave Conference (APMC)*, Kuala Lumpur, Malaysia, 13–16 November (IEEE, 2017), pp. 1010–1013.
- ⁵²⁰X. Ji, W. X. Dong, Y. M. Zhang, J. F. Wang, and K. Xu, *Chin. Phys. B* **28**, 067701 (2019).
- ⁵²¹A. Müller, G. Konstantinidis, I. Giangu, V. Buiculescu, A. Dinescu, A. Stefanescu, A. Stavrinidis, G. Stavrinidis, and A. Ziae, in *Proceedings of IEEE MTT-S International Microwave Symposium*, Tampa, FL, USA, 01–06 June (IEEE, 2014), pp. 1–4.
- ⁵²²H. H. Jeong, S. K. Kim, J. S. Lee, H. C. Choi, J. H. Lee, and Y. H. Lee, in *Proceedings of IEEE International Ultrasonics Symposium*, Atlanta, GA, USA, 07–10 October (IEEE, 2001), pp. 207–209.
- ⁵²³A. Qamar, M. Ghate, R. Tabrizian, and M. Rais-Zadeh, in *Proceedings of IEEE 33rd International Conference on Micro Electro Mechanical Systems (MEMS)*, Vancouver, BC, Canada, 18–22 January (IEEE, 2020), pp. 1211–1214.
- ⁵²⁴V. J. Gokhale, B. P. Downey, D. S. Katzer, and D. J. Meyer, *Appl. Phys. Lett.* **117**, 124003 (2020).
- ⁵²⁵M. Ghate, M. Rais-Zadeh, and R. Tabrizian, in *Proceedings of 21st International Conference on Solid-State Sensors, Actuators and Microsystems (Transducers'21)*, Orlando, FL, USA, 20–24 June (IEEE, 2021), pp. 1400–1403.
- ⁵²⁶A. Ansari and M. Rais-Zadeh, *IEEE Electron Device Lett.* **35**, 1127–1129 (2014).
- ⁵²⁷P. X.-L. Feng, “Resonant Nanoelectromechanical Systems (NEMS): Progress and emerging frontiers,” in *Proceedings of 33rd IEEE International Conference on Micro Electro Mechanical Systems (MEMS 2020)*, Vancouver, Canada, 18–22 January (IEEE, 2020), pp. 212–217.
- ⁵²⁸B. Xu, P. Zhang, J. Zhu, Z. Liu, A. Eichler, X. Q. Zheng, J. Lee, A. Dash, S. More, S. Wu, Y. Wang, H. Jia, A. Naik, A. Bachtold, R. Yang, P. X.-L. Feng, and Z. Wang, “Nanomechanical resonators toward atomic scale,” *ACS Nano* **16**(10), 15545–15585 (2022).
- ⁵²⁹X. L. Feng, C. A. Zorman, M. Mehregany, and M. L. Roukes, “Dissipation in single-crystal 3C-SiC UHF nanomechanical resonators,” in *The 12th Solid-State Sensors, Actuators, and Microsystems Workshop (Hilton Head'06)*, Hilton Head Island, SC, June 4–8 (IEEE, 2006), pp. 86–89.
- ⁵³⁰X. L. Feng, R. He, P. Yang, and M. L. Roukes, “Quality factors and energy losses of very-high frequency silicon nanowire electromechanical resonators,” in *14th International Conference on Solid-State Sensors, Actuators, and Microsystems (Transducers'07)*, Lyon, France, June 10–14 (IEEE, 2007), pp. 1325–1326.
- ⁵³¹A. Islam, J. Lee, and P. X.-L. Feng, in *Proceedings of IEEE 33rd International Conference on Micro Electro Mechanical Systems (MEMS)*, Vancouver, BC, Canada (IEEE, 2020), pp. 826–829.
- ⁵³²A. Islam, A. van den Akker, and P. X.-L. Feng, “Anisotropic thermal conductivity of suspended black phosphorous probed by opto-thermomechanical resonance spectromicroscopy,” *Nano Lett.* **18**, 7683–7691 (2018).
- ⁵³³R. Yang, Z. Wang, and P. X.-L. Feng, in *Proceedings of IEEE International Frequency Control Symposium & European Frequency and Time Forum (IFCS-EFTF)*, Denver, CO, USA, 12–14 April (IEEE, 2015), pp. 198–201.
- ⁵³⁴Z. Wang, R. Yang, A. Islam, and P. X.-L. Feng, “Observation of strong temperature hysteresis in molybdenum disulfide (MoS_2) vibrating nanomechanical resonators,” in *Proceedings of 2015 Joint Conference of the IEEE International Frequency Control Symposium (IFCS) & European Frequency and Time Forum (EFTF)*, 783–786, Denver, CO, April 12–16 (IEEE, 2015).
- ⁵³⁵Z. Wang, R. Yang, and P. X.-L. Feng, “Thermal hysteresis controlled reconfigurable MoS_2 nanomechanical resonators,” *Nanoscale* **13**, 18089–18095 (2021).
- ⁵³⁶X.-Q. Zheng, J. Lee, and P. X.-L. Feng, in *Proceedings of 18th International Conference on Solid-State Sensors, Actuators and Microsystems (Transducers'15)*, Anchorage, AK, USA (IEEE, 2015), pp. 1393–1396.
- ⁵³⁷S. Wu, F. Xiao, J. Zhu, Y. Liang, C. Jiao, S. Pei, and Z. Wang, in *Proceedings of IEEE 35th International Conference on Micro Electro Mechanical Systems (MEMS)*, Tokyo, Japan (IEEE, 2022), pp. 551–553.
- ⁵³⁸N. Arora and A. Naik, in *Proceedings of IEEE Sensors*, Sydney, Australia (IEEE, 2021), pp. 1–4.
- ⁵³⁹F. Ye, J. Lee, and P. X.-L. Feng, “Electrothermally tunable graphene resonators operating at very high temperature up to 1200 K,” *Nano Lett.* **18**, 1678–1685 (2018).
- ⁵⁴⁰J. Lee, H.-Y. Chiu, L. Zhao, J. Shan, and P. X.-L. Feng, “Temperature compensated graphene nanomechanical resonators,” *Adv. Funct. Mater.* **35**, 2415708 (2025).